Final Report for NASA Grant NAG5-504: "A Search for Outflows from X-ray Bright Points in Coronal Holes"

D. J. Mullan

Bartol Research Foundation, University of Delaware, Newark, DE 19716

and

W. L. Waldron

Applied Research Corporation, 8401 Corporation Drive, Suite 650, Landover, MD 20785.

1. Introduction

The aim of this work was to investigate properties of X-ray bright points using two of the instruments on Solar Maximum Mission, and to model the mass outflows from magnetic regions.

2. Observations with UVSP

The aim of this part of the experiment was to obtain raster scans of areas of coronal holes where X-ray bright points were known to be present. Intensity and Doppler information are used to determine characteristics of the velocity fields in the bright points. We do not identify the X-ray bright points directly. We use a ground-based proxy of the bright points (see below), and we assume also that points which are bright in CIV emission (as seen with UVSP) correspond to X-ray bright points.

To identify the coronal holes, images of the sun taken in the 10830 A line of helium (which are obtained every clear day at Kitt Peak National Observatory) were transmitted via telephone line to SMM control center at Goddard Space Flight Center. On these images, coronal holes are detectable as brighter than normal areas. Also on the images, X-ray bright points appear as darker than normal areas. Thus, we seek to obtain UVSP images of helium dark points in coronal holes. For purposes of our experiment (i.e. obtaining Doppler shifts of outflows), it is essential that the coronal hole(s) lie at low latitudes.

(NASA-CR-176647) A SEARCH FOR OUTFLOWS FROM X-RAY BRIGHT POINTS IN CORONAL HOLES Final Report (Delaware Univ.) 84 p HC A05/MF A01 CSCL 03A

N86-22458

G3/89 Unclas 05850

2.1. Data acquisition

Shortly after our proposal was funded in late 1984, we were informed that we would be granted observing time on five days early in February 1985 (Febr. 2, 3, 4, 6, and 8). Our contact person at UVSP control was to be Dr. P. Nakada. During the time of our observations, we were fortunate in that the Sun showed a low latitude coronal hole, including some He dark points. Unfortunately, observing conditions at Kitt peak were not favorable for all the days of our SMM observations: only on Feb. 1 and Feb 7 were He 10830 spectroheliograms obtained at Kitt Peak. As a result, a certain amount of guesswork was involved in pointing SMM on certain days.

On the five days, nine sets of observations were obtained, although only seven of these turned out to be complete. A complete set of observations consisted of five separate exposures.

[1] A 3-minute exposure to obtain lambda-max (global), picking out the most intense wavelength in the chosen field of view. In this mode, the central pixel (with area 3 X 3 arcsec) of the field of view is scanned in wavelength, with an exposure of 0.496 seconds of time per resolution element. In all cases in our program, the line of interest to us is the 1548.19 A line of CIV: this probes conditions in the solar atmosphere at temperatures of order 100,000 K. Hence, Lambda-max procedure in all of our cases yields peak intensity close to 1548A.

[2] Having determined peak wavelength, we now do a raster scan of an area of 180 X 180 arcseconds, with a short exposure time per pixel (0.063 sec). With pixel sizes of 3X3 arcsec, this fast raster scan has 3600 pixels, and is completed about 4 minutes. Detectors 1 and 2 are used, one fixed in wavelength on the red side of the line, one fixed in wavelength on the blue side. Adding the signals of detectors 1 and 2 tells us what the total intensity in each pixel is; this gives us a quick look at a large area of the sun, to pick out the bright points in CIV emission. We presume that the brightest point in the 180 X 180 arcsec area is of most interest to us. That point then serves as the focus for the next exposure.

[3] At the point of maximum intensity, we again do a Lambda-max (global), to ensure that we are close to the 1548.19A line of CIV. Here, the entrance aperture is fixed at a single pixel, and a wavelength scan is performed, with exposure of 0.992 sec per resolution element. With the wavelength scale again checked in this way, we are now ready to perform the principal observing routine.

[4] An area of 90 X 90 arcsec around the point of maximum intensity is rastered, again with pixel size 3 x 3 arcsec, and again with detectors 1 and 2 positioned on the red and blue sides of the line center. Now, the exposure time is quite long, 2.4 seconds per pixel, so as to achieve good signal to noise. With 900 pixels to scan, this procedure occupies 36-37 minutes, i.e. about two-thirds of the entire sunlit portion of the orbit.

[5] Finally, the last 4 minutes of sunlight are used to re-do the larger area scan (180 X 180 arcsec) to verify that we are still observing the brightest part of the field of view.

The nine Dopplergrams which we obtained are exposures 26492, 26497, 26544, 26624, 26629, 26723, 26728, 26787, and 26792. The shortest time intervals between consecutive pairs of these exposures were 93-99 minutes (26492-26497; 26624-26629; 26723-26728; 26787-26792).

Before a new series of observations could be scheduled, UVSP broke down, in the sense that no further Dopplergrams could be taken. Hence, the nine exposures obtained above constitute the entire data set in this section of our program. At our request, Dr. S. Drake searched through the UVSP archives for any further data which might have been gathered on CIV in coronal holes. Under the category "HOLES", and at wavelengths between 1500 and 1600 A, Dr Drake found no data at all from the first portion of SMM lifetime. After the revival of SMM in 1984, 31 exposures were obtained (apart from our observing run) between June 15, 1984 and April 3, 1985. Of these, the only exposures which were in the Dopplergram mode were 21129, 21130 (9/20/84), and 25230, 25231 (1/9/85). Unfortunately, in all four cases, exposure time per pixel was only 0.063 seconds, i.e. much shorter than we used in our coronal hole exposures. Thus, it appears that the data we obtained in February 1985 are a unique sampling of velocity fields of CIV bright points in coronal holes.

2.2. Data reduction

The first phase of data reduction was performed with the help of Dr. Nakada. He showed us how to use ANA commands on the SMM PDP computer to obtain contour plots of intensity and Doppler shifts from the 900 pixel scans. From these, it appeared that we indeed had obtained regions where bright points in CIV existed. However, when we plotted the Doppler signals, it was apparent that there was a systematic variation of Doppler signal from top to bottom of the plot, presumably due to the orbital motion during the 36-37 minute exposure (see Fig. 1: the label is DOPPLER). We tried to manipulate the files in such a way as to subtract off the effects of the orbital motion. However, neither the Co-I nor the PI had any experience with ANA, and the best we could do, finally, was to devise a crude linear subtraction across the image. After doing that, we plotted the Doppler signals and the total intensities on contour maps, and it appeared that some bright points did coincide with some blue shifted flows. In particular, on exposure 26544, it appeared that a very strongly blueshifted core coincided almost perfectly with a bright CIV emission region (see Fig. 2, labelled INTENSITY, for the intensity contour plot, and Fig. 3, labelled DOPPLER CORRECTED, for the "corrected" velocity contours: in the velocity contours, negative velocities are shown dashed. The blue-shifted bright point is labelled A on Figs. 2 and 3. Other CIV bright points coincided with both red and blue shifts. However, the inability to correct properly for orbital motion suggested to us that this method of data reduction was not satisfactory.

Consultations with Dr. J. Gurman of Applied Research Corporation enabled us to re-reduce the data. Dr Gurman introduced us to the IDL language, and showed us how to sum over all pixels in blue and red detectors on a particular exposure, and how to correct for that. He showed us how to form difference and sums from the data, and then take ratios of differences over sums and convert to velocities. With the small Doppler signals in our sample, the error function which enters into the relationships between SMM difference/sum ratios can be approximated by a linear term alone, according to Dr. Gurman. We would like to take this opportunity to express our gratitude to Dr Gurman for the detailed and generous assistance which he gave to us in our reductions.

We averaged over columns of pixels (from North to South in the original raster coordinartes) in order to model the orbital veolcity variations across the exposure. With this averaged variation, we then fitted a 4-th order polynomial to represent the orbital change in velocity across the exposure. An example of the fit is shown in Fig. 4, again for exposure 26544. Once the polynomial coefficients have been determined, the fit is subtracted from the velocity array. To ensure, visually, that the proper subtraction has been performed, we plot a histogram of the velocities on all 900 pixels of the Dopplergram: see Fig. 5.

The horizontal scale in Fig. 5 is in units of the half-half width of the CIV line, 0.15 Angstroms. Thus, unity on the horizontal scale in Fig. 5 corresponds to a velocity of about 30 km/sec. Notice that the histogram is indeed peaked around zero, so that the velocity subtraction seems to have been done satisfactorily. The tails of the distribution extend to about +0.4 and -0.5, indicating velocities of at most 15 km/sec in these data.

What we are looking for is blue-shifts from bright points. To see if there are any gross indications of such behavior, we have plotted in Fig. 6 a scatter plot of Velocity vs. Intensity for all 900 pixels in exposure 26544. There is no indication of strong negative velocities at predomimantly high intensities. In fact, other SMM data suggest that if anything, in a plot such as that shown in Fig. 6, if there is a trend at all, it is that the points fall on a branch which rises towards the right, i.e. the more intense emission is correlated preferentially with redward Doppler shifts. Thus, downfalling material tends to be brightest, in general areas of the sun: this was discovered in about half of the sample points obtained in active regions by Athay et al (1983, Ap.J. 269, 706). Athay et al did note a few cases where there was a correlation between intensity and blueshift, especially in cases where a loop showed a bright top. Thus, we must conclude that in general, outflows from bright points are rare events, too rare to create a trend in Fig. 6.

Therefore, if we are to find examples of the kind we are seeking, we must look at individual features in our data. The data of intensity and velocity must both be plotted, and then we must compare bright features in the intensity plots with the same locations on the velocity plots. Examples of intensity and Doppler data were displayed, for a first look, on the color monitor and photographed for our records. The Doppler pixels were color coded in red and blue for downdrafts and upflows, respectively: the depth of the color is a measure of the Doppler shift. The intensity pixels are color coded with white for maximum intensity. For a more quantitatve analysis, we need to know the actual velocity values: for this, contours must be plotted.

Plotting contours requires us to choose contour levels. We experimented with various choices of contour levels in order to bring out features we were interested in. In Figs. 7, 8 and 9 we show three different choices of contour levels for the Intensity of pixels in exposure 26544. There are some differences in detail between the plots, but the major bright points can be readily identified in all three plots. There is a pair of bright points near the center, a pair near the lower right boundary, and a single point (A') near the center of the right hand edge. Dr Gurman's reduction routine rectified the aspect of the plot, and is therefore rotated 90 degrees with respect to the plot obtained in ANA (Fig. 2). Hence, point A in Fig. 2 corresponds to point A' in Figs. 7, 8, and 9.

For the velocity contours, plots which included both positive and negative Doppler signals turned out to be somewhat confusing to interpret readily. Hence, we chose to plot positive and negative velocities on separate displays so as to enhance the possibility of identifying blue-shifted areas without confusion from low velocity noise. To pick the contour levels, we first evaluated the maximum red-shifted Doppler signal (MX) and the minimum blue-shifted signal (MN). In Fig. 10, for exposure 26544, we show the redshifted contours at levels 0.4, 0.55, 0.7, 0.85, and 1.0 (in units of MX).

There is some overlap of the red-shifted flows with the bright points labelled B and C in Fig. 9. However, the red-shifted peaks lie definitely displaced from the peaks in brightness. Similar behavior can be seen for the point labelled D in Fig. 9. Thus, in exposure 26544, we have no definite association of bright points with red-shifts, although there are some close correspondences.

For blue-shifts, we chose a series of contour levels. In Fig. 11 we show the most highly blue-shifted material, with contours at 1.0, 0.9, 0.8, 0.7, and 0.6 (in units of MN). The most blue-shifted feature corresponds to no bright emission in Fig. 9. To pick up some less blue-shifted material, we show in Fig. 12 our contour plots in velocity space at contour levels 1.0, 0.85, 0.7, 0.55, and 0.4 (in units of MN). Now, other blue-shifted patches show up in other parts of the field of view, but none has any obvious correspondence to any feature in the intensity contour plot (Fig. 9). Moving on to include further material, at even smaller blue-shifts, in Fig. 13 we show velocity contours at levels 1.0, 0.8, 0.6, 0.4, and 0.2 (in units of MN). Feature B in Fig. 9 now is superposed by a blue-shifted contour, as is also feature D. Around feature A', blue-shifted contours appear to form a partial collar, but the blue-shifts do not overlap with the region of intense brightness itself. Finally, going to even smaller blue-shifts, in Fig. 14 we present velocity contours at Doppler signal values of -0.40, -0.28, -0.16, and -0.04. (These are in Doppler units, and not in units of MN.) Some blue-shift contours now overlap with all of the labelled intense features in Fig. 9. Hence, all four features have some up-welling material located directly in coincidence with the peak intensity, although the velocities involved are all small (only 1-2 km/sec). Moreover, is we also push the contour levels of red-shifted material down to the low levels included in Fig. 14, we also find that red-shifts overlap partially the regions of large intensity (see Fig. 15, which has Doppler contour levels of +0.38, +0.24, +0.10, and -0.04).

However, we note that the intensity blue-shifted contours which appeared in our first Doppler plots (Figs. 1, 3) do not appear here at all. In our first reductions, we must have used erroneous procedures.

We have examined all of our exposures with the same approach as we have just described in detail for exposure 26544. We now take the others in order, to describe what we see in each of them.

[26492]Maximum blue-shift is -0.45. Intensity plot in Fig. 16 shows a broad ridge of emission stretching across the center of the plot, with two other regions of intense emission at lower left and lower right. Contours of positive velocity (Fig. 17) show pronounced features across the central ridge, with close coincidences with the intense peaks of emission. Thus, here we see good examples of downflowing material in regions of strong

emission. When we plot the negative velocities (Fig. 18), we find that the most pronounced blue-shifts do not coincide with any strong intensity features.

[26497]Maximum blue-shift is -0.65, associated with a partial data drop-out in the upper left-hand corner. Intensity plot in Fig. 19 shows five separate areas of emission. Red-shift contours (Fig. 20) show overlap with all five centers of emission. Blue-shift contours (Fig. 21) show no overlap with any of the five centers of emission. Hence, in this area also, we reaffirm the previously established correlation of red-shifted flows with high intensity.

[26624]Maximum blue-shift is -0.45. Intensity plot in Fig. 22 is dominated by a strong emission close to center, with another feature in the lower right-hand corner, and a lesser feature near lower center. The velocity contours in this case are very sparse: poorly developed flows are apparently occurring in this region. Red-shifts (Fig. 23; contours of 1.0, 0.9, 0.8, 0.7, 0.6 MX) have an overlap with the strong central emission, but not with the other two. The lesser feature near lower center overlaps with a blue-shift of -0.3 (i.e. about 10 km/sec)(see Fig. 24). In this frame, then, we see a conventional bright spot correlated with downflow, but also a bright spot associated with upflow.

[26629]Here, the emission is quite complex, and is distributed over a large fraction of the observing window, although there is a gap in the central area (see intensity contours in Fig. 25). Red and blue shift contours are shown in Figs. 26 and 27. The red-shifts do not coincide with intensity features in any obvious way. However, blue-shifted features here do show exact correspondence with several intense features. Exact overlap of blue-shift peaks with intensity peaks occurs for features A and B, and in feature C, the blue-shift peak is only slightly offset from the maximum intensity. Again, the blue-shifts correspond to velocities of about 10 km/sec in the bright features.

[26723]Here, the emission is dominated by a vertical ridge near the center of the contour plot (Fig. 28). The ridge has some red-shifted features peaking along it, although the major area of downflow does not coincide with the ridge (see Fig. 29). Blue-shift peaks also occur at various locations along the ridge (see Fig. 30). Here, peaks of blue-shift do show some correspondence with peaks in intensity. (See features A, B, C, and D in Fig. 28.) In this case, the blue-shifts are all less than 10 km/sec.

[26728]Here, the emission is dominated by two regions along the right-hand side of the intensity plot (Fig. 31). Positive velocities (Fig. 32) are of finite amplitude in only a few very localized areas in this exposure, and none coincides with an intensity peak. Blue-shifts are more widely spread across the field of

view (see Fig. 33), and peaks in blue-shift do coincide with peaks in intensity (see features A, B, C, D, and E in Fig. 31). In exposure 26728, we are therefore confronted with no evidence whatever for infalling material in the bright points: on the contrary, there are several examples of outflow at the brightest points. This has the effect that the intensity-versus- velocity scatter plot (see Fig. 34) does not exhibit the usual tendency of a predominant branch of points rising towards the upper right hand corner. The main tendency in Fig. 34 is for the points to lie along a branch which is more-or-less horizontal, or even tending slightly downwards. Apparently, velocity fields in exposure 26728 are not typical of the solar atmosphere as a whole.

[26787]Here, the emission is complex, with many bright regions distributed throughout the entire field of view (Fig. 35). Red shift contours (in Fig. 36) show several pockets of downflow, one or more of which may overlap with the many bright spots (especially feature A in Fig. 36). Contours of blue-shifts (Fig. 37) also overlap with many bright points, especially those labelled A through I in Fig. 35. Of particular note is feature E, where two peaks in intensity are both included within the same feature in the blue-shift contours. Here are are apparently two bright points side by side with material flowing upwards from both, forming a single "hill" in velocity space. In this field of view, the velocity-versus-intensity scatter plot (Fig. 38) has a broad scatter, and again show no strong tendency for a ridge pointing upwards towards the right-hand top corner. The contrast between the data in Fig. 38 and those, e.g. in Fig. 2 of Gebbie et al (ApJ 251, L115, 1981) is striking. The usual occurrence of dominant redshifts is not apparent in our data.

[26792]Here, the emission is confined to a few small patches (Fig. 39). Red-shift contours (Fig. 40) overlap with some of the emission patches. Blue-shift contours (Fig. 41) in general avoid the emission patches except for feature A in Fig. 41.

2.3. Conclusions from UVSP data

The conclusion we draw from this portion of our work is that in the coronal hole area which we chose for study, we have found many examples of blue-shifts coinciding with peaks in the brightness contours. There are certainly also examples in our data of bright spots being correlated with red shifts. But the general tendency of having red-shifts correlated with intensity (which has been reported by earlier investigators of the solar atmosphere) does not appear to be strongly evident in our data. Whether this is because we have chosen a coronal hole for our studies, and are therefore probing velocity fields in a different kind of solar atmosphere from the earlier studies, is not clear. In order to answer that question, more data will need to be gathered on other coronal holes.

3. Coronagraph Investigation of Polar Plumes

In this portion of the work, we planned to search for temporal variations in intensity along polar plumes. The first step was therefore to use C/P to detect the plumes. This work was done in collaboration with Dr Bob MacQueen at HAO and Chris St Cyr at Goddard.

The observations were done with the usual wide-band green filter (bandpass several hundred A), collecting only clear images (no polaroids). The northeast sector mirror was used so as to avoid regions of blemishes in the SEC vidicon tube. The normal exposures were increased by a factor of two so as to optimize chances of seeing the plumes. To enhance signal to noise, five images were obtained in as small a fraction of an orbit as practical, given the observing control constraints. The images were then sent to Boulder, to be superposed, forming a photographic image of the final product. The observations were carried out over both the north and south solar poles. This meant that at some point in the observing program, the spacecraft had to be rolled.

The results turned out negative. At neither north nor south pole could polar plumes be detected on the photographic images, representing the averages of five exposures at north pole and five at south pole. The sequences of images were repeated several times, in the hopes that temporal variations in solar activity might enhance detectability of the plumes at other times. But results were negative. At present, therefore, it is unfortunately not possible to carry out the proposed study of temporal variations of polar plumes using SMM. However, Dr MacQueen has assured us that if subsequent C/P exposures show the presence of plumes, he will be in contact with us for future work.

4. MHD modelling of outflows

It is well known that X-ray bright points are associated with magnetic bipoles in the solar atmosphere. Therefore, since mass appears to be emerging from certain bright points on the sun, we wanted to investigate how mass might be ejected from magnetic structures in the sun. To investigate this problem, we have constructed a two-dimensional MHD code.

4.1. Physical justification

Before we describe our results, it is important to describe how ideas of mass ejection have altered since we started the project. When we began, it was widely believed that the magnetic bipoles which underlie X-ray bright points in the sun are newly emerged flux loops, i.e. essentially small active regions which have bubbled up to the surface of the sun from the dynamo which operates in the sub-photospheric convection zone. For example, in the models of X-ray bright points proposed by Parker, Gledhill, and others, it was believed that the magnetic loops was twisted or sheared in some way so as to create local reconnection at certain locations on the loop. Perhaps a kink instability on a severely twisted emerging flux tube might explain the local heating which is obviously occurring in an X-ray bright point. With that framework in mind, when we started this modelling, we planned to treat mass flows associated with flux loops with both feet embedded in the photosphere. Because of the earlier work of B. C. Low, we considered it essential to include the effects of stratification of the atmospheric pressure in the neighborhood of the loop. Hence, our MHD code from the beginning was conceived in two-dimensional terms because of the need to include stratification. To our knowledge, the effects of significant stratification have never been incorporated in any solar MHD code for mass loss.

While we were in the process of modelling, a study by K. L. Harvey became available to us (in unpublished form, specifically, as a final report for an Air Force Geophysics Laboratory Contract: we became aware of the work through the NAASA/STAR Journal service). Harvey investigated dark points in HeI 10830 spectroheliograms: these are believed to be proxy indicators of X-ray bright points. Harvey confirmed that indeed the HeI dark points were associated with magnetic bipoles. However, she was able to classify the bipoles into two separate groups: one contains bona fide flux loops which have just emerged from beneath the surface (these she calls ephemeral active regions, ER); the second contains chance encounters of flux loops of opposite polarity as they are jostled across the solar surface by sub-surface buffeting in the convection zone. Harvey finds that most HeI dark points belong to the second group: in coronal holes, for example, 79% of the HeI dark points belong to group 2. This is a radical alteration in our concepts of the magnetic structure associated with X-ray bright points.

Harvey's study became available to us in November 1985, when our MHD modelling of ER loops was leading us to conclude that it would be difficult, if not impossible, to understand how mass would ever be ejected from emergent flux loops (as in ER). Harvey's results suggested to us that we should be considering a different magnetic topology, namely, vertical flux tubes of opposite polarity. As we shall see, modelling mass ejection from X-ray bright points of such structure makes more physical sense.

Another aspect of Harvey's study which is relevant to our present work concerns her correlation studies with solar wind properties. She finds that the areal density of X-ray bright points in coronal holes is positively correlated with the average velocity of the solar wind at the Earth's orbit. This suggests that indeed, the solar wind flow may be controlled by conditions in the X-ray bright points: this possibility is consistent with the hypothesis which we set out to examine in this project, namely, that the solar wind is emerging from X-ray bright points in coronal holes.

4.2. Development of MHD code

Starting from the Boltzmann kinetic equation for the particle distribution function for particles of each species, we derive the usual equations of conservation of mass, momentum, and energy. We do not replace the energy equation by a simplifying assumption, such as polytropic law, or isothermal conditions: we retain the time-dependence. To obtain a single fluid description of the MHD processes, we sum the individual fluid equations over species, and incorporate a re-definition of the pressure tensor in terms of the center-of-mass velocity. For computational convenience, the one-fluid equations are cast in conservative form, including a time derivative, a spatial derivative in the form of a divergence operator, and a source term. The MHD equations are supplemented by Ohm's law and Maxwell's equations. Note that in our treatment, we include finite electrical resistivity. In fact, the effects of resistivity are at the heart of our simulations.

The MHD one-fluid equations are cast into non-dimensional form by suitable scaling. Time is scaled to units of Alfven crossing time of unit length of our grid; velocities are scaled to the Alfven speed at the origin at time zero. Maxwell's equations are scaled in terms of the ratio of Alfven speed to light speed.

To obtain the two-dimensional MHD equations, we make some simplifying assumptions. Charge neutrality is assumed, and isotropic pressure tensor. Collision integrals involving momentum and kinetic energy exchange between species are neglected. Gravity is included in a plane-parallel form, i.e. the potential varies as 1/r where r is written as ro + L y, and y is the vertical coordinate. The ratio of L to ro is an input parameter of our models. The gravity can be non-dimensionalized in terms of the ratio of sound speed to Alfven speed, i.e. the plasma beta. The x-coordinate lies in the plane of the solar surface.

4.3. Code testing

The code follows MHD evolution by means a two-step Lax-Wendroff method. On a VAX 11/750, evolution up to 6-7 Alfven crossing times, in a 32 X 52 grid, requires 3 hours of CPU time. To check the code, we first modelled a non-magnetic hydrostatic atmosphere, to ensure that after several acoustic wave crossing times, no spurious motions developed: in fact, the maximum amplitude of spurious flows in such cases turned out to be small, on the order of the round-off error of the machine. As a check of the specifically MHD aspects, we then inserted a magnetic field which in principle is current-free. We developed an algorithm which made minor adjustments to the field components at each point of the grid such that the numerically derived divergence and curl of the initial field remained zero within the round-off error of the machine. As this field structure evolved in time, the code again produced only very small velocities after several Alfven crossing times. The fact that several crossing times had elapsed also indicated that the code was correctly handling the boundaries, and avoiding spurious reflections from them.

4.4. Modelling of Reconnection Regions

Initially, the material is at rest, with zero perturbation to the magnetic field. The pressure is a function of both x and y, depending on the choice of magnetic field. The density is a function of y only, at t=0: it is taken to be a linearly decreasing function of y, with a variation by a factor of 10 from the bottom of the grid to the top. The initial choice of magnetic field, chosen to model the Harvey results (that X-ray bright points are random encounters of vertical flux tubes of opposite polarities) is a vertical field (Bx=0) with strength which is a sinusoidal function in x out to a distance xo; beyond xo, the vertical field is uniform. For our calculations, we have selected values of plasma beta 0.25, 0.50, and 0.75: these are chosen so as to allow the magnetic structure to evolve in a reasonable computer time. In all cases to date, we have chosen a unique value for the gravity parameter and for the ratio of L/ro. Magnetic Reynolds numbers for our calculations vary from Rm=5000 to 10000. These values are of course not as large as the actual values in the solar atmosphere, but they are chosen to be as large as possible, consistent with the available computer time. To investigate the effects of non-stratification, we have also run the beta=0.75 case with no stratification.

Our grid is a 32 X 52 box ranging from -0.1 to +3.0 in x, and from -0.1 to +5.0 in y. Reflection symmetry about the y-axis is assumed.

To initiate a flow, we introduce a localized region of enhanced resistivity occupying a circle of radius unity centered at y=2.5, x=0. Within this circle, the resistivity is larger than in the ambient medium by a factor which varies smoothly from unity (at the border of the circular region) to 100 (at the center of the circle). Outside the circle, the resistivity is uniform, and is equal to the inverse of the magnetic Reynolds number. The region of enhanced resistivity is meant to model, say, the onset of turbulence in the immediate vicinity of a magnetic reconnection site.

We have computed four stratified models (labelled 002, 003, 004, 005); the first three have Rm=5000 and beta = 0.75, 0.5, 0.25. Model 005 has beta=0.75 and Rm=10000. The non-stratified model (labelled 006) has beta=0.75, Rm=5000.

4.5. Results of MHD modelling

In presenting our results, we refer to time in units of Alfven crossing times, and we plot quantities only within a restricted subarea of the computational grid. First we discuss results from model 002. In this case, the model was followed up to time t=6, by which time, the flow velocities in our grid had risen to about 0.3 (in units of the initial Alfven speed at the origin). In Fig. 42 we present the velocity field at this time: the flow is mainly upwards across the top of the grid. At the same time, the contours of magnetic field strength are as shown in Fig. 43. The creation of a magnetic island along the y-axxis is apparent: there are two x-type neutral points above and below the island, due to reconnection in the region of enhanced resistivity centered at y=2.5, x=0. Strong currents have developed at the x-type neutral points (see Fig. 44, which shows contours of electric current density at time t=6). Density contours (Fig. 45) at the same time show that the upper x-type neutral point is a region of locally perturbed density. A quantity which is of basic interest to us is the mass flux in the grid. Contours of the mass flux are shown at time t=6 in fig. 46: as expected, most of the flows are concentrated along the magnetic neutral line, particularly in the vicinities of the x-type neutral points. We will return shortly to a consideration of the integrated mass flux from our grid. Other quantities which we plot out for each step of time include the local temperature, the local pressure, the local electric fields. But the results in Figs. 42-46 give the reader a flavor for the results which emerge from our modelling.

Figures analogous to 42-46 are presented in Figs. 47-51 for the case of zero stratification (model 006). In this case, the integrations were carried forward somewhat farther in time before plotting (to more than 7 Alfven crossing times): at that point in time, the maximum velocity in the grid was 0.18 (in units of the Alfven velocity), i.e. smaller than in the stratified case. The magnetic field contours (Fig. 48) are more symmetrical than before, but they still exhibit the formation of an o-type magnetic island surrounded by two x-type neutral points. Current densities are again maximal at the x-type neutral points (Fig. 49). The mass density distribution is different now, with a "hole" forming at y=2.5, where the density drops to about 80% of its initial (uniform) value (Fig. 50). The mass flux is more symmetrical (Fig. 51), as expected.

Now we turn to plots which show how the various energy fluxes alter with time. The non-stratified case will be discussed first (file number 006). In Fig. 52 we show how the mass flux per unit length per unit time varies with time. In all subsequent plots, curves labelled T refer quantities which have been integrated across the top of the grid, B to the bottom of the rid, R to the right-hand side of the grid, and D is the difference between T and B. In the non-stratified case, T and B cancel out, so that the D curve in Fig. 52 is essentially zero: there is no net mass flow in this case. Similarly, the net energy in this case cancels out to zero (Fig. 53), as does the net kinetic energy flux (Fig. 54), the thermal energy flux (Fig. 55), and the magnetic energy flux (Fig. 56). As regards the total energy and mass contained within the grid, we show the behavior of the various components in Figs. 57-60: in Fig. 57, T denotes thermal energy: this peaks in the early stages (due to energy released in reconnection), but then decreases as expansion out of top and bottom causes cooling. The total kinetic energy builds up with time (Fig. 58): there is motion in the grid both out of the top and the bottom. The total energy, after initial transients, settles down to almost a constant value (Fig. 59), as does the total mass (Fig. 60). Thus, as expected in the absence of stratification, the symmetry of the situation results in little net outflow from the region of integration.

In contrast, let us now consider the run labelled 002, which is identical to the run we have just been discussing in all respects except one: stratification is included in run 002. In Fig. 61, we now see the mass fluxes in the stratified case: now the flux out through the top is not cancelled by the flux through the bottom, and as a result, the net flux (curve D) becomes positive at times later than about 3 Alfven crossing times. In this case, therefore, the magnetic configuration is ejecting mass upwards through the top boundary. This is precisely the signature we have detected in certain solar bright points: upflow from a magnetic bipolar region which forms when two vertical flux tubes of opposite polarity come into contact.

The total energy flux (Fig. 62) also shows a net increase at later times, due to the predominance of the flow of energy out through the top (curve T). Similarly, net flows of kinetic and thermal energy through the top boundary also occur (Figs. 63, 64). The magnetic energy, on the other hand, shows essentially zero flux in the vertical direction, although flux is lost through the right-hand side (curve R, Fig. 65). As regards the integrated energies in the grid, the situation is qualitatively similar to the non-stratified case: in Fig. 66, note that the thermal energy has a peak at early times (again due to energy release from reconnection), followed by a decrease (due to expansion). Integrated kinetic energy increases as time goes on (Fig. 67), but now the total energy and total mass no longerr settle down to asymptotic values (see Figs. 68, 69). Note that the percentage change in total mass in the grid in Fig. 69 is in absolute terms: the actual mass decreases as time progresses towards the right.

We have similar plots for the other runs we have done (003, 004, 005). They all show qualitatively similar behavior as for run 002: the presence of stratification apparently ensures that there will be a net mass flow upwards out of the grid area.

This result is in contrast to our earlier attempts to create mass outflow from closed loops of magnetic flux: we do not show any results from these extensive modelling efforts here, but they were uniformly negative. It was the receipt of K.L. Harvey's report after these negative results had been obtained which led us to try another magnetic configuration. Thus, there may be a physical difference between the two classes of HeI dark points in Harvey's classification: one may find it easy to cause mass outflows, the other may find it essentially impossible. In this regard it is interesting that in fact Harvey has found a better empirical correlation between solar wind properties and HeI dark points which are random encounters of flux than between the solar wind and ephemeral active regions.

5. Conclusions

We believe that our data plus our modelling efforts yield a consistent picture: mass can be ejected from X-ray bright points provided that the magnetic topology is favorable. Not all X-ray bright points will have the favorable topology. In fact, the early SMM data suggest that inflows are predominant in bright points in active regions and in the quiet sun. But our study of coronal holes suggests that the population of "correct" bright points may be more prevalent in coronal holes than in the general surface of the sun. This is pertinent, perhaps, to an understanding of why coronal holes may be favored sites of solar mass loss.

Our only regret is that the coronagraph on SMM did not succeed in detecting the "far-field" signatures of individual ejecta from bright points at the base of polar plumes.

```
ANA>V26544 DOPPLER 2/3/85 1952 UT  ↑U

ANA>TY,MAX(DOP),MAXLOC(DOP),MIN(DOP),MINLOC(DOP),$CONTOURS
 9.48383E+02     17     18-1.26255E+03     11      4-1.10463E+03-7.88779E+02
-4.72932E+02-1.57084E+02 1.58764E+02 4.74612E+02 7.90459E+02
ANA>
```

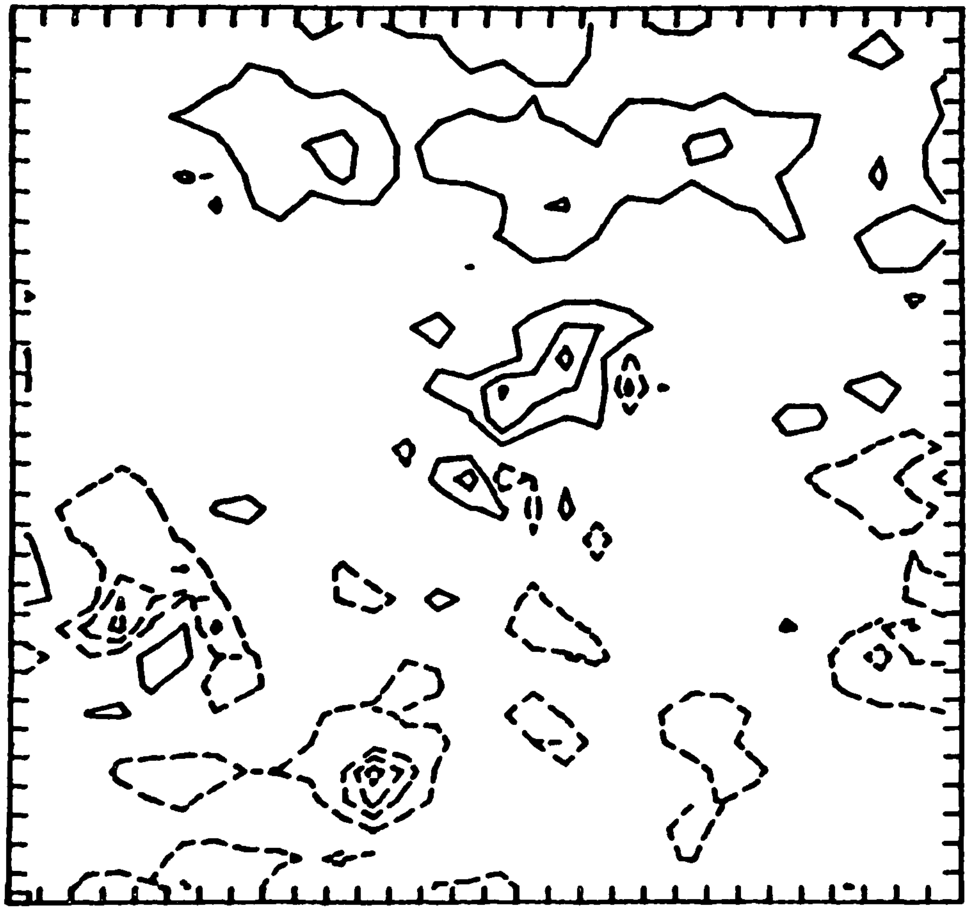

+126

-107

Fig. 1 Exp. 26544

```
ANA>V26544 INTENSITY  2/3/85  1952     ↑U

ANA>TY,MAX(INT),MIN(INT),MAXLOC(INT),MINLOC(INT),$CONTOURS
 5.79455E+03 1.77965E+02    11     4     3    19 5.79149E+02 1.38152E+03
 2.18389E+03 2.98626E+03 3.78863E+03 4.59100E+03 5.39337E+03
ANA>
ANA>
```

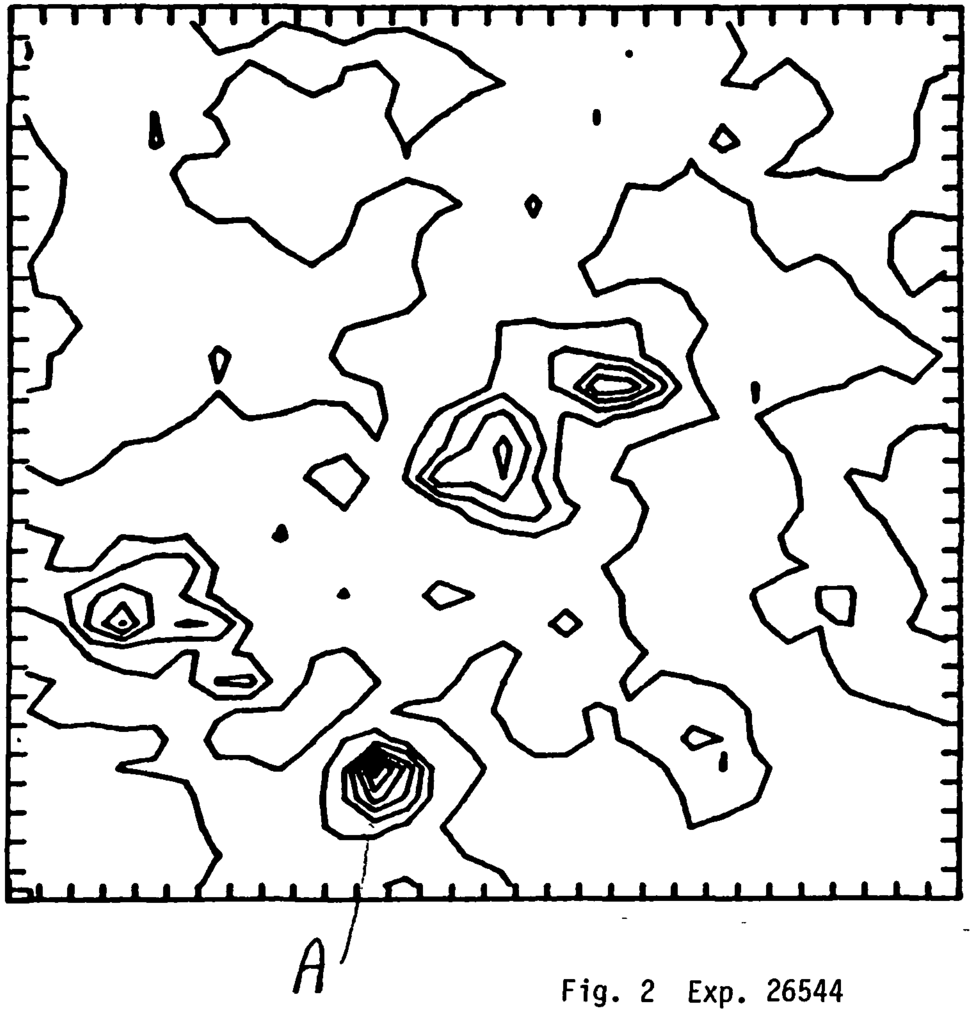

Fig. 2 Exp. 26544

```
ANA>TY,MAX(DOPR),MAXLOC(DOPR),MIN(DOPR),MINLOC(DOPR),$CONTOURS
 9.20263E+02     17     18-1.17819E+03     11       4-1.02830E+03-7.28521E+02
-4.28742E+02-1.28963E+02 1.70816E+02 4.70595E+02 7.70373E+02
ANA>V26544 DOPPLER CORRECTED 2/3/85 1952 UT
```

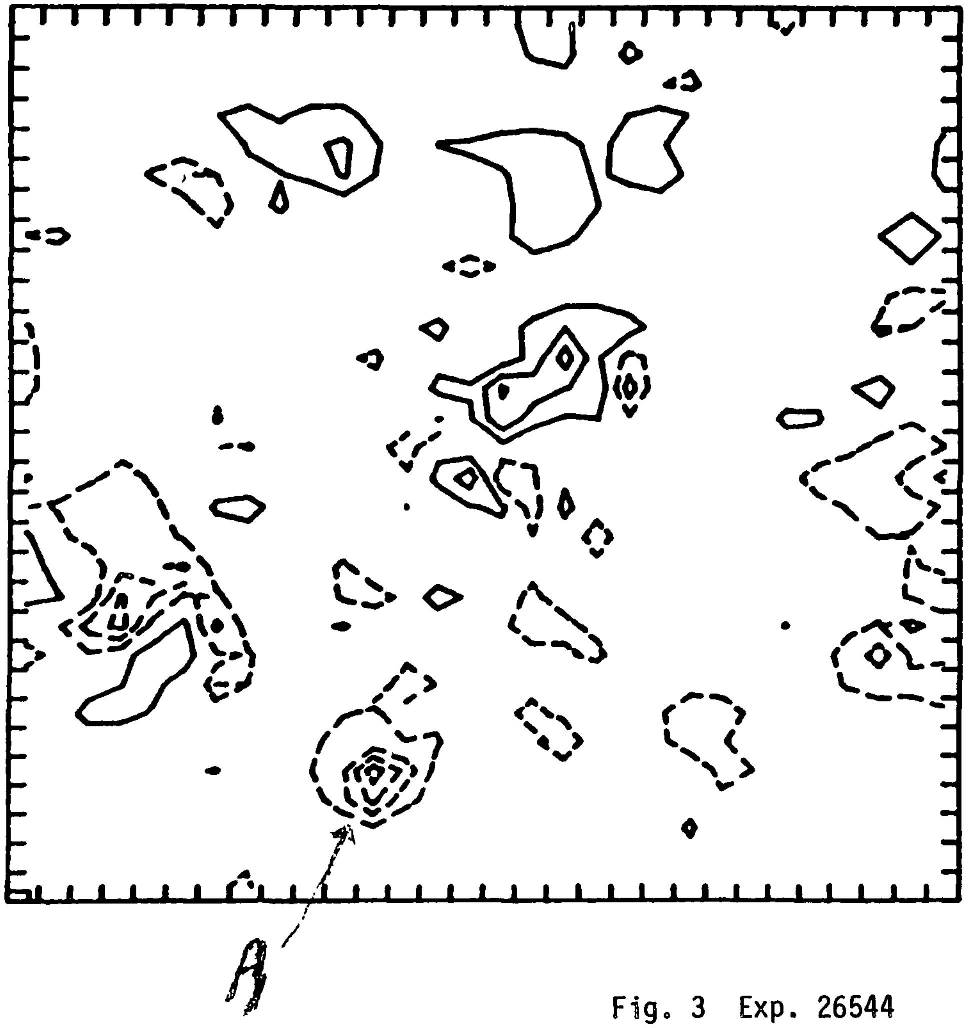

Fig. 3 Exp. 26544

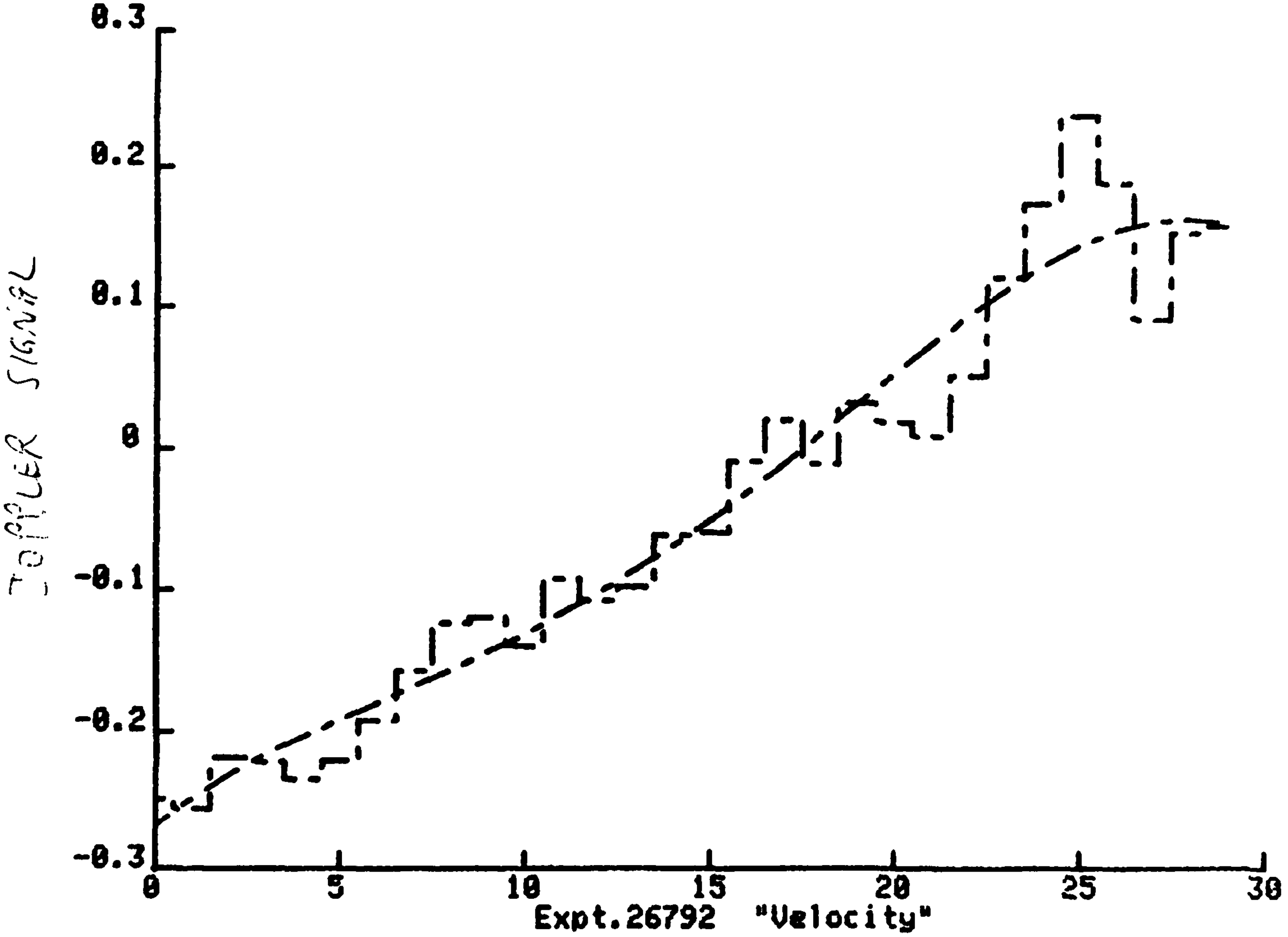

Fig. 4 Exp. 26544

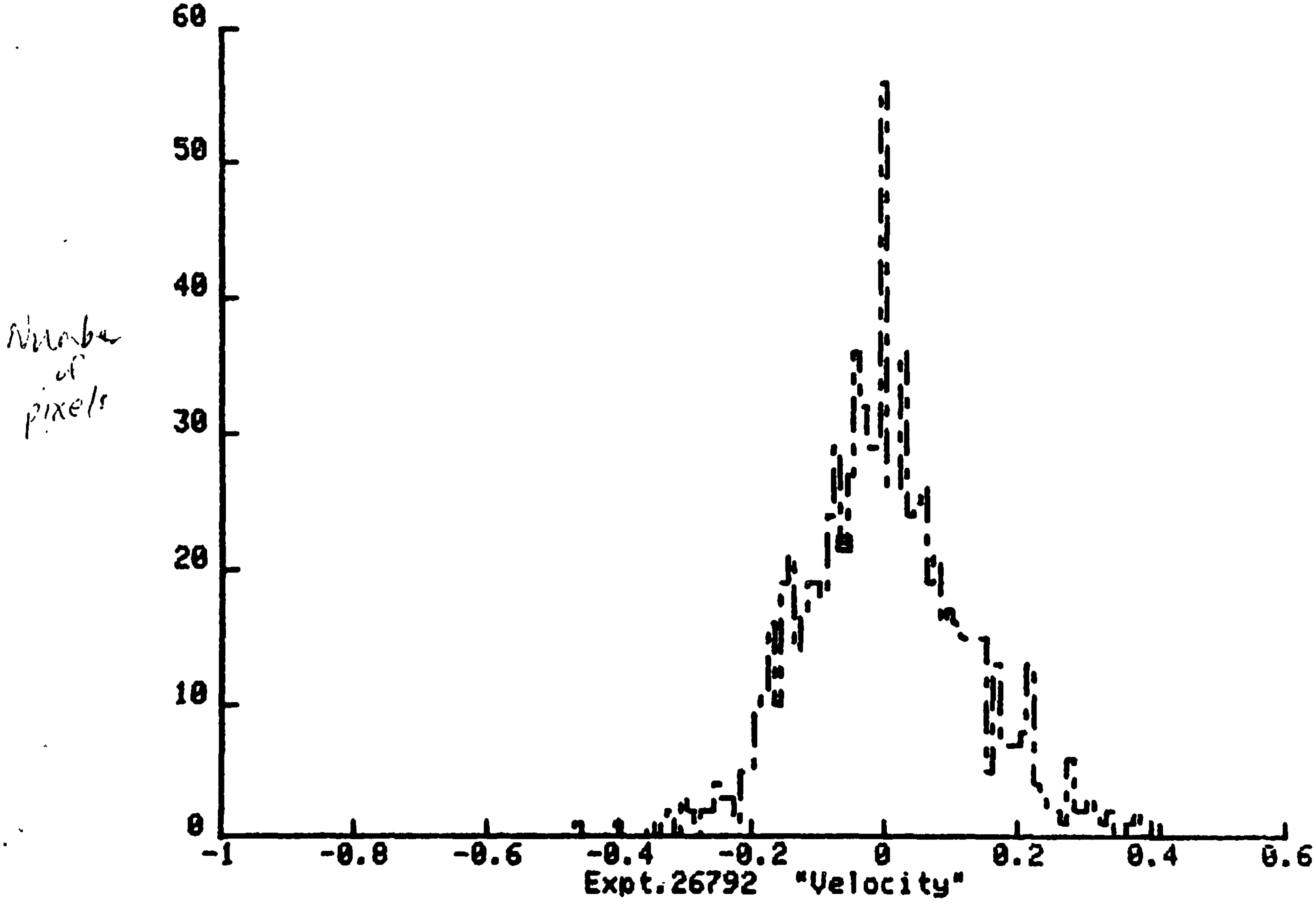

Fig. 5 Exp. 26544

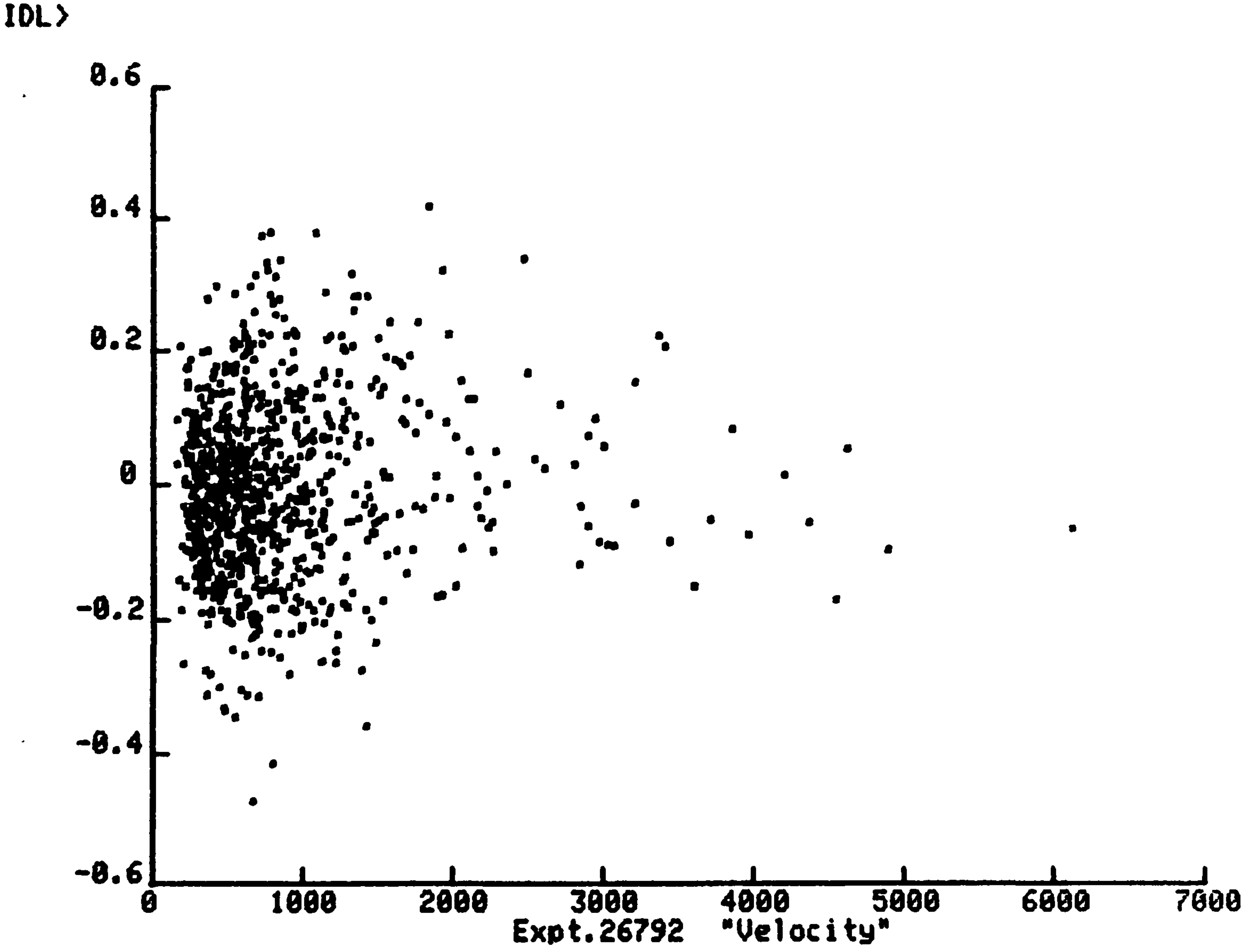

Fig. 6 Exp. 26544

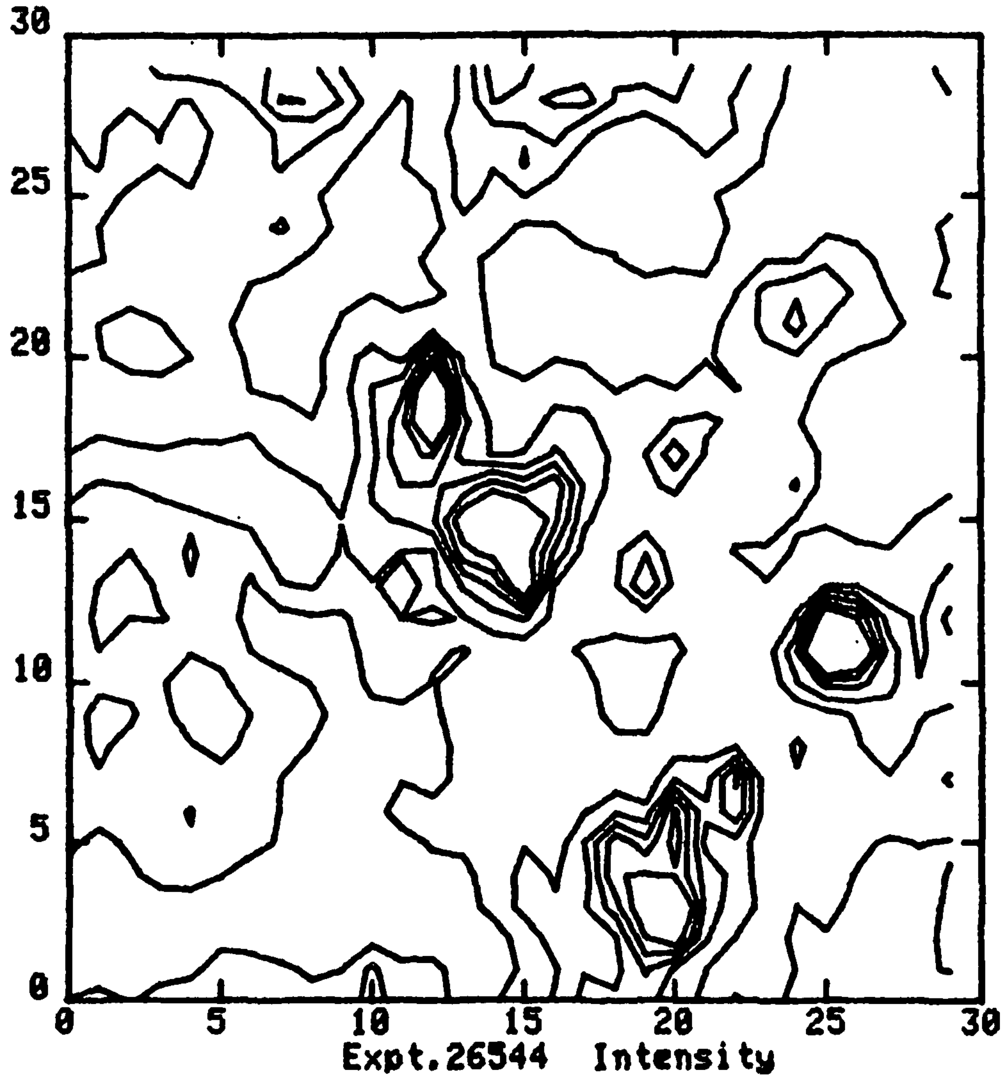

A'

Fig. 7 Exp. 26544

IDL>

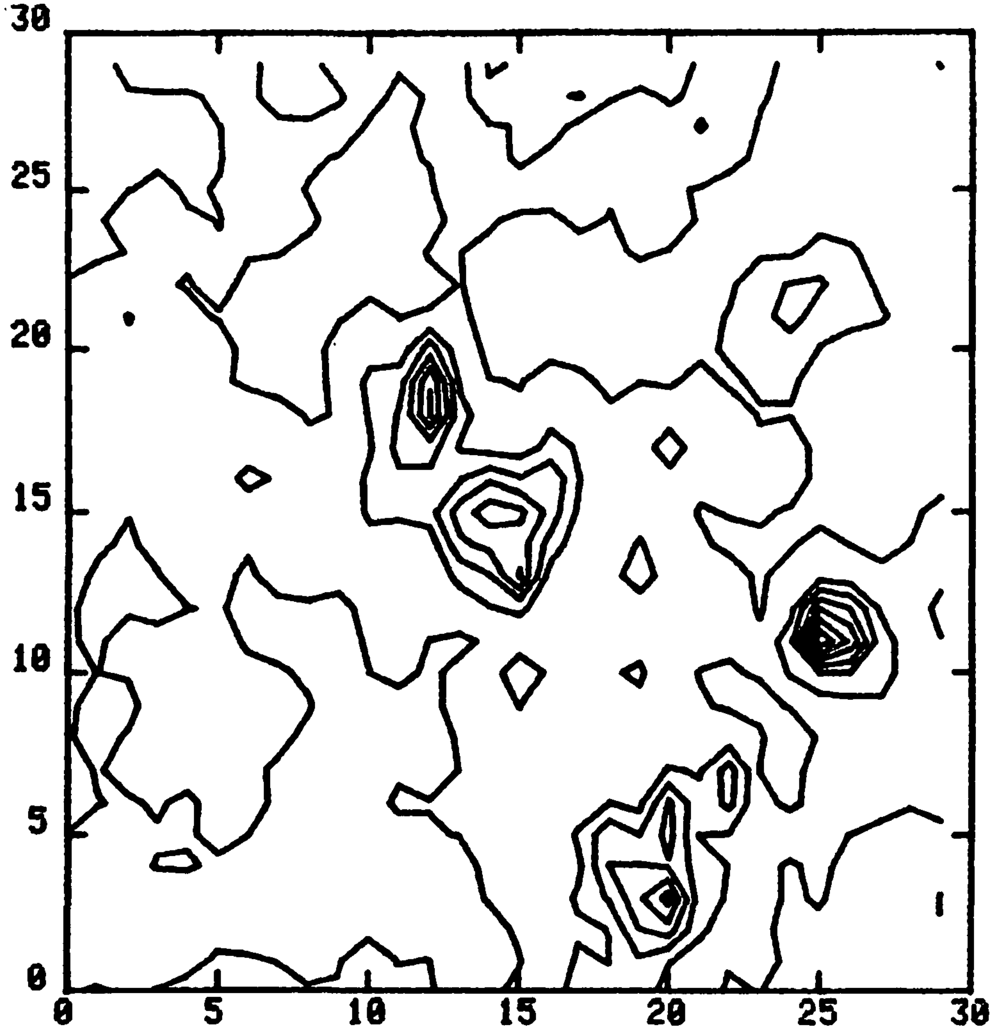

26544

Fig. 8 Exp. 26544

IDL>

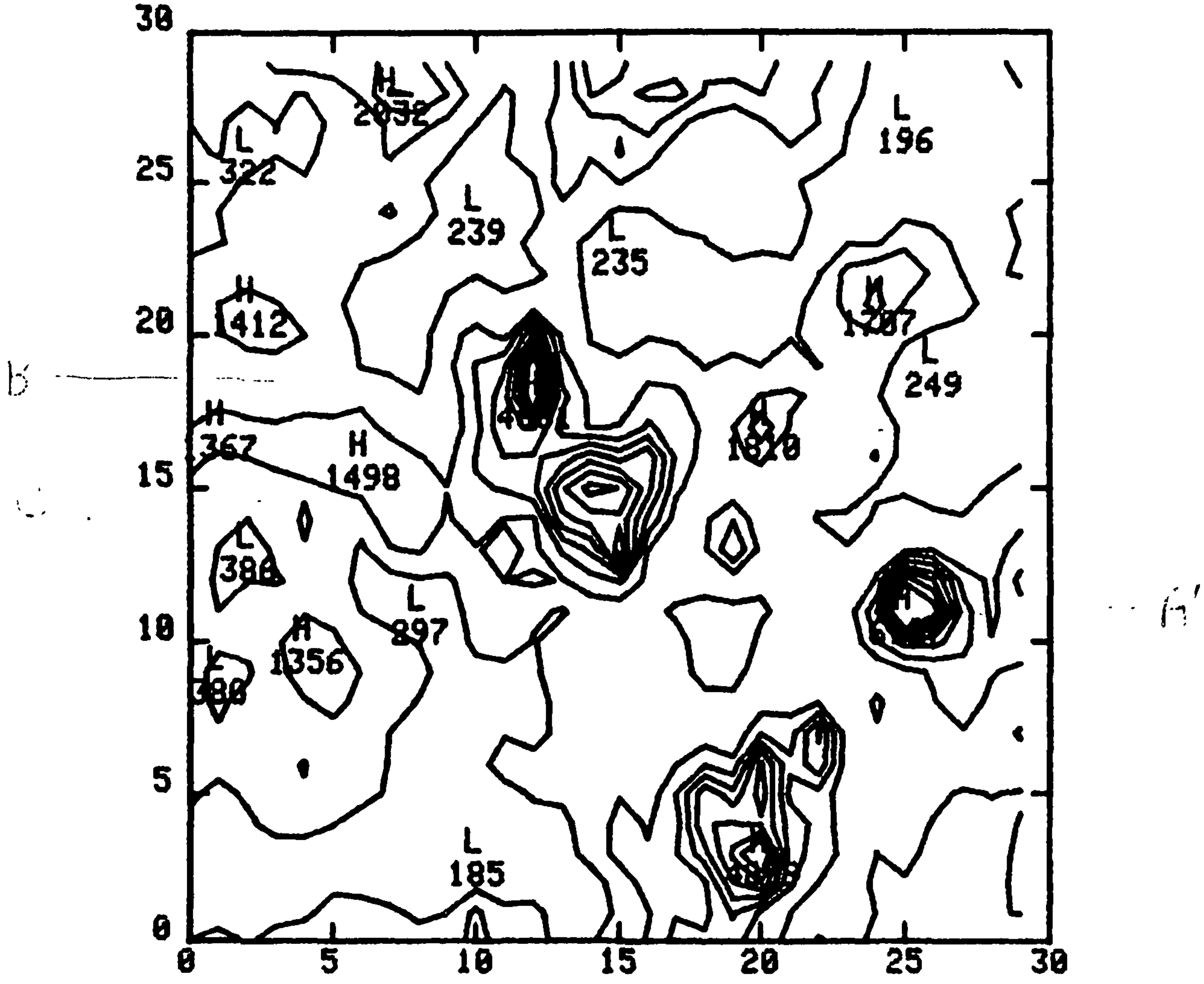

Fig. 9 Exp. 26544

IDL>

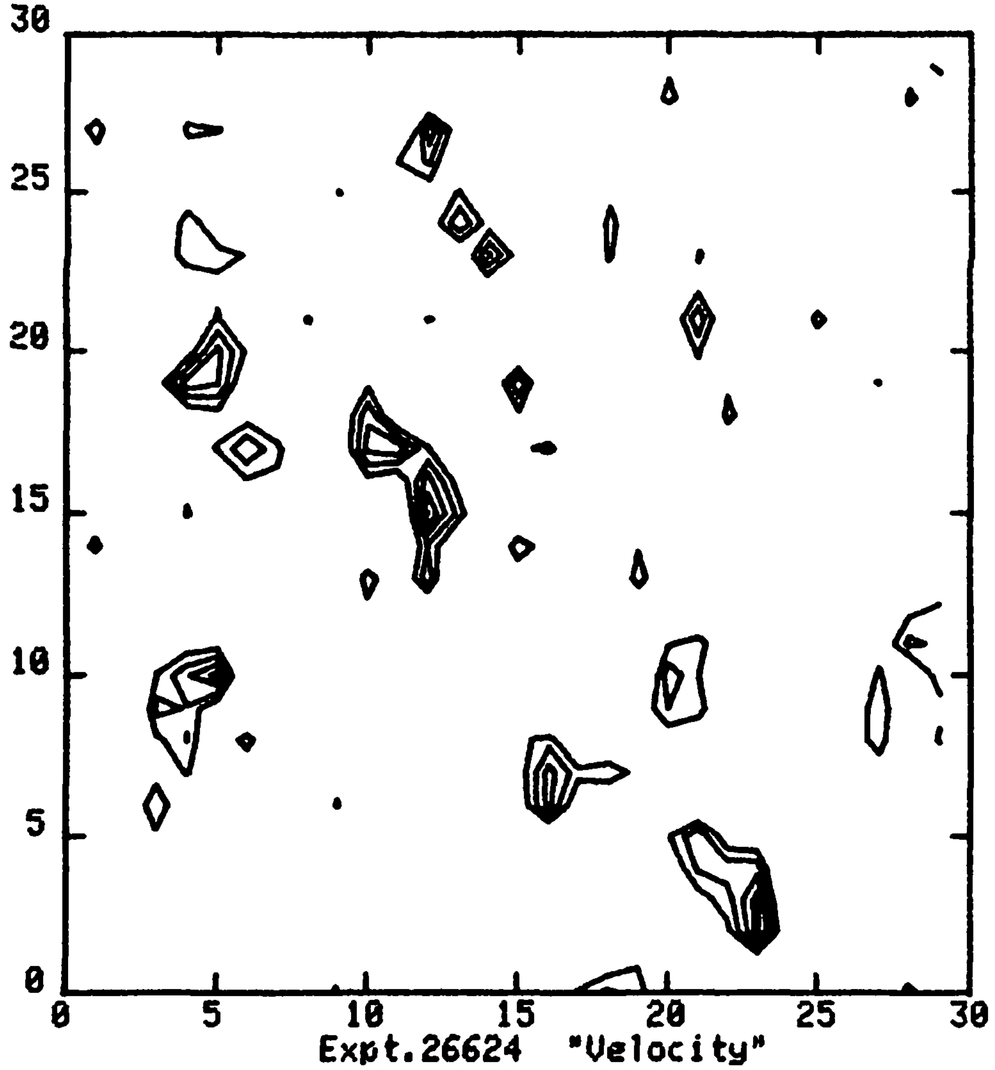

Fig. 10 Exp. 26544

```
IDL>CONTOUR,V0,
```

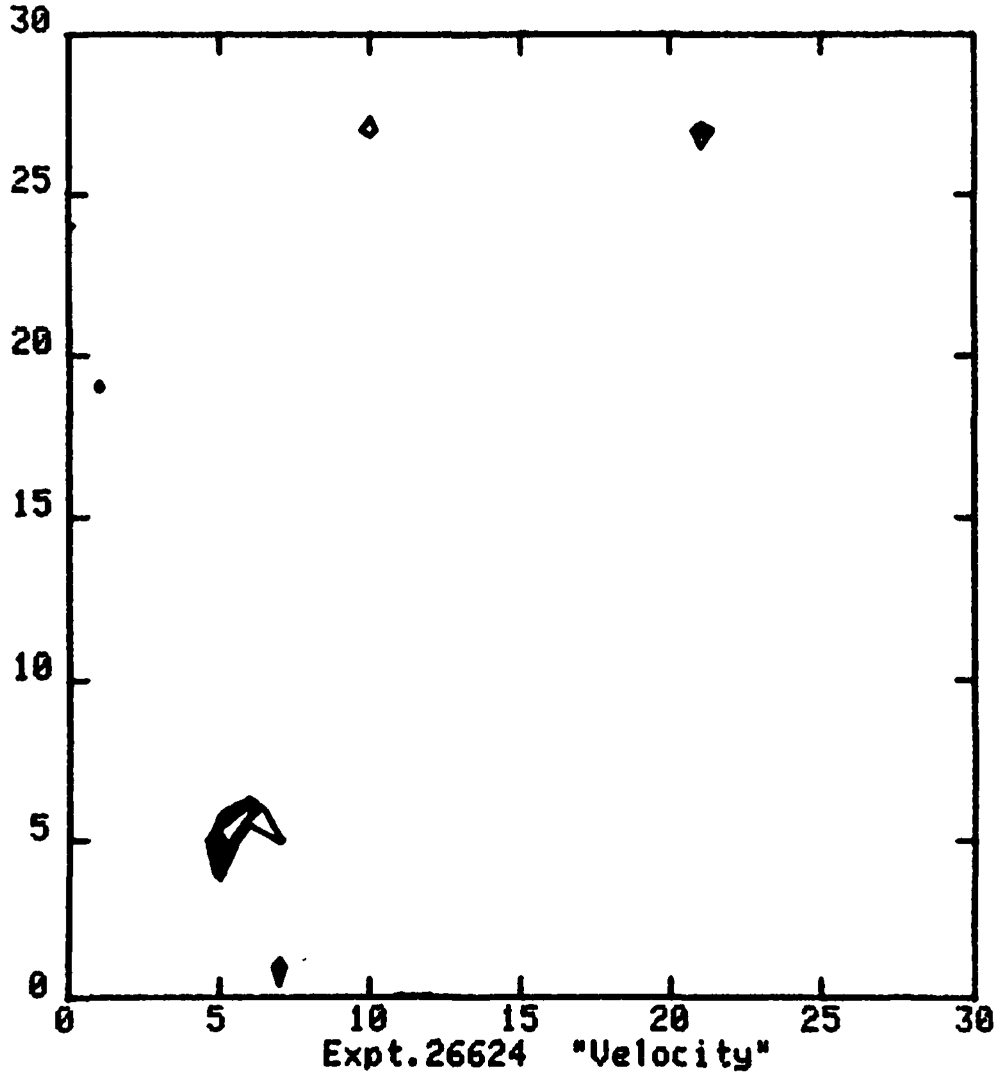

Fig. 11 Exp. 26544

IDL>

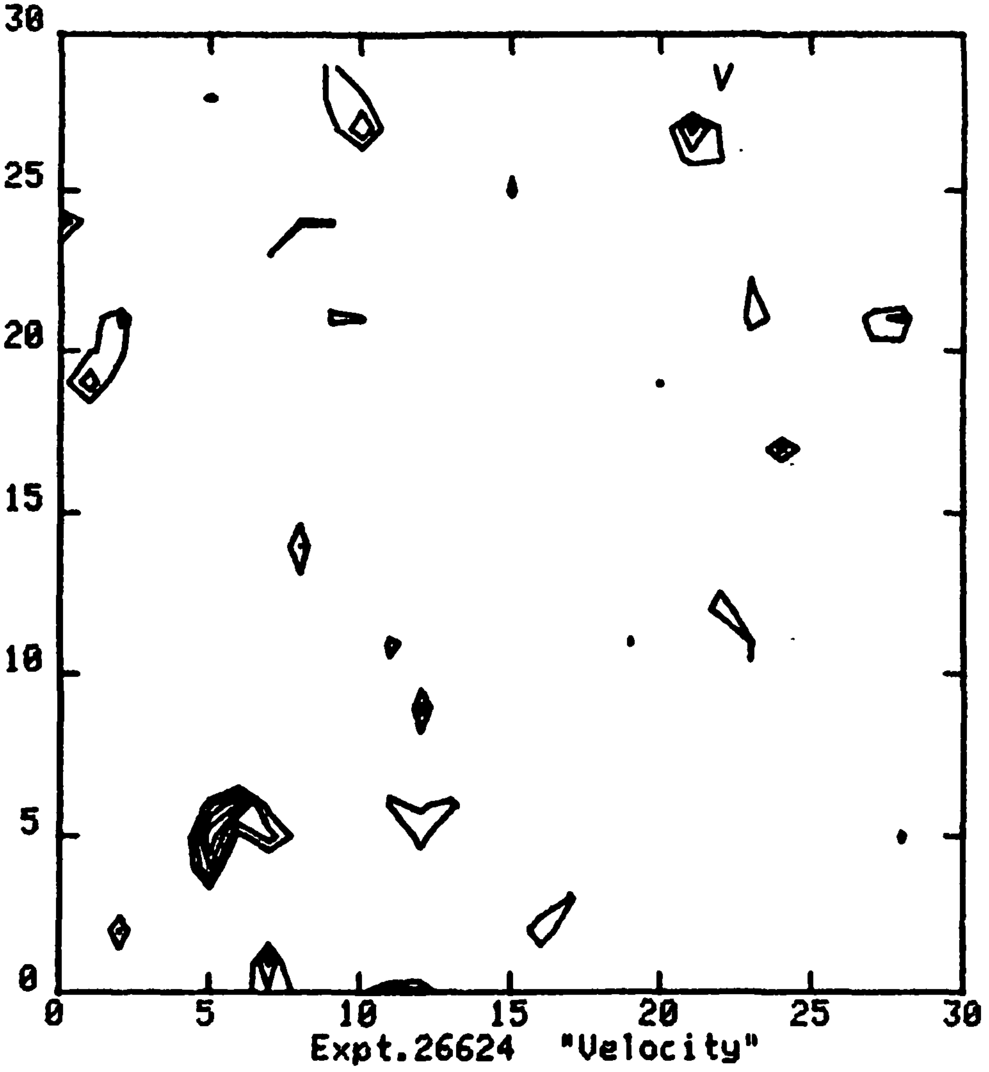

Fig. 12 Exp. 26544

IDL>

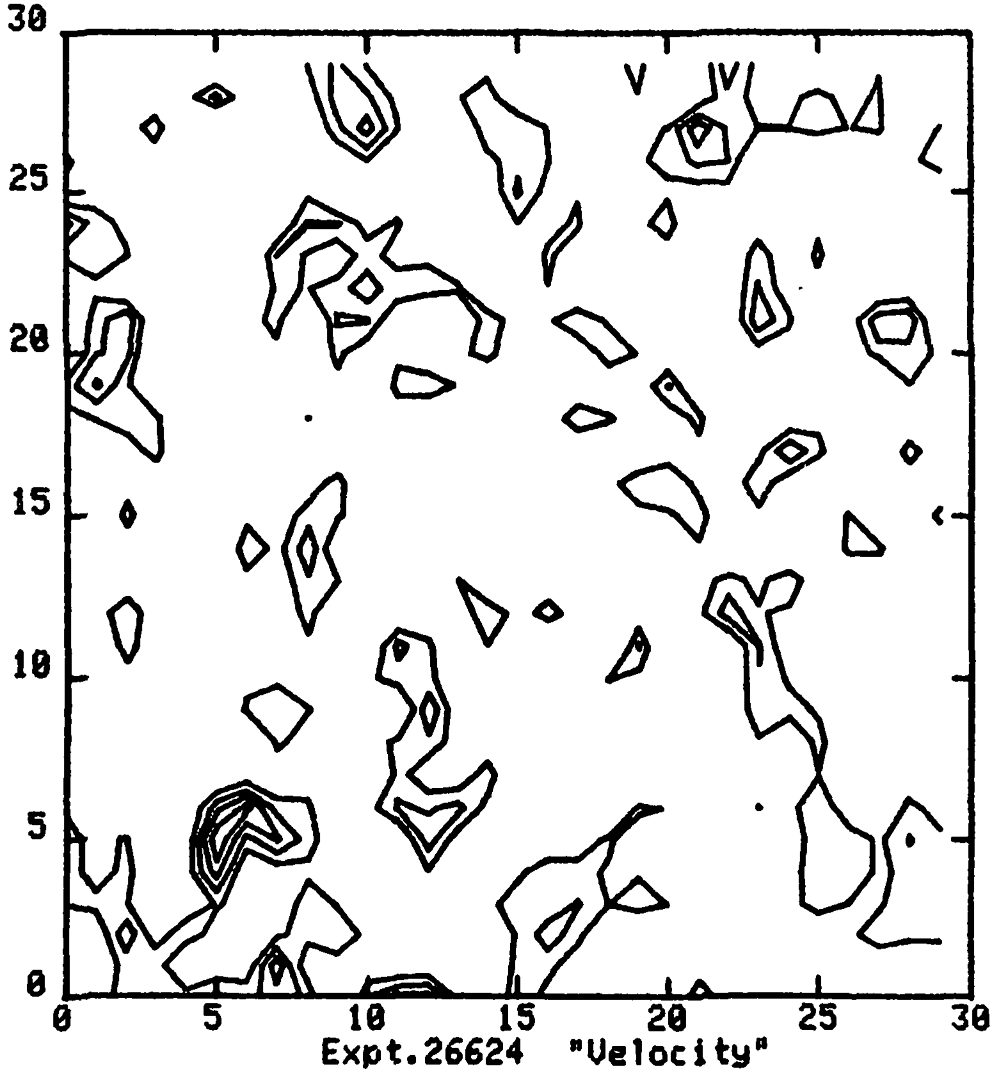

Fig. 13 Exp. 26544

2544

IDL>

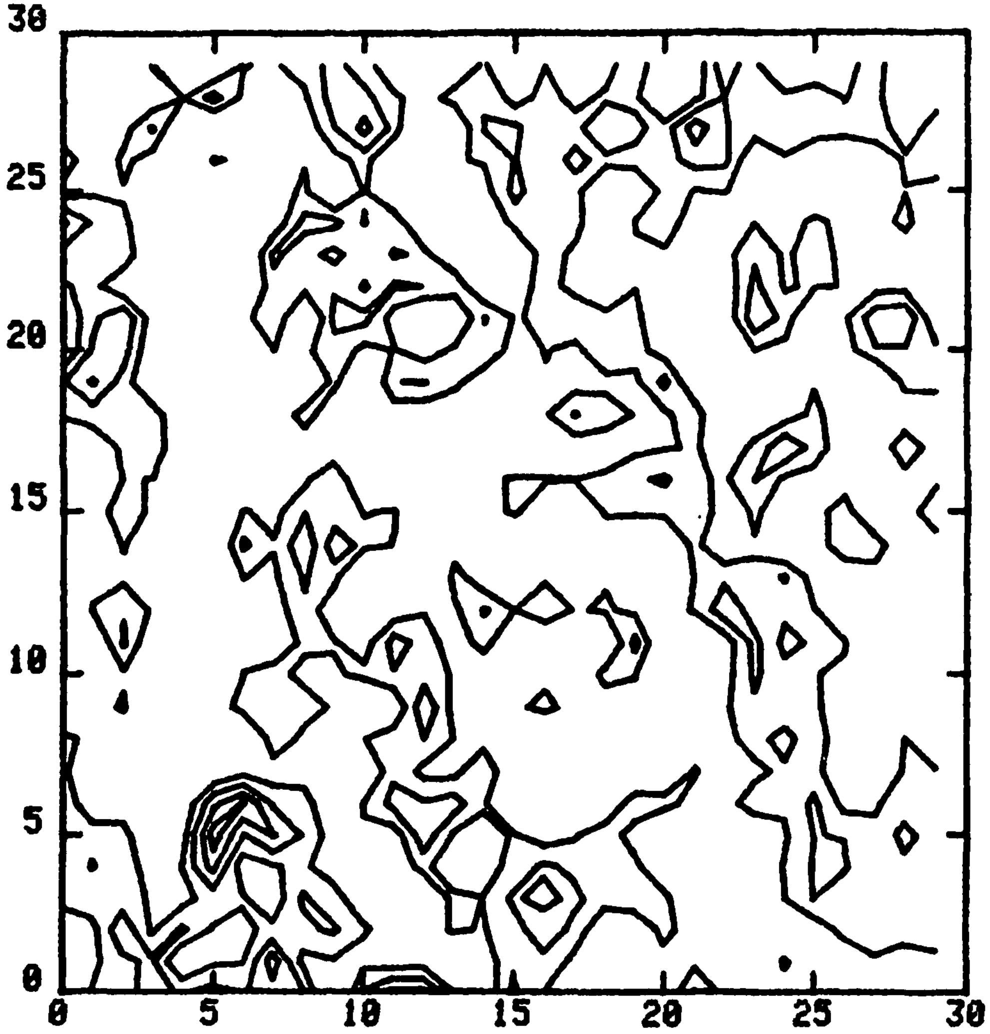

Fig. 14 Exp. 26544

IDL>

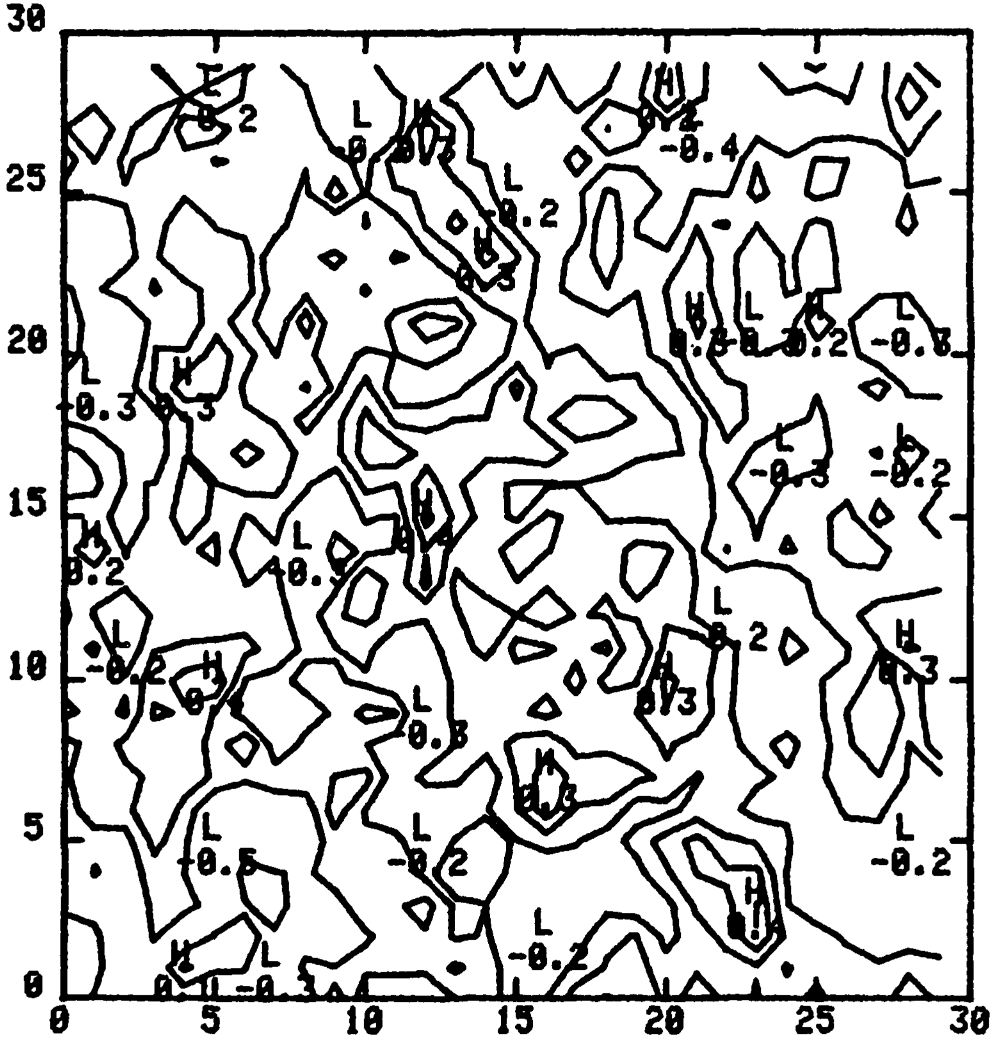

Fig. 15 Exp. 26544

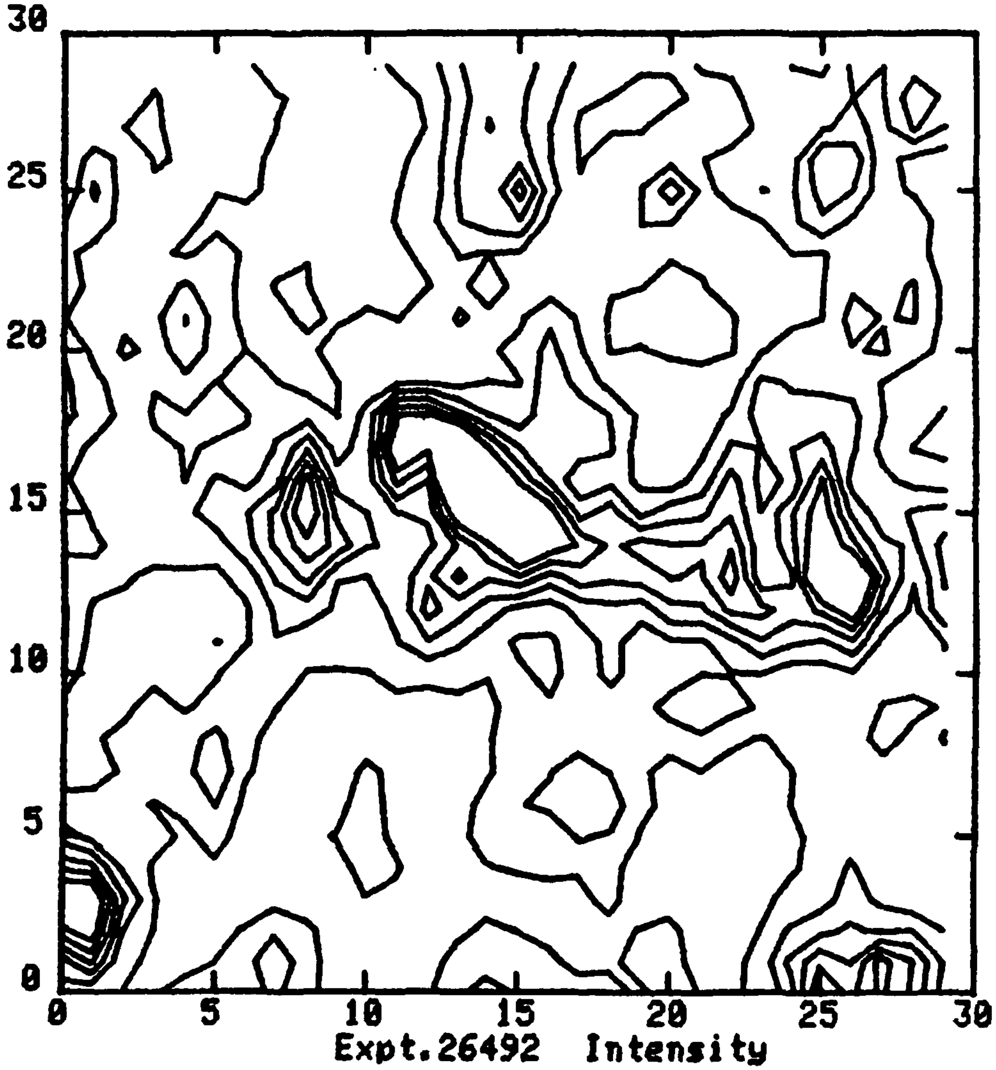

Fig. 16 Exp. 26492

IDL>

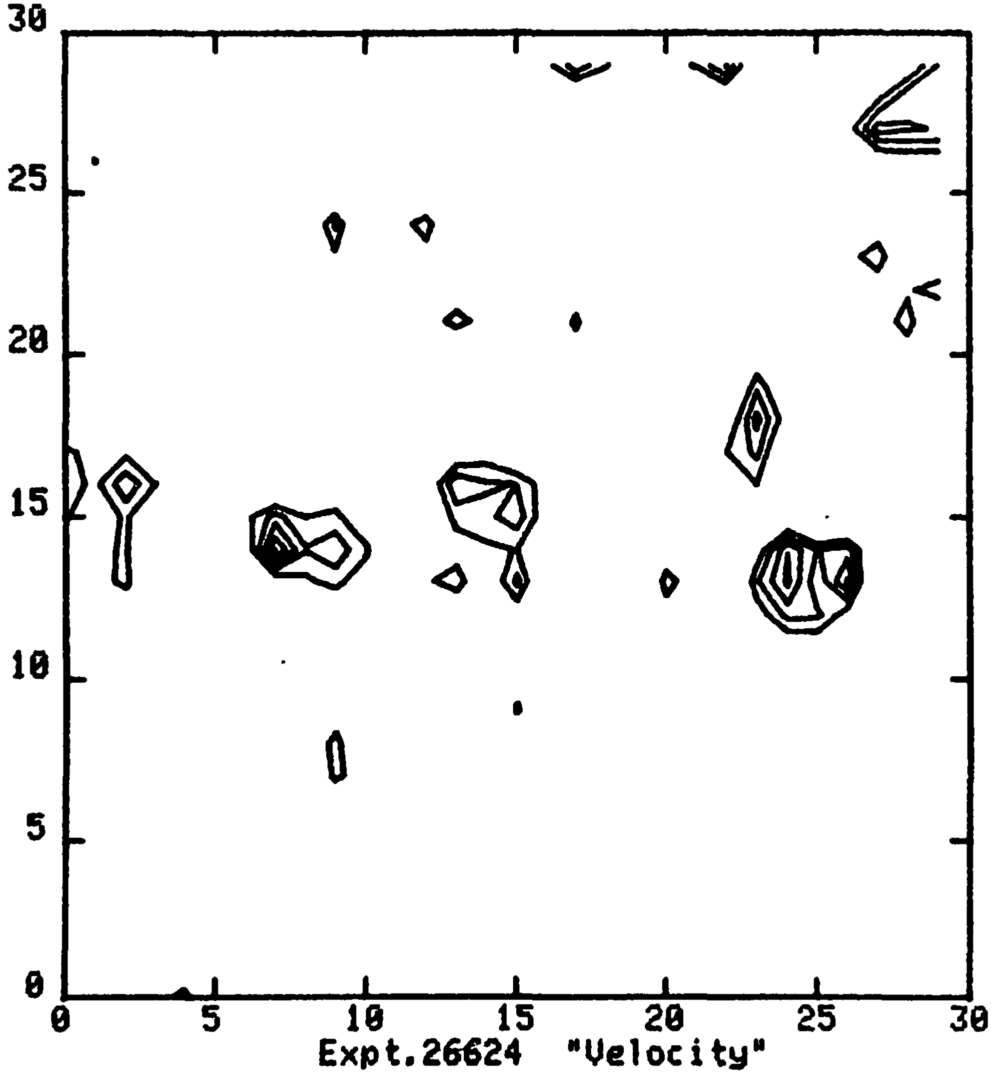

Fig. 17 Exp. 26492

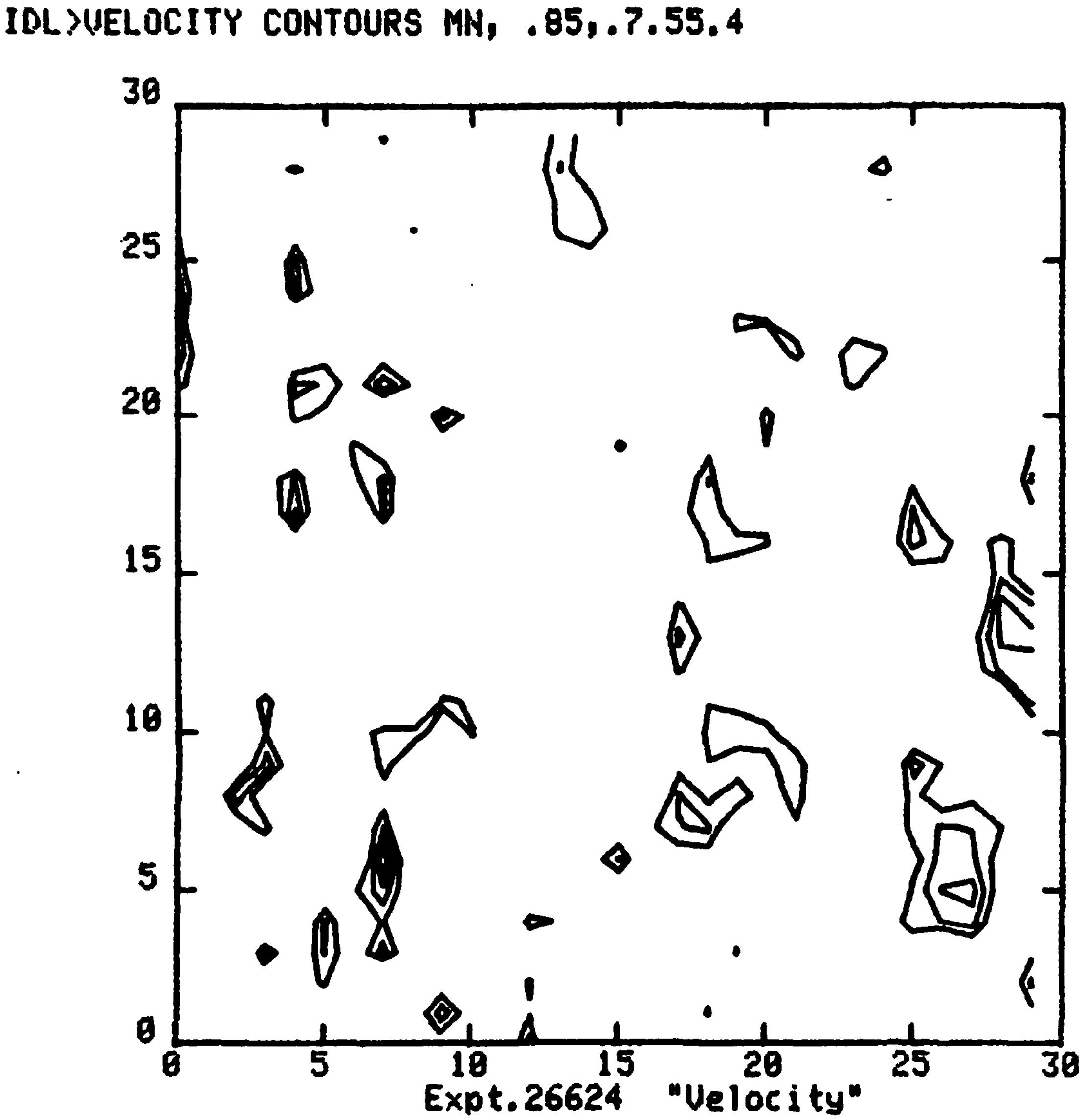

Fig. 18 Exp. 26492

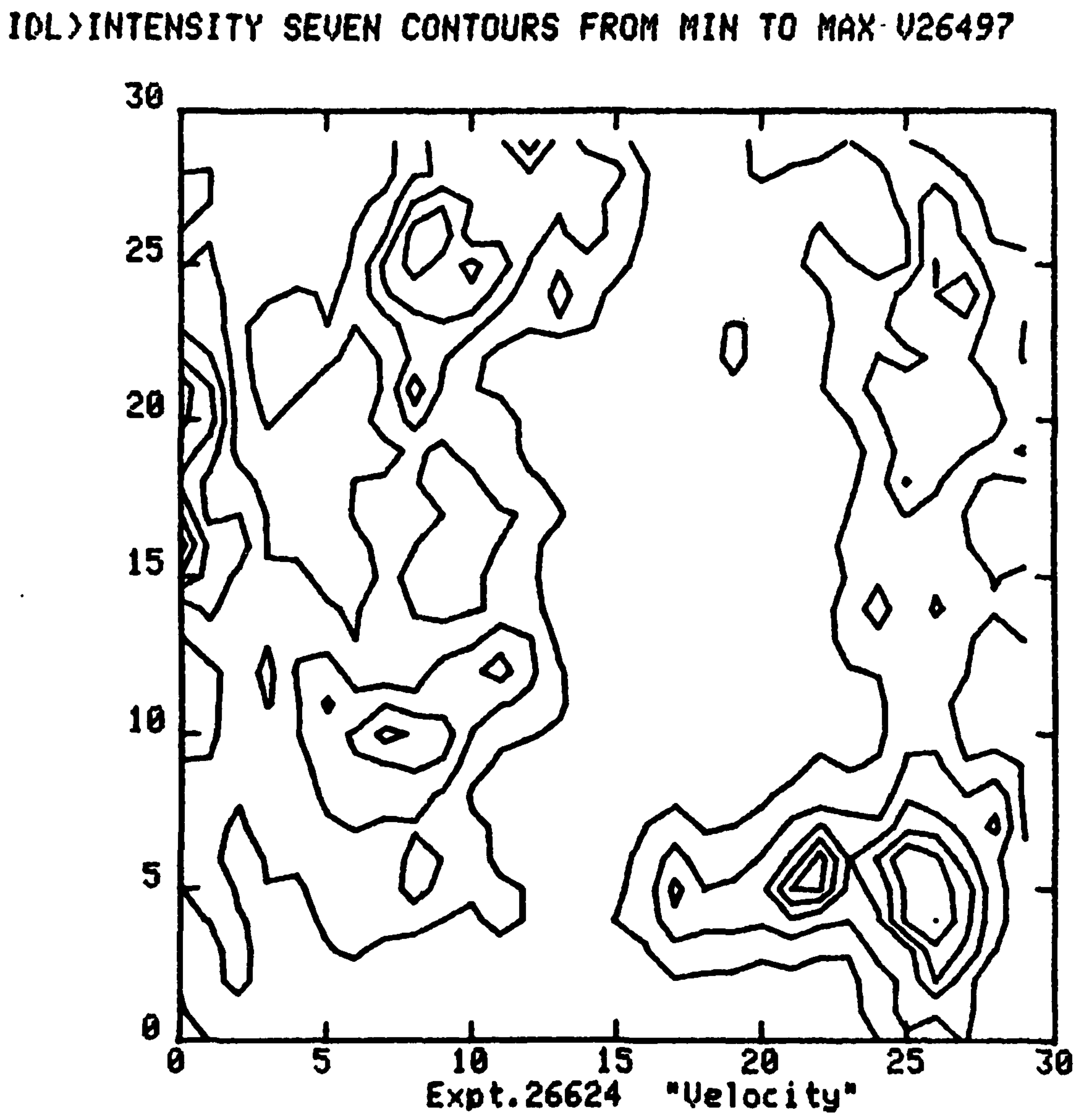

```
IDL>INTENSITY SEVEN CONTOURS FROM MIN TO MAX V26497
```

Fig. 19 Exp. 26497

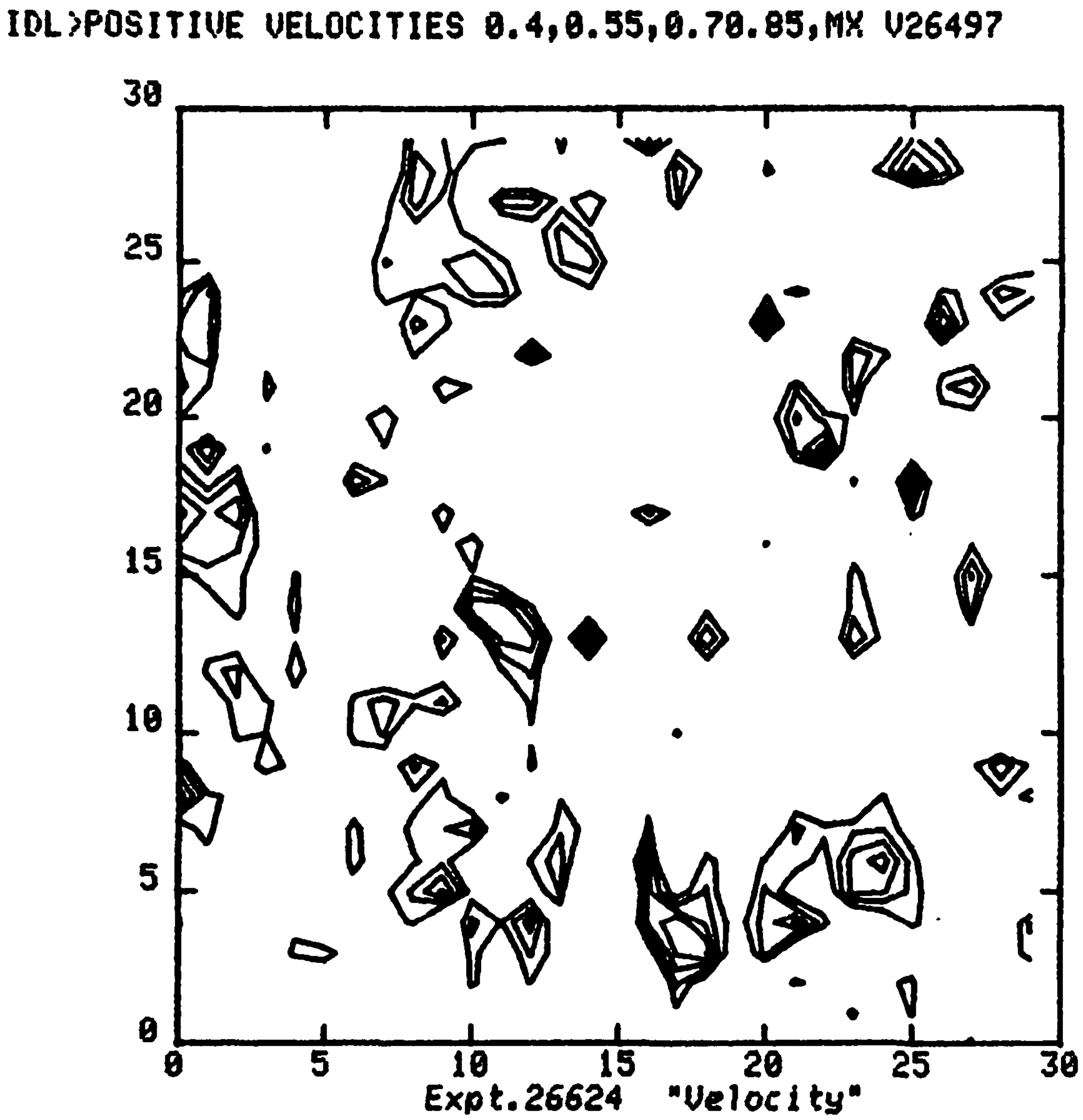

Fig. 20 Exp. 26497

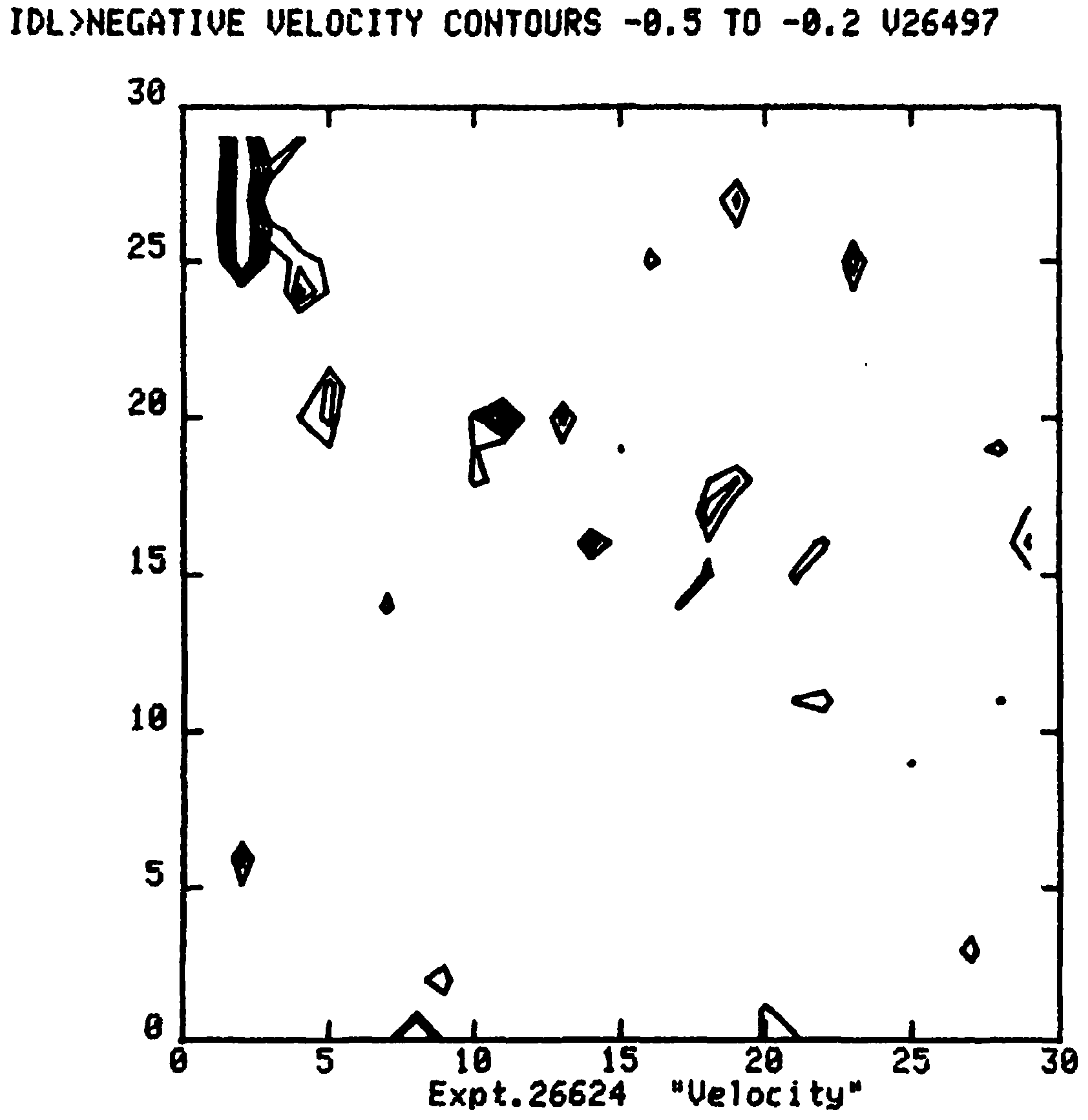

Fig. 21 Exp. 26497

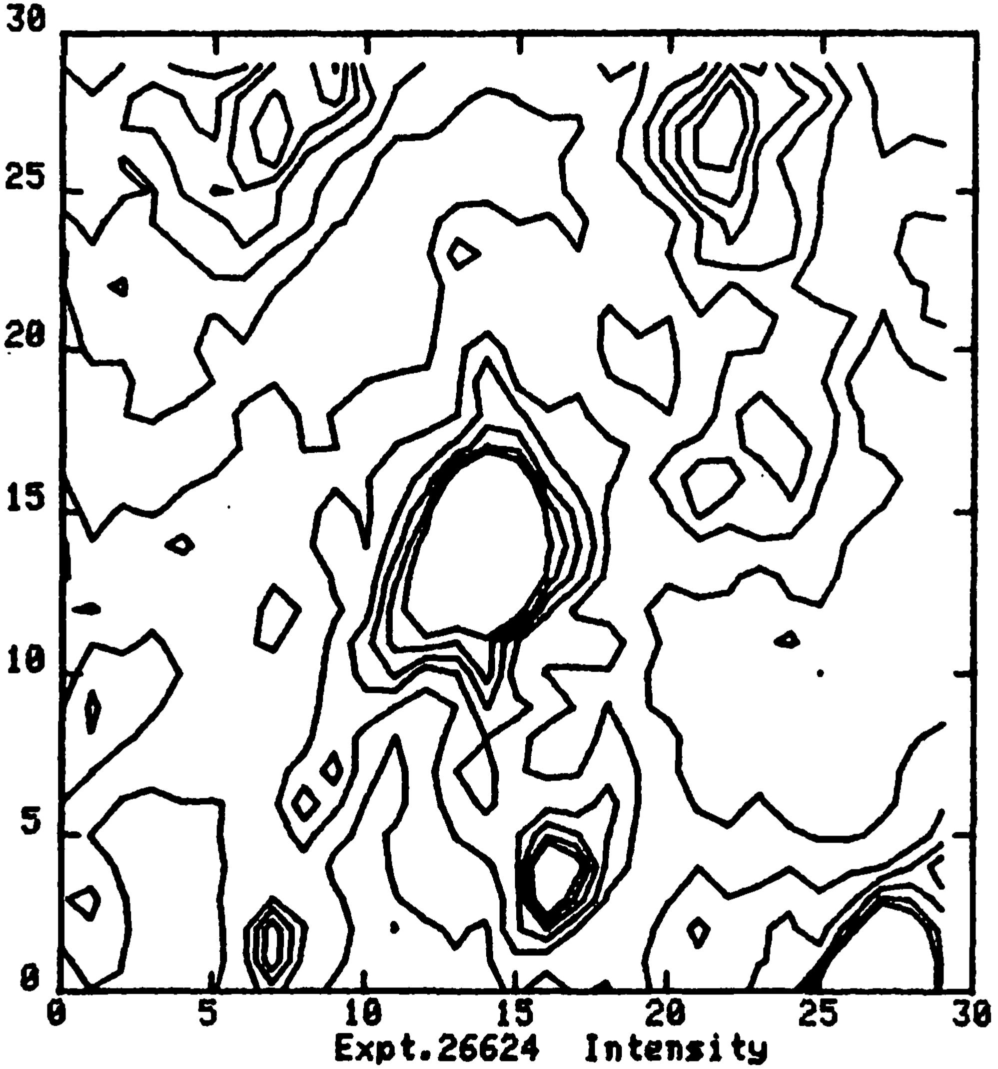

Fig. 22 Exp. 26624

IDL>

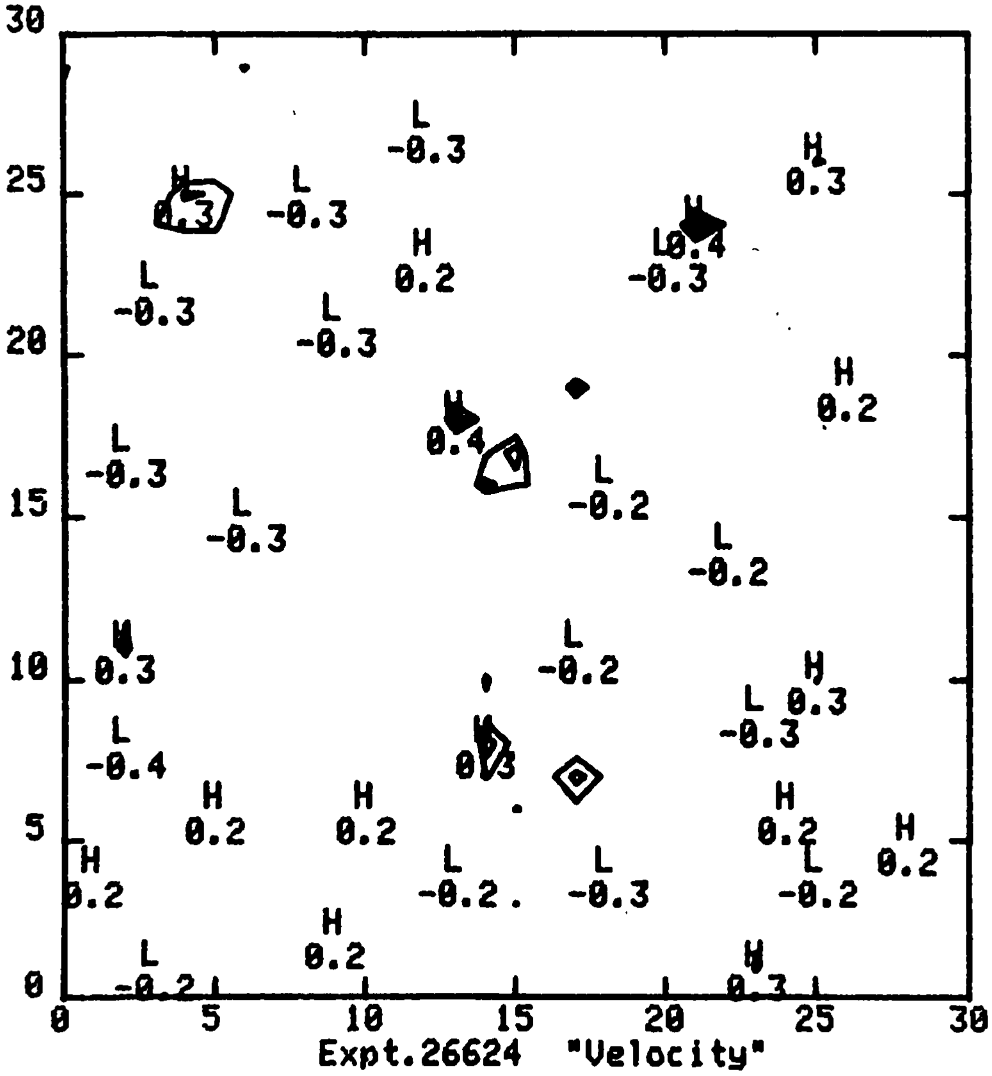

Fig. 23 Exp. 26624

IDL>

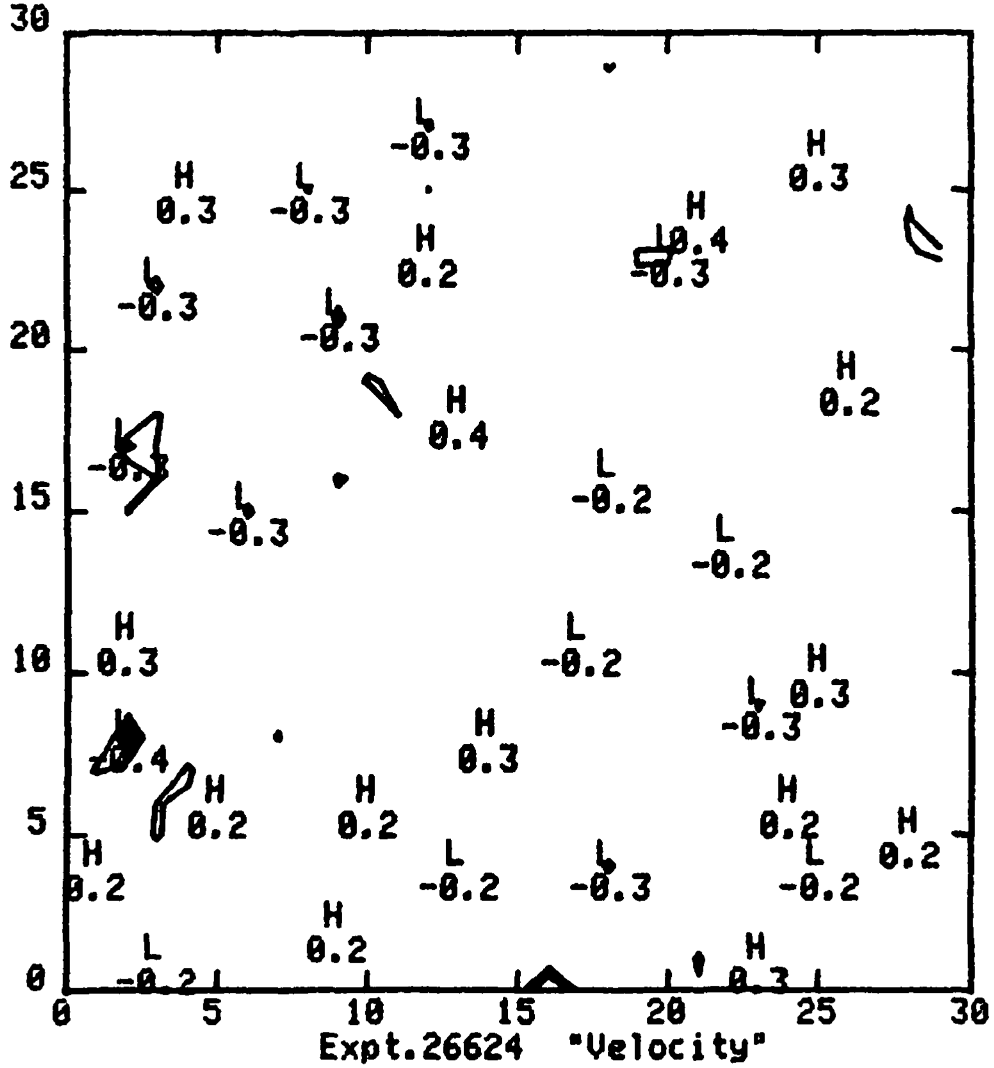

Fig. 24 Exp. 26624

IDL>INTENSITY 26629 7 EQUAL CONTOURS

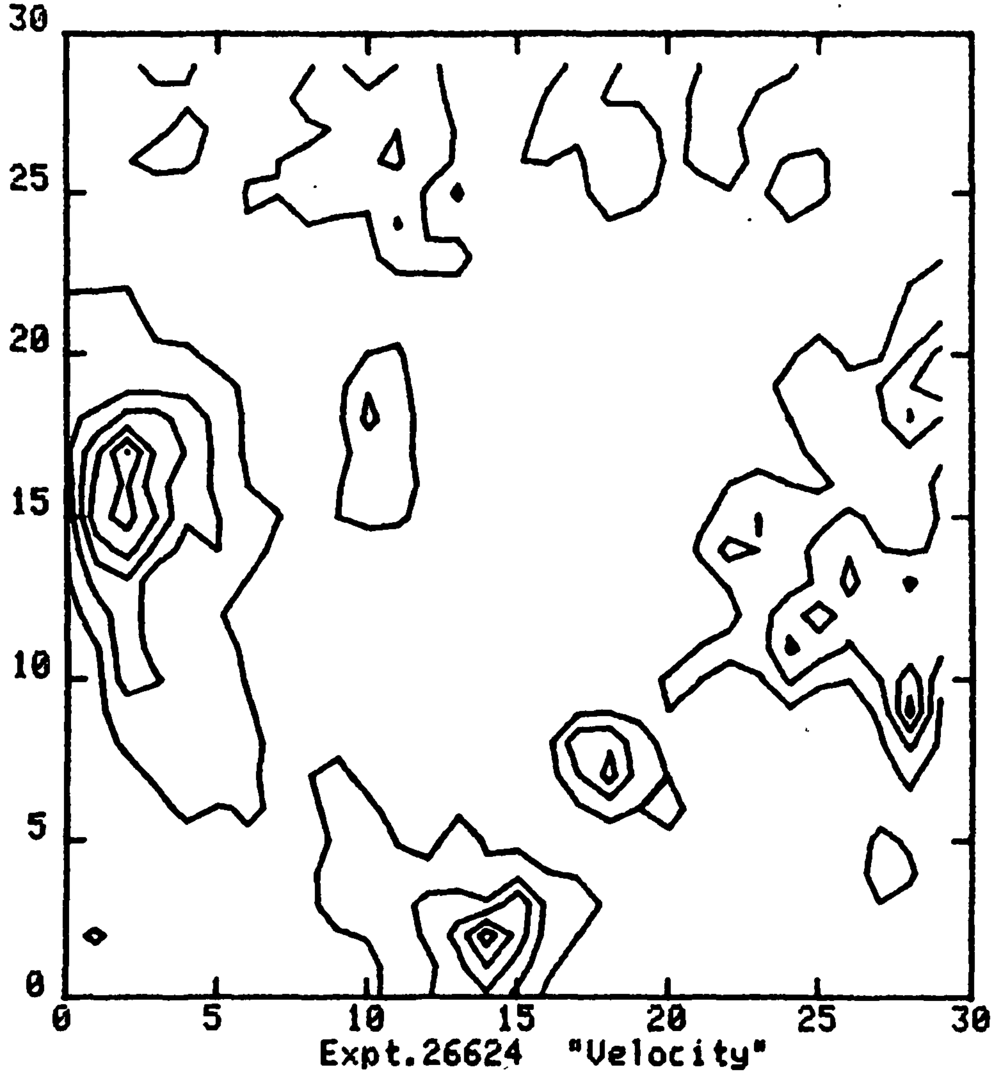

Fig. 25 Exp. 26629

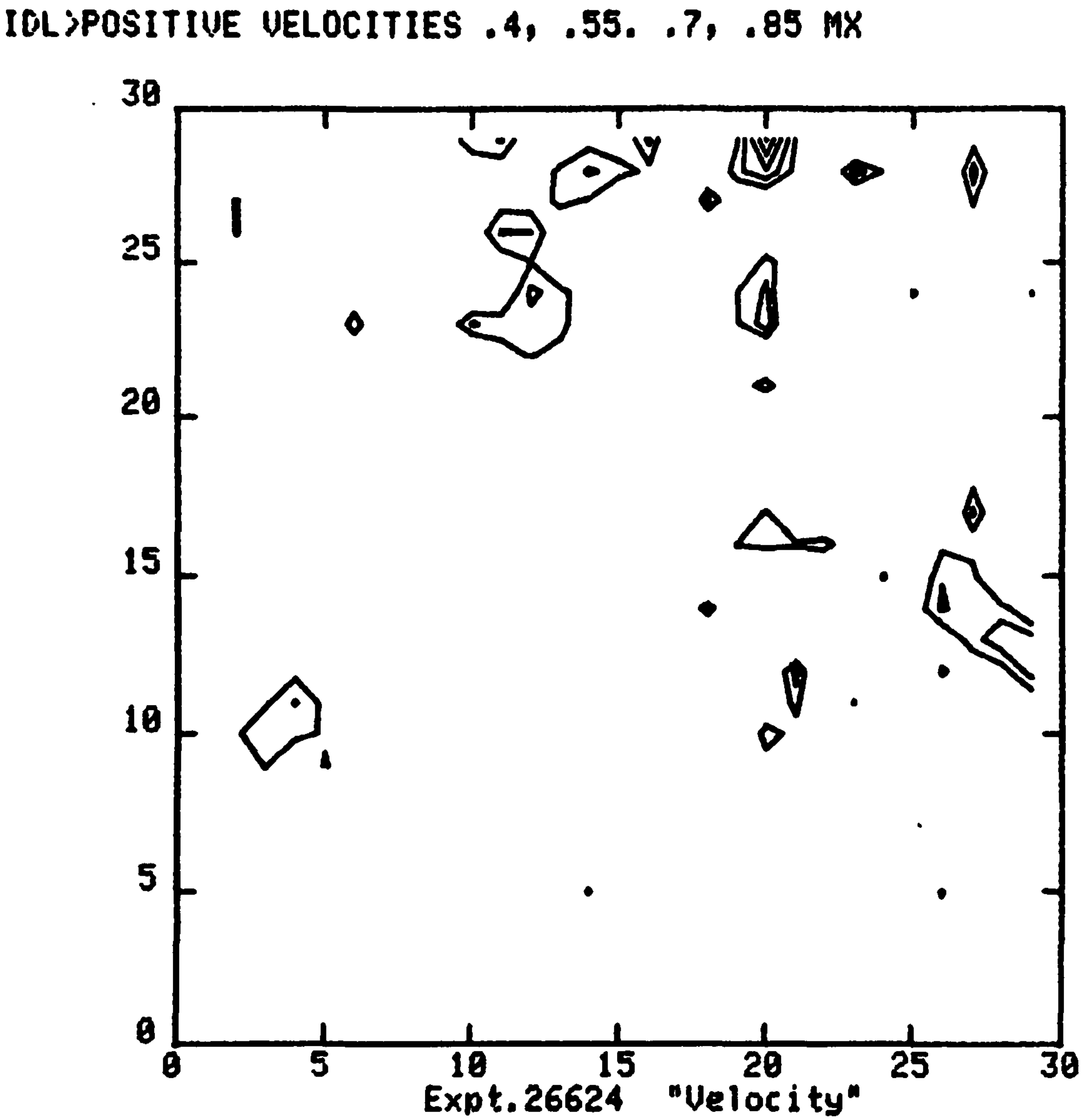

Fig. 26 Exp. 26629

IDL>NEGATIVE VELIOCITIES V26629 MN .85 .7 .55 .4 MN

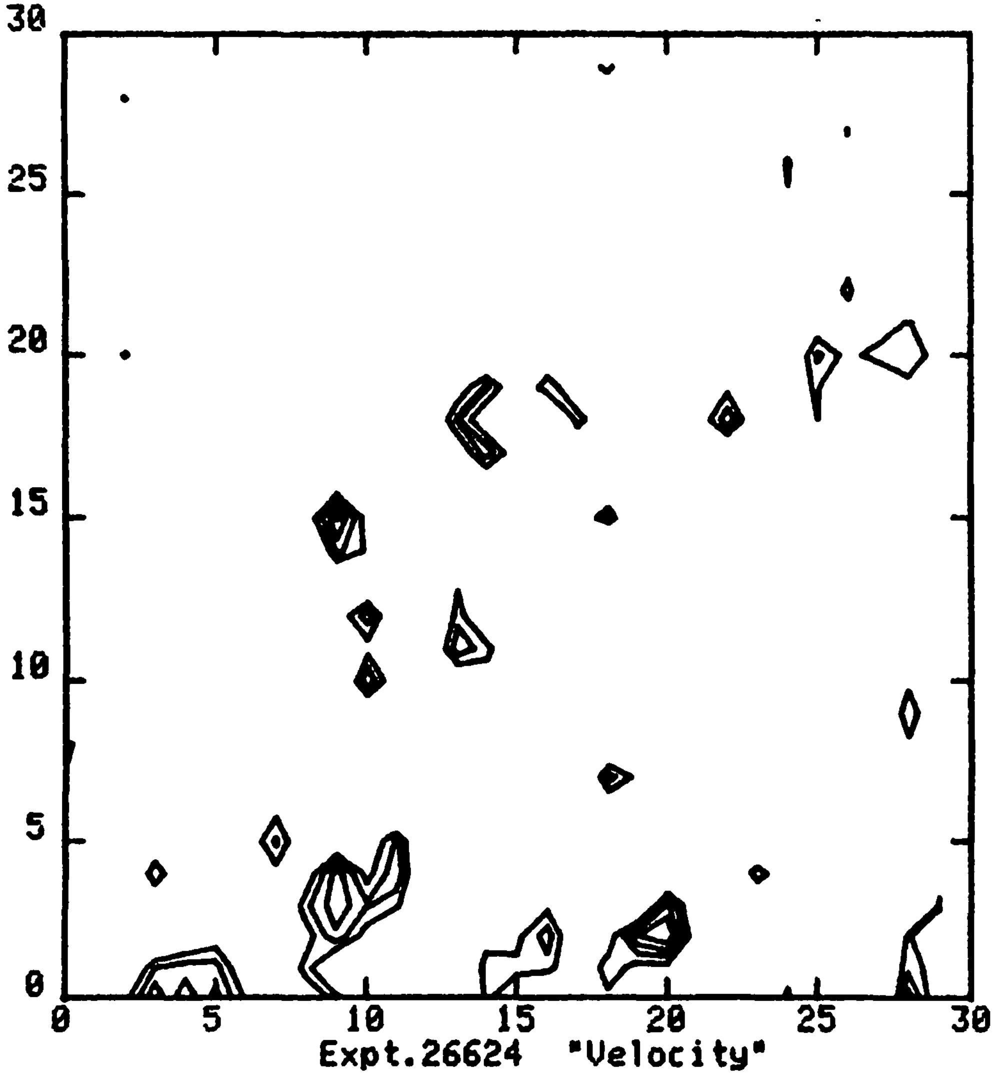

Fig. 27 Exp. 26629

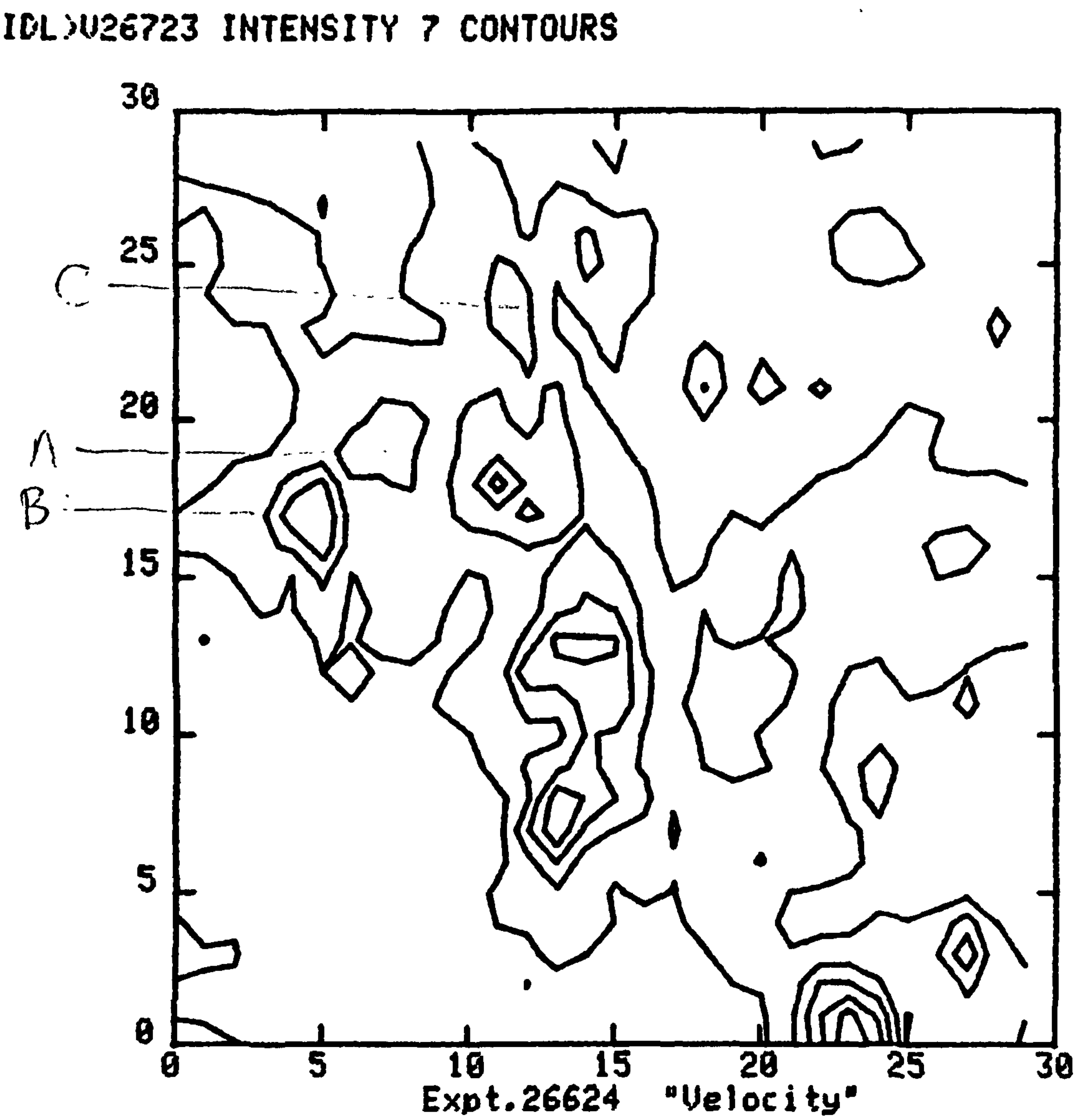

Fig. 28 Exp. 26723

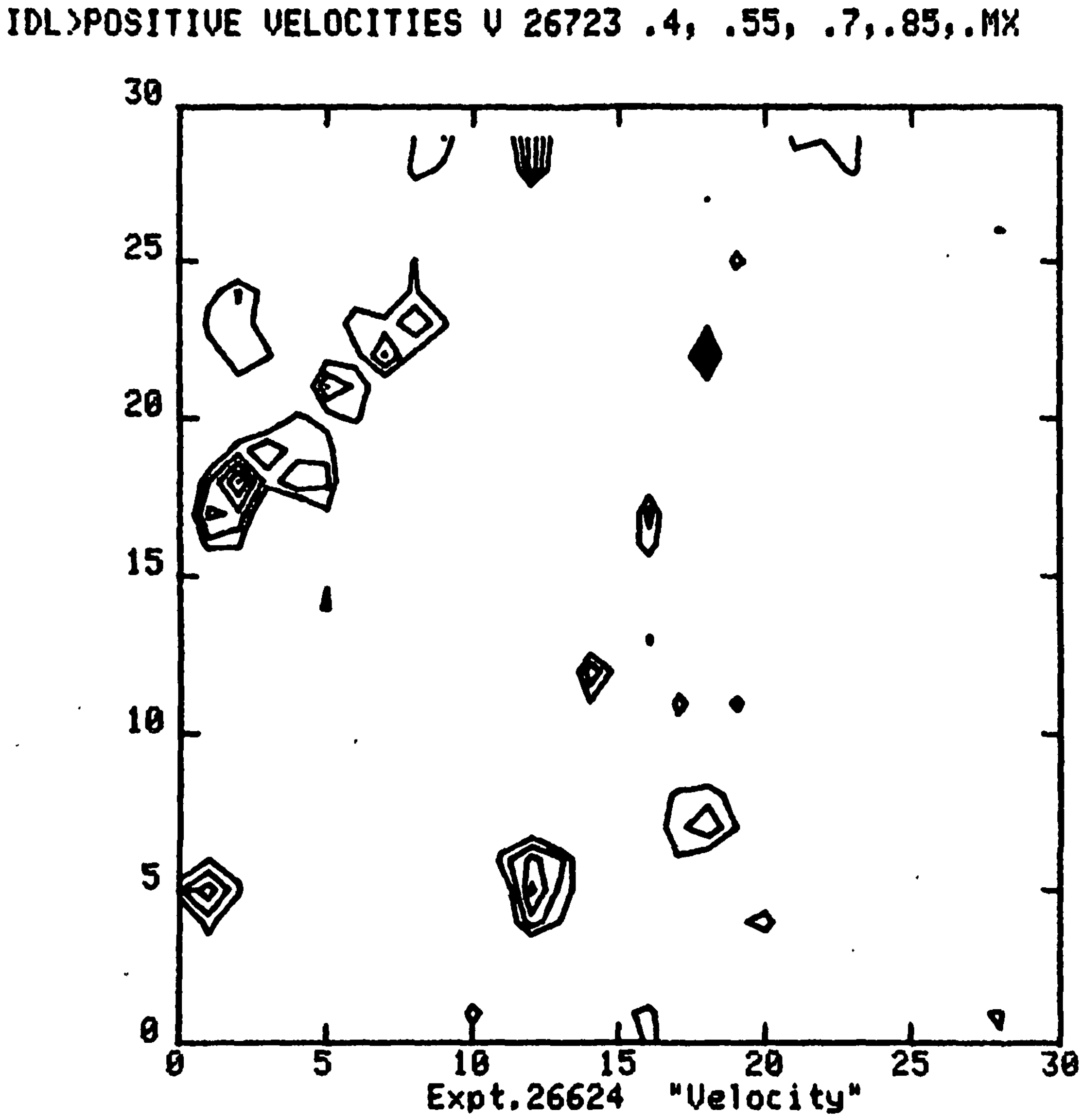

Fig. 29 Exp. 26723

IDL>NEGATIVE VELOCITIES V 26723 MN,.85,.7,,.55,.4 MN

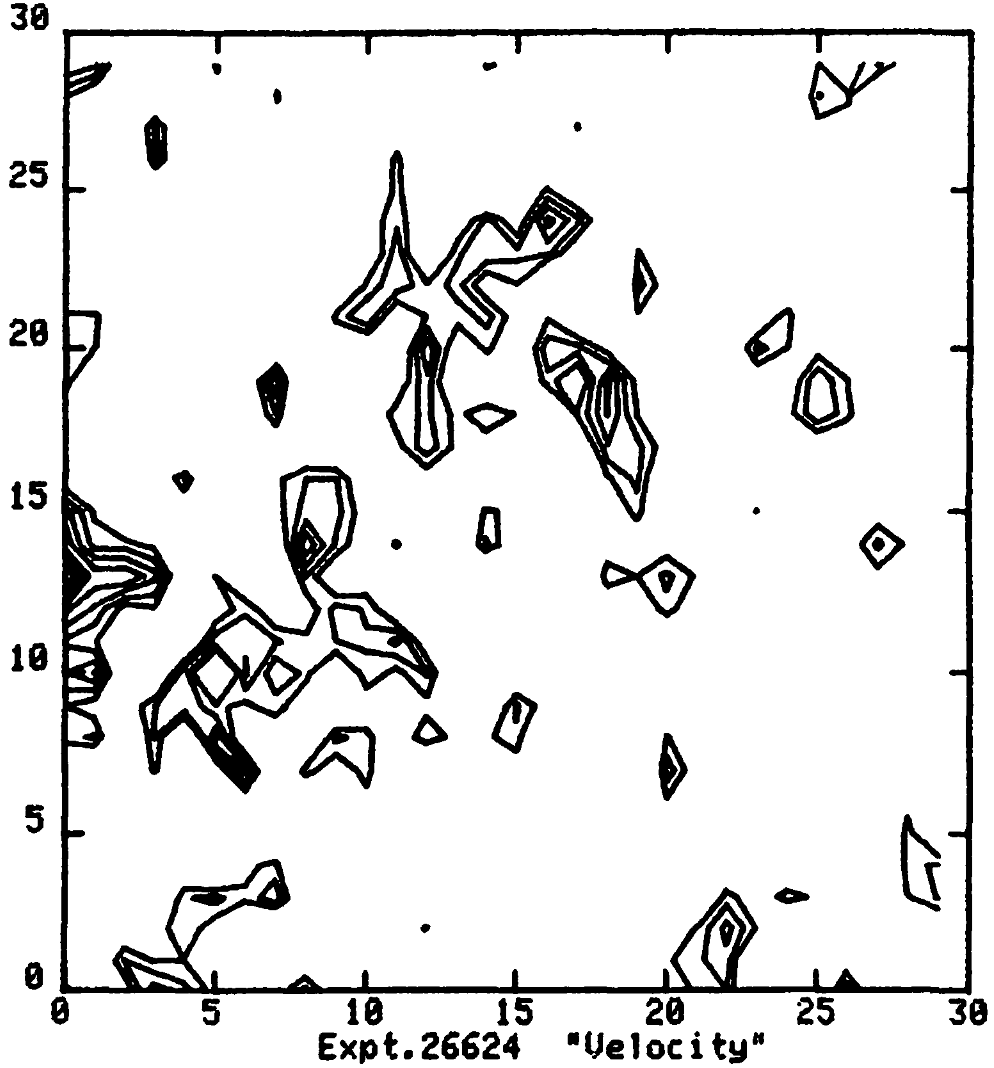

Fig. 30 Exp. 26723

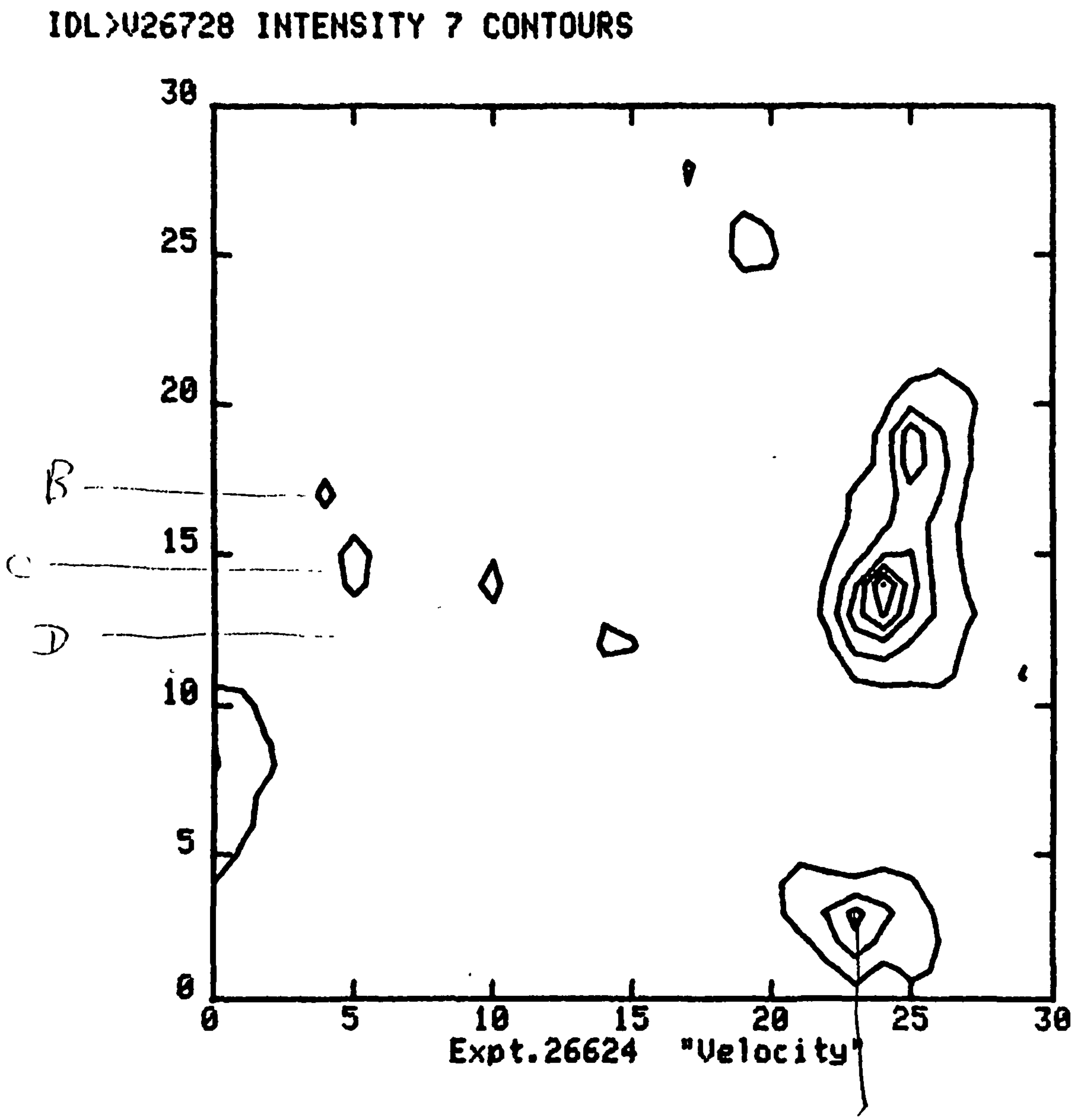

Fig. 31 Exp. 26728

IDL>POSITIVE VELOCITIES V 26728 .4 .55 .7 .85 MX

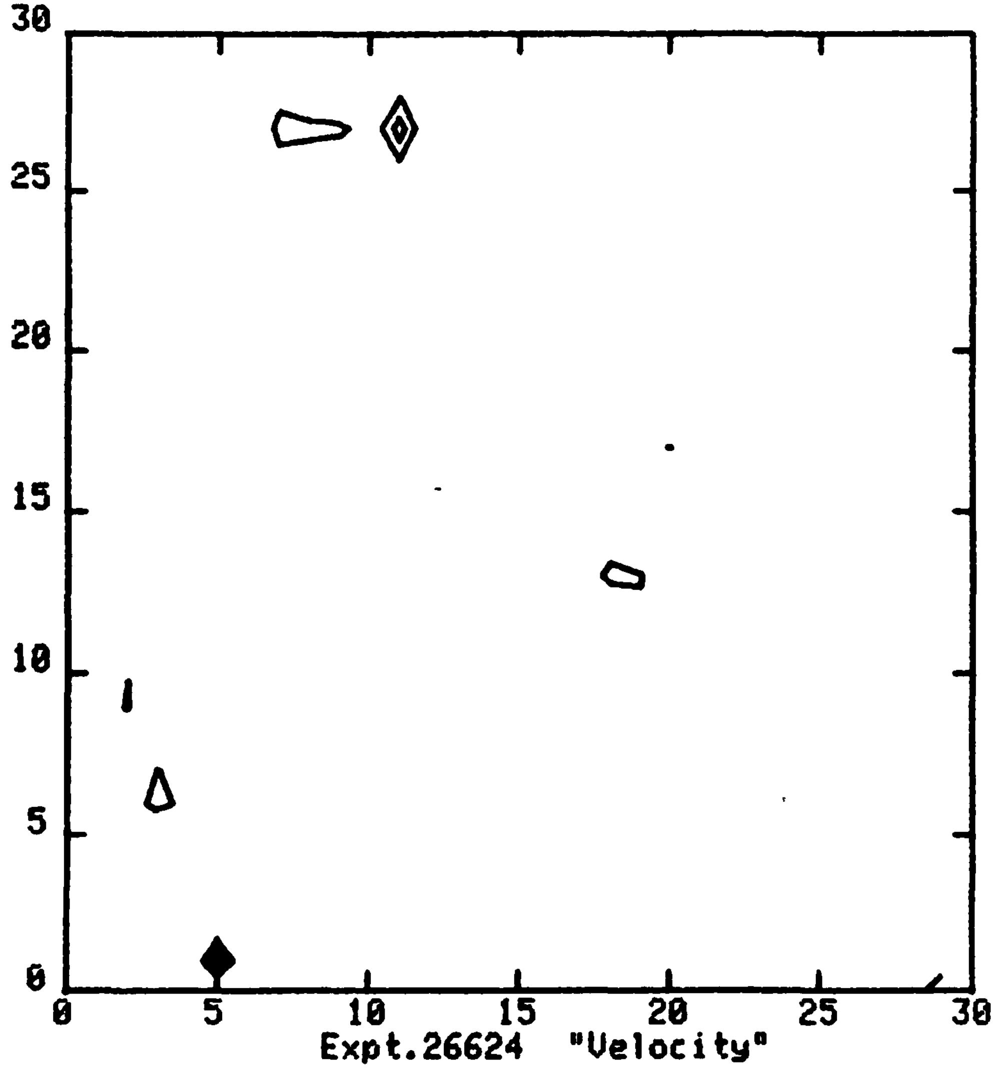

Fig. 32 Exp. 26728

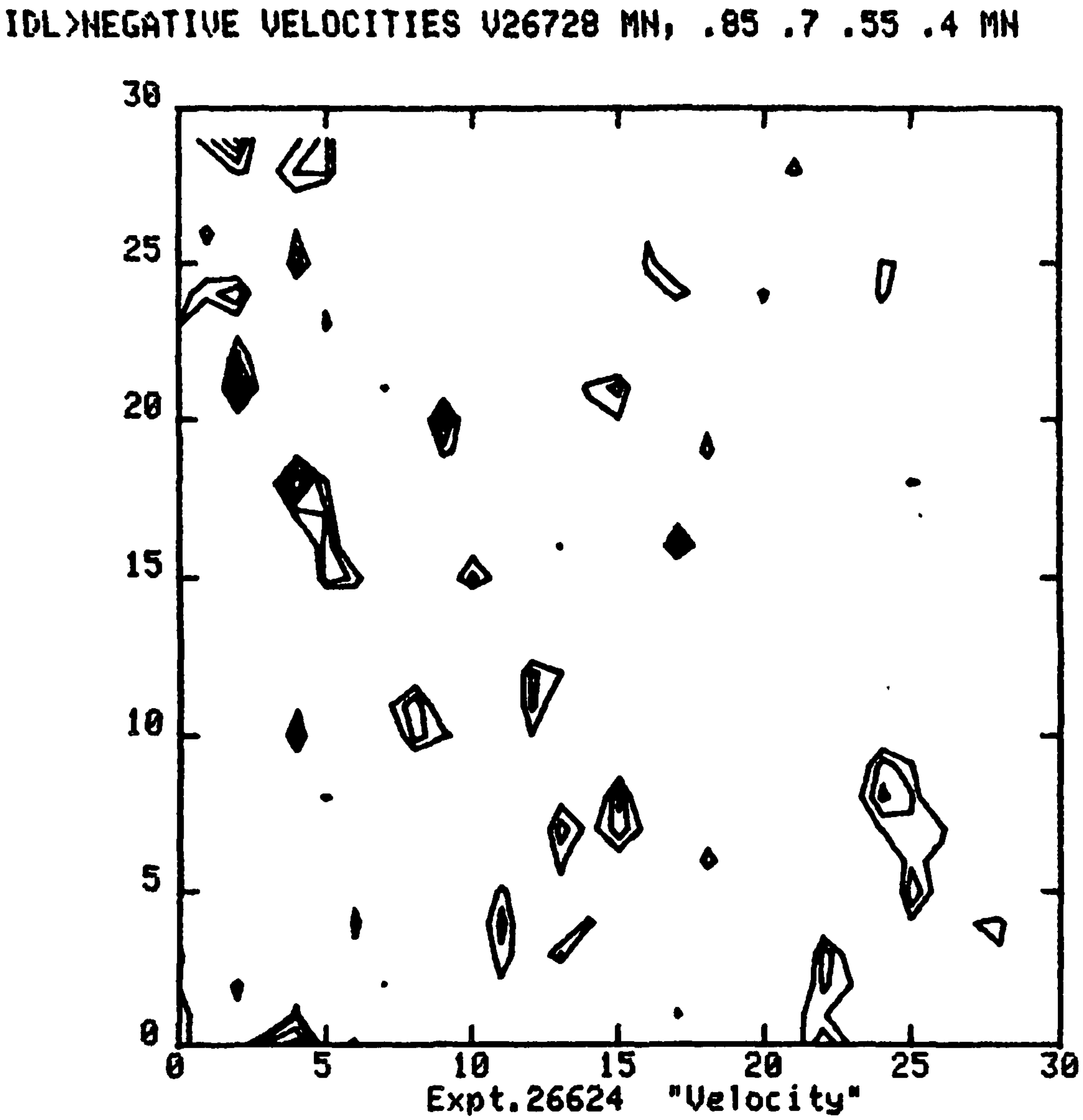

Fig. 33 Exp. 26728

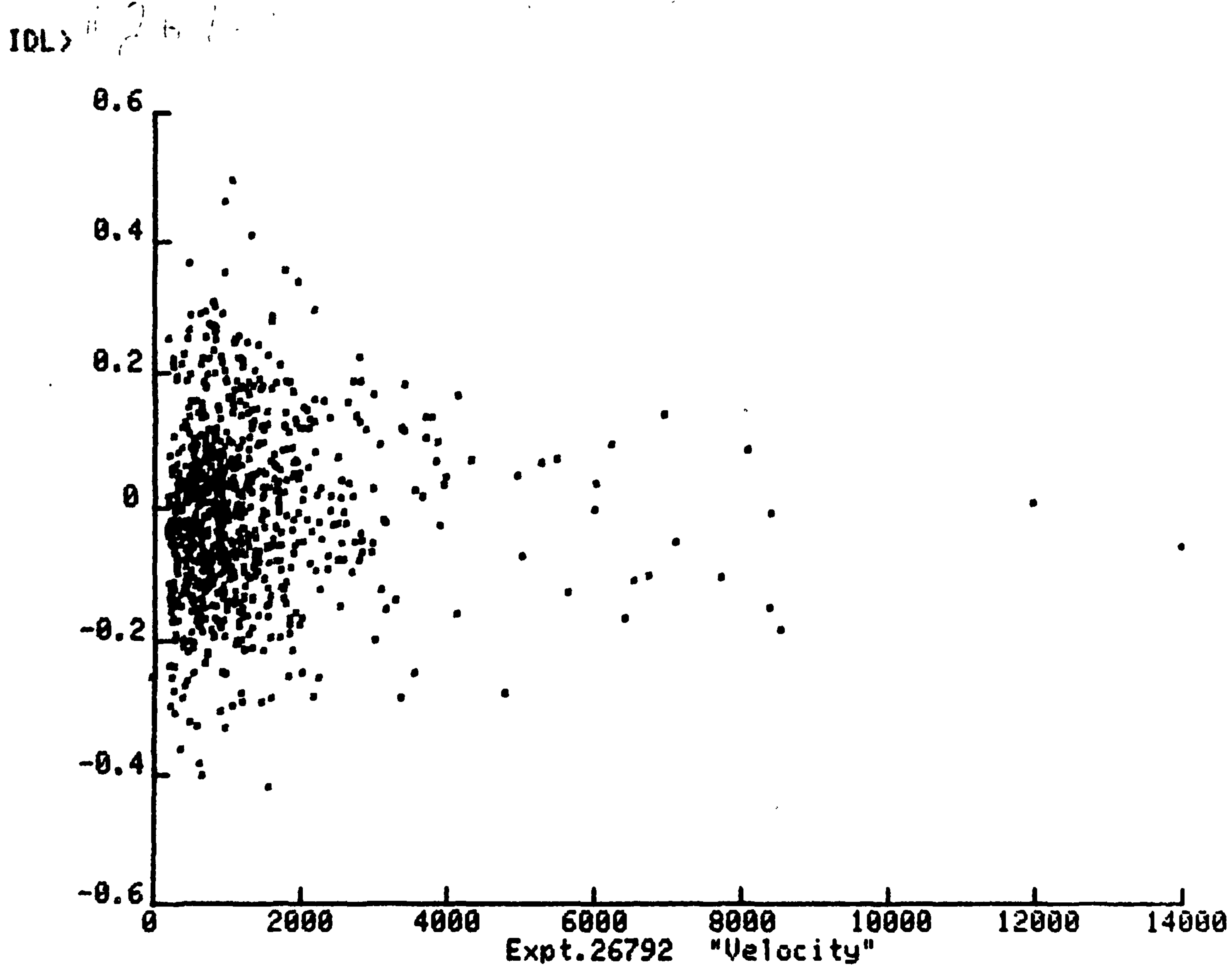

Fig. 34 Exp. 26728

IDL>INTENSITY V 26787 7 CONTOURS EQUALLY SPACED

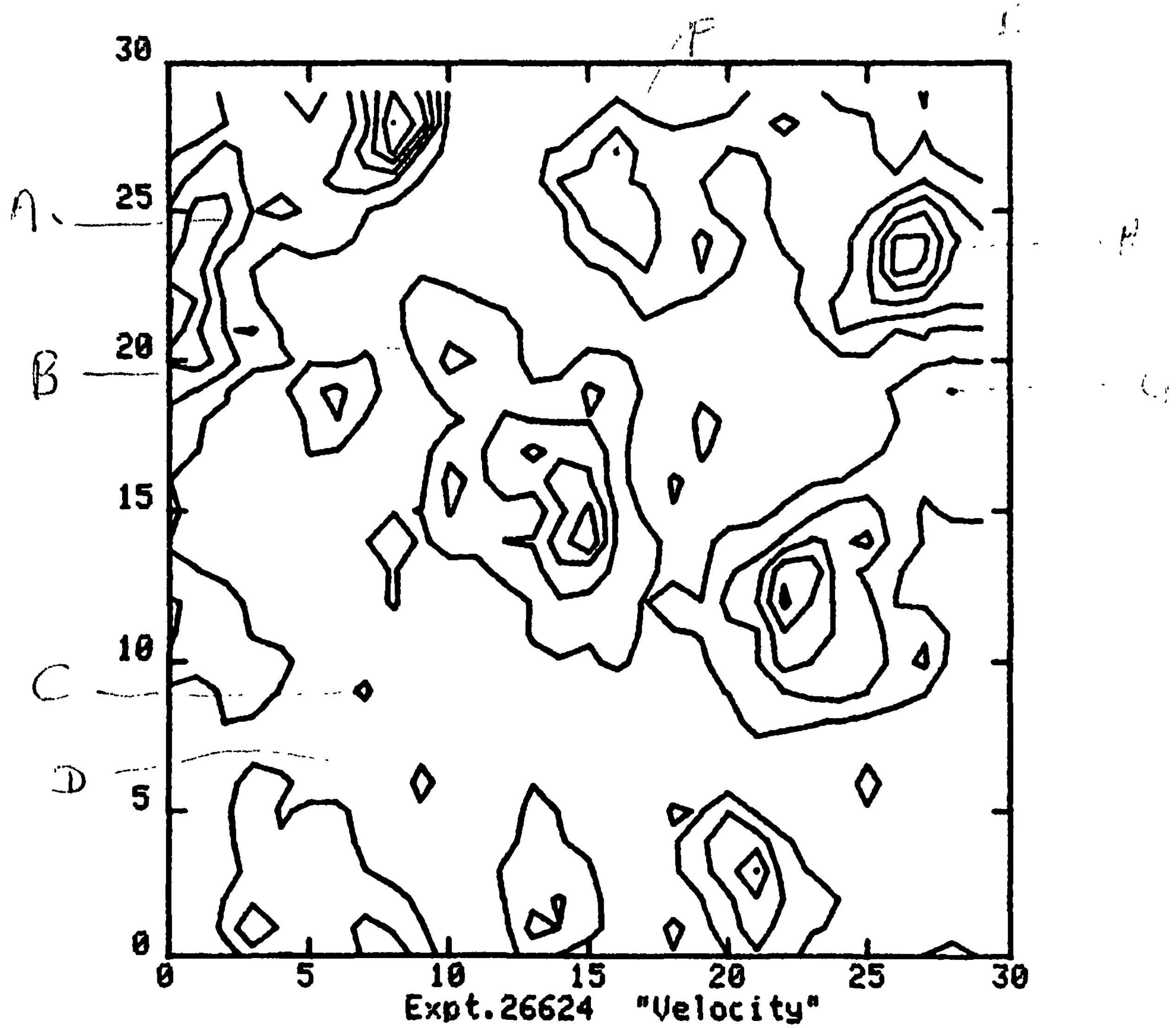

Fig. 35 Exp. 26787

IDL>POS VEL V 26787 .4, .55 .7 .85 MX

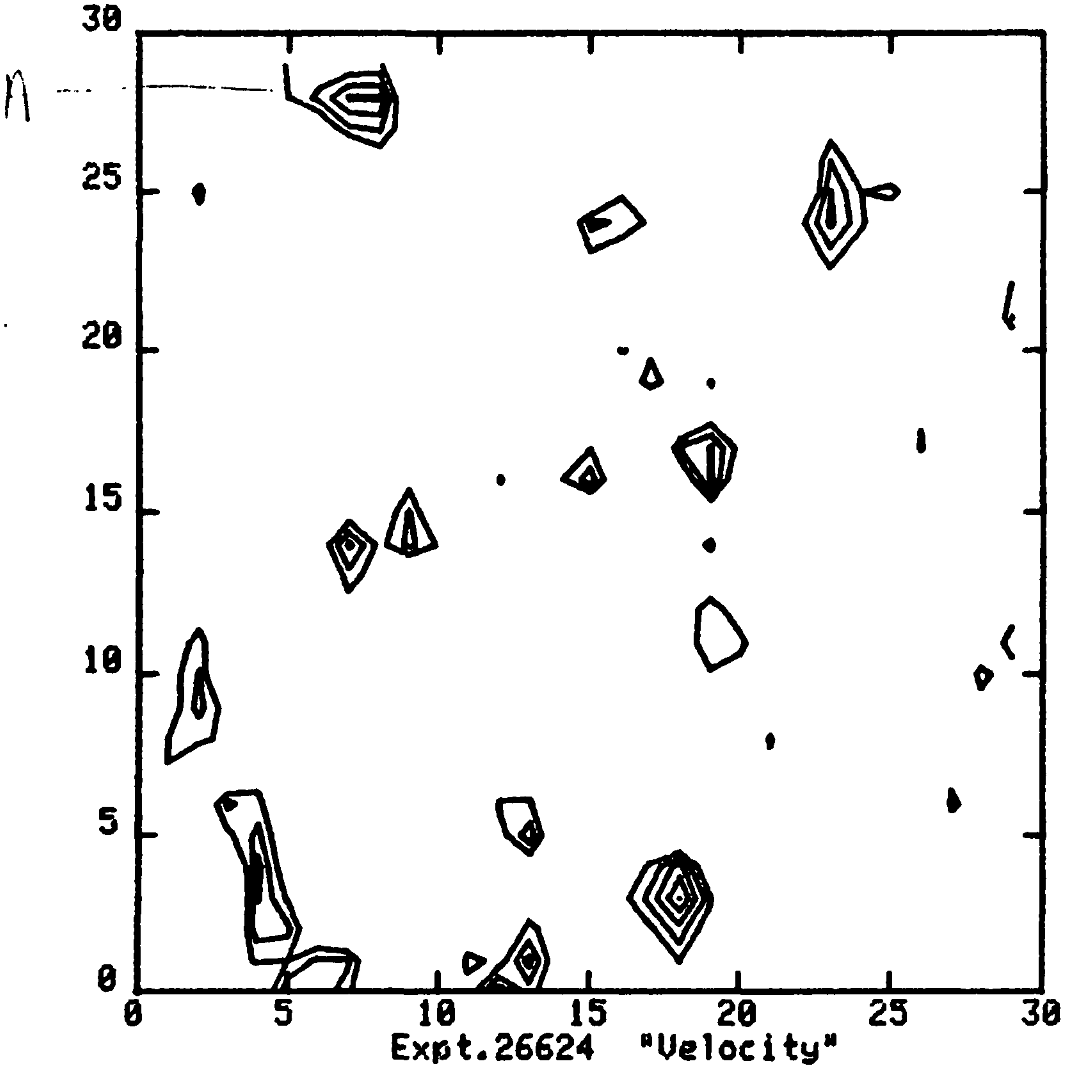

Fig. 36 Exp. 26787

IDL>NEG VEL V26787 MN .85 .7 .55 .4 MN

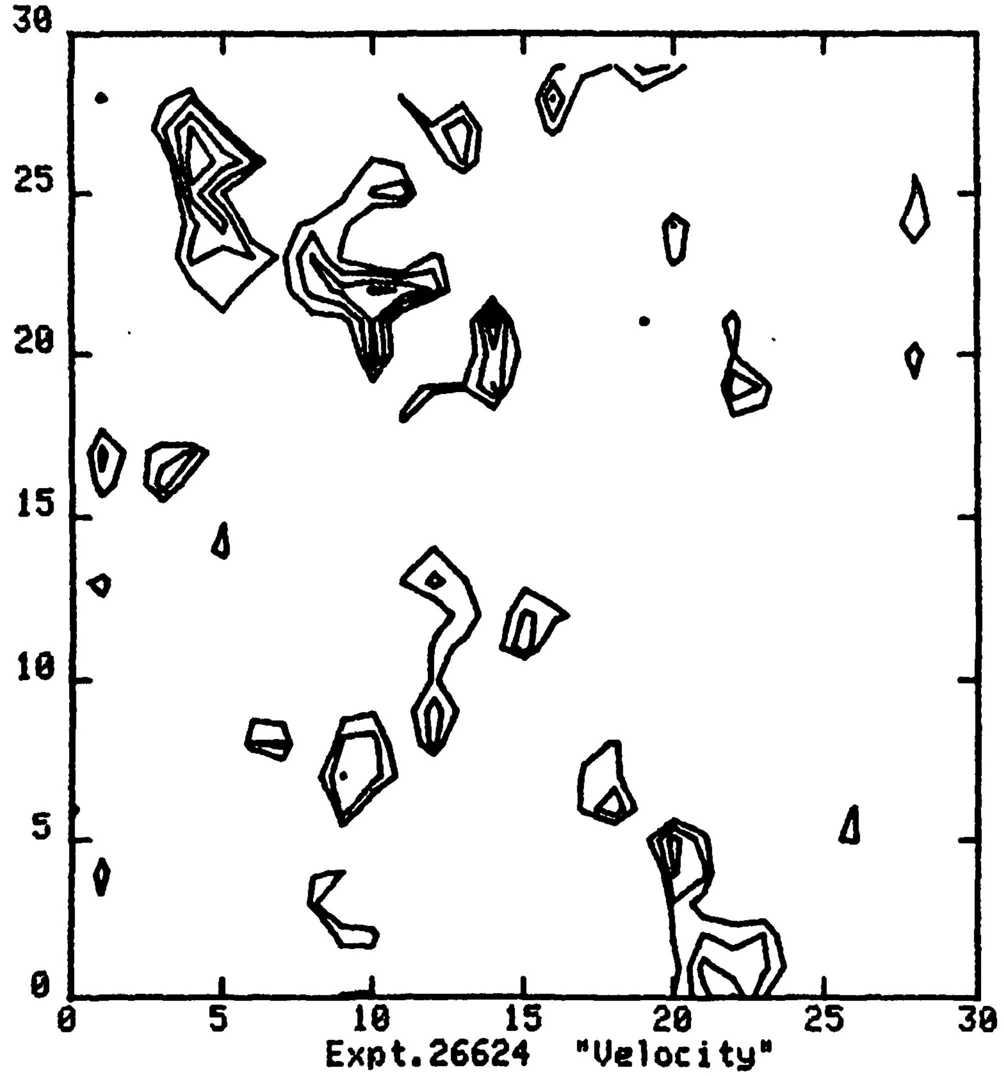

Fig. 37 Exp. 26787

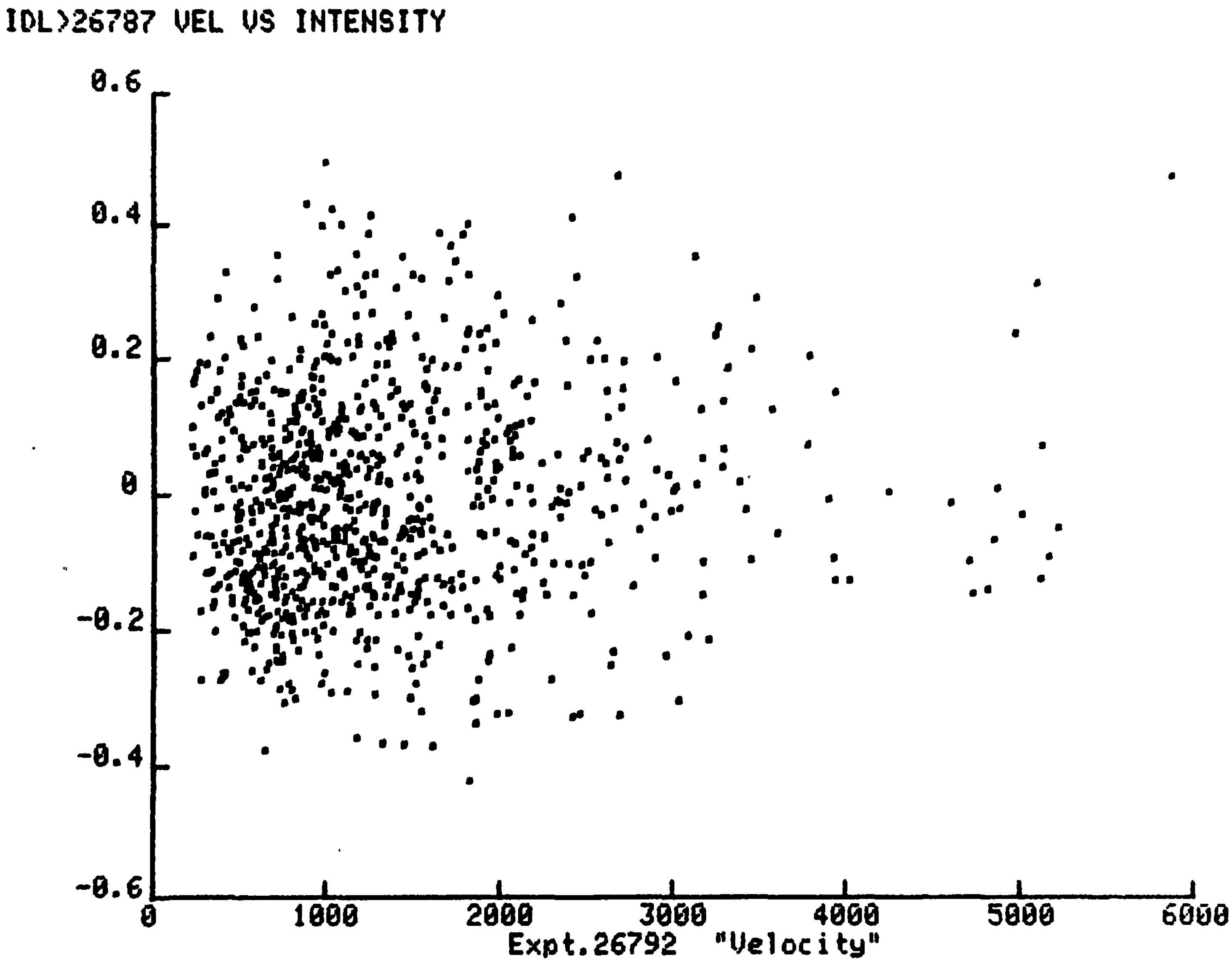

Fig. 38 Exp. 26787

IDL>INTENSITY V26792 7 EQUAL CONTOURS

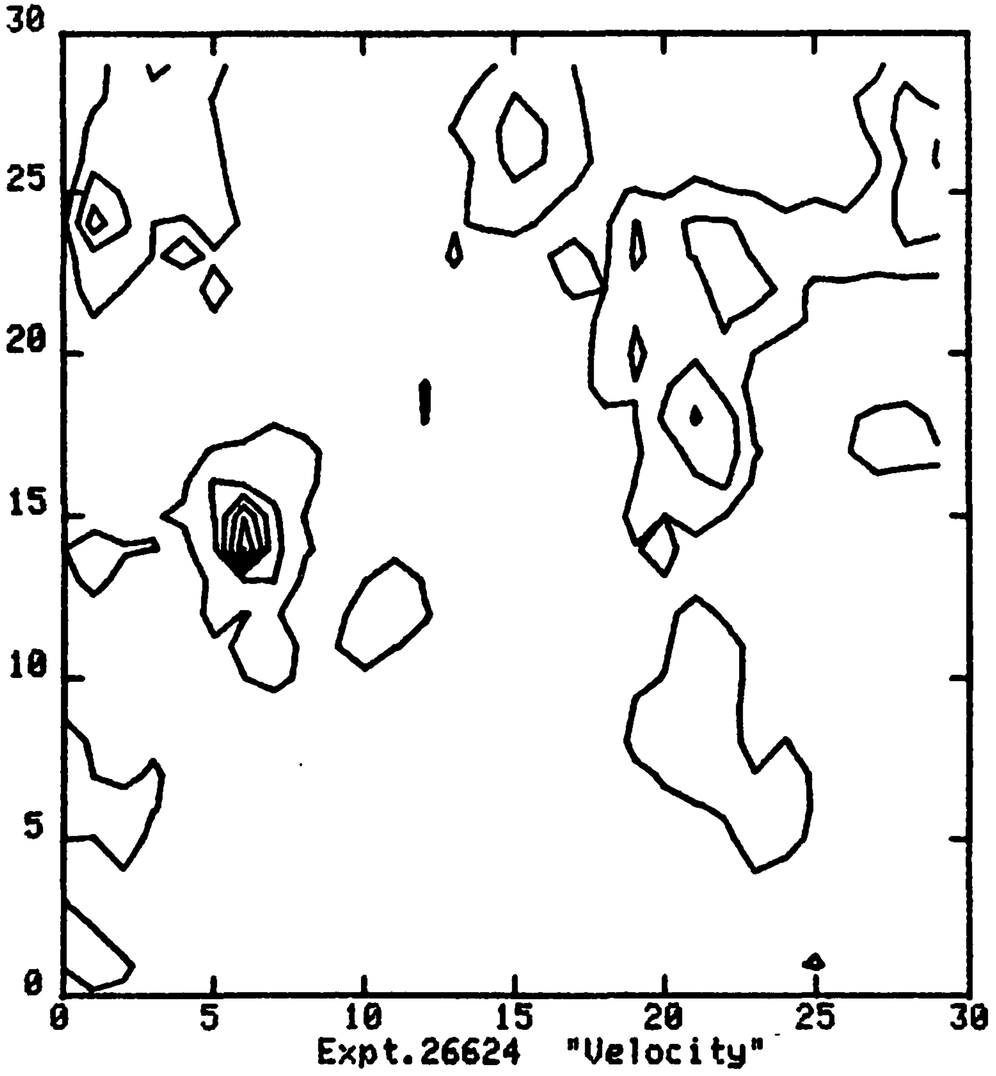

Fig. 39 Exp. 26792

IDL>POS VEL V26792

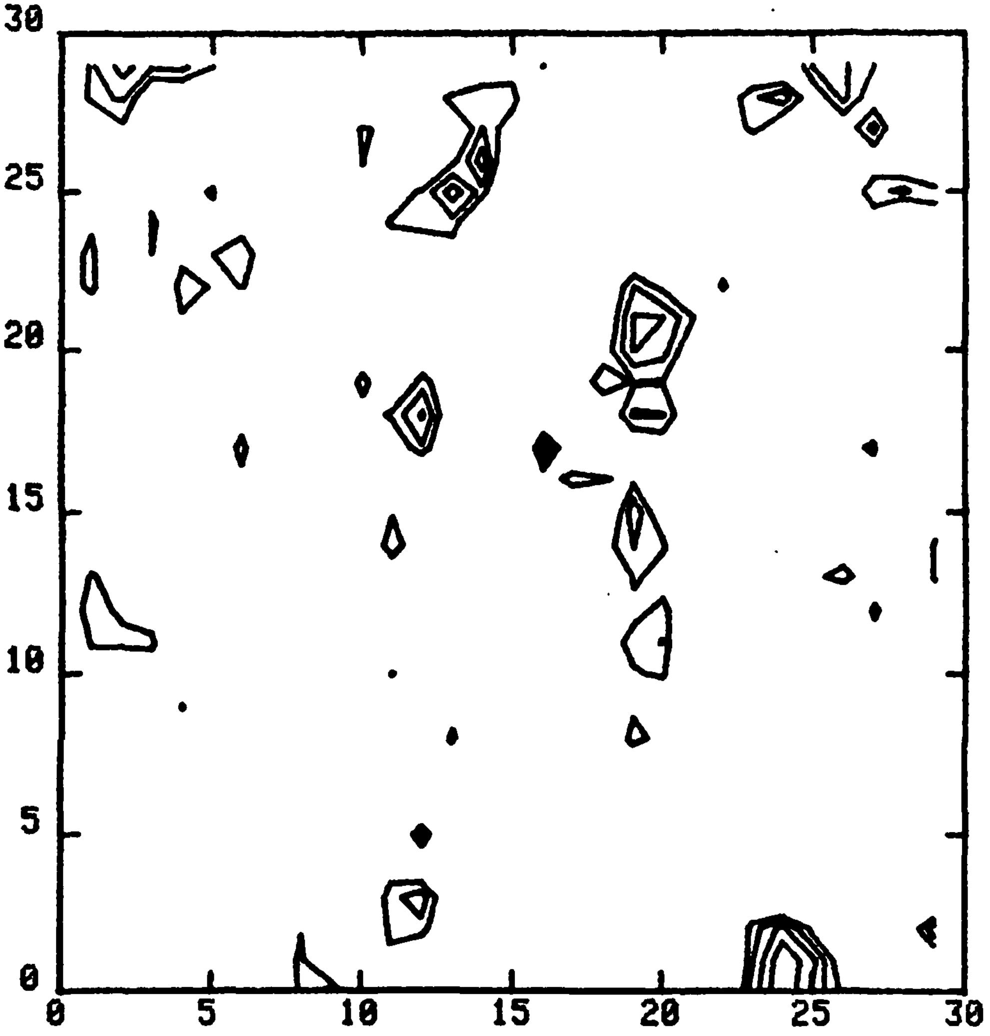

Fig. 40 Exp. 26792

IDL>NEG VEL V 26792 MN, .85.7 .55 .4 MN

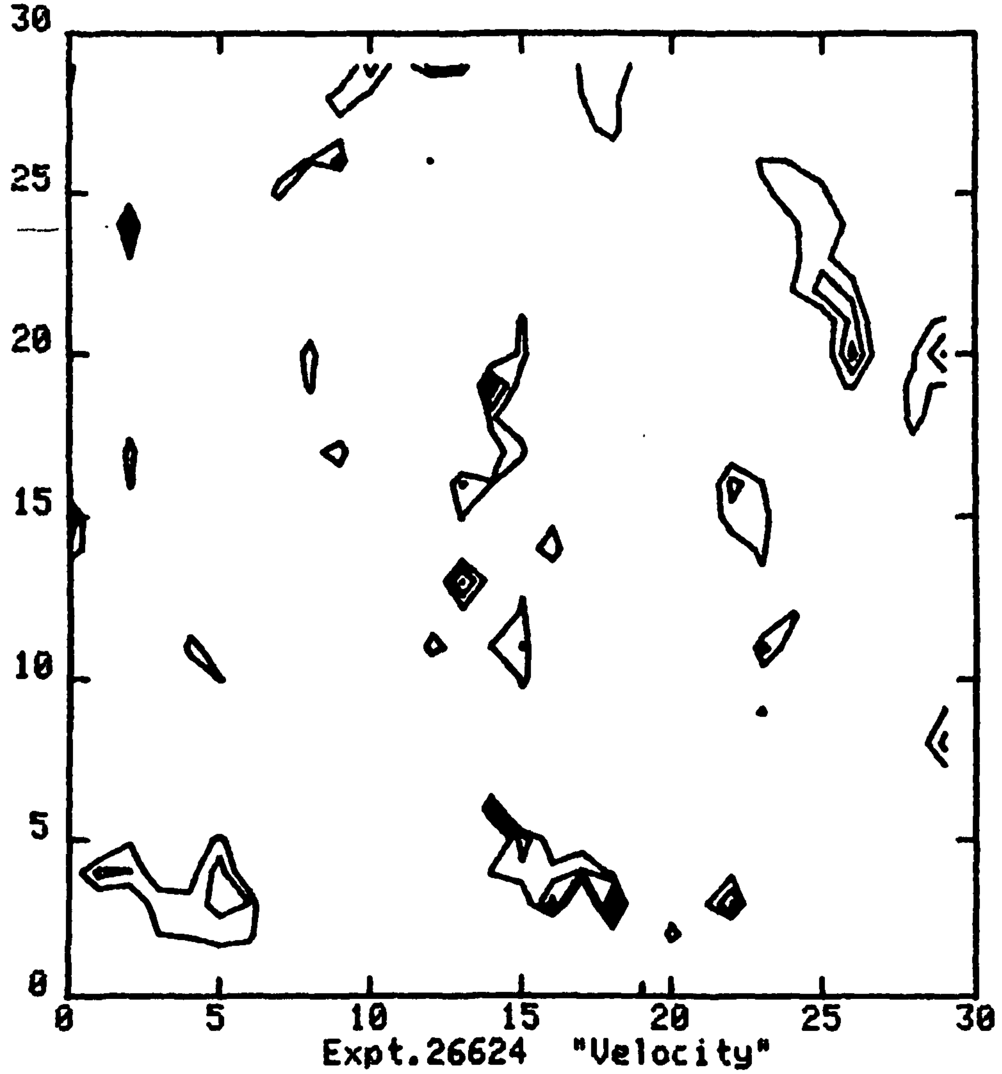

Fig. 41 Exp. 26792

ORIGINAL PAGE IS
OF POOR QUALITY

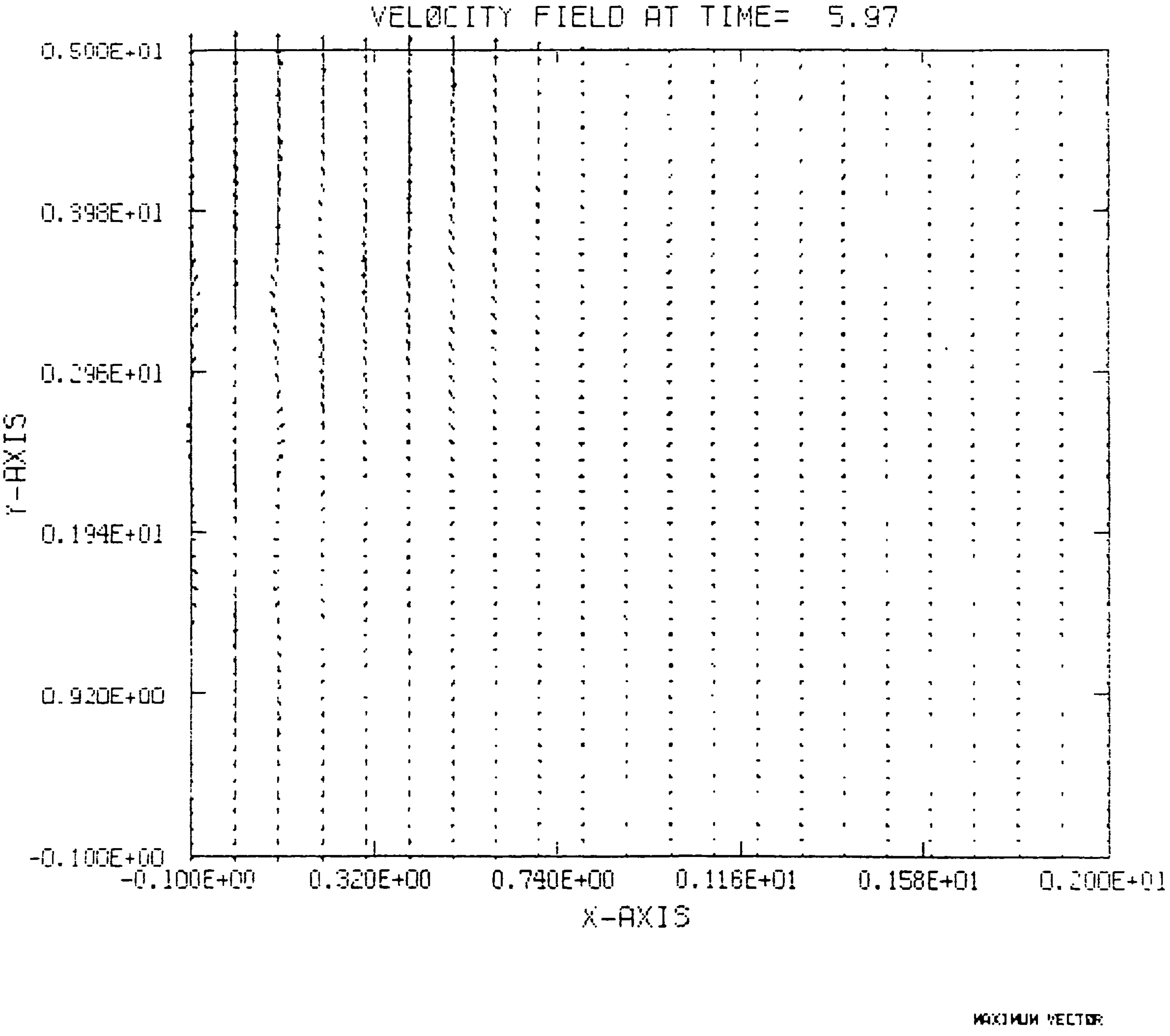

FIG. 42

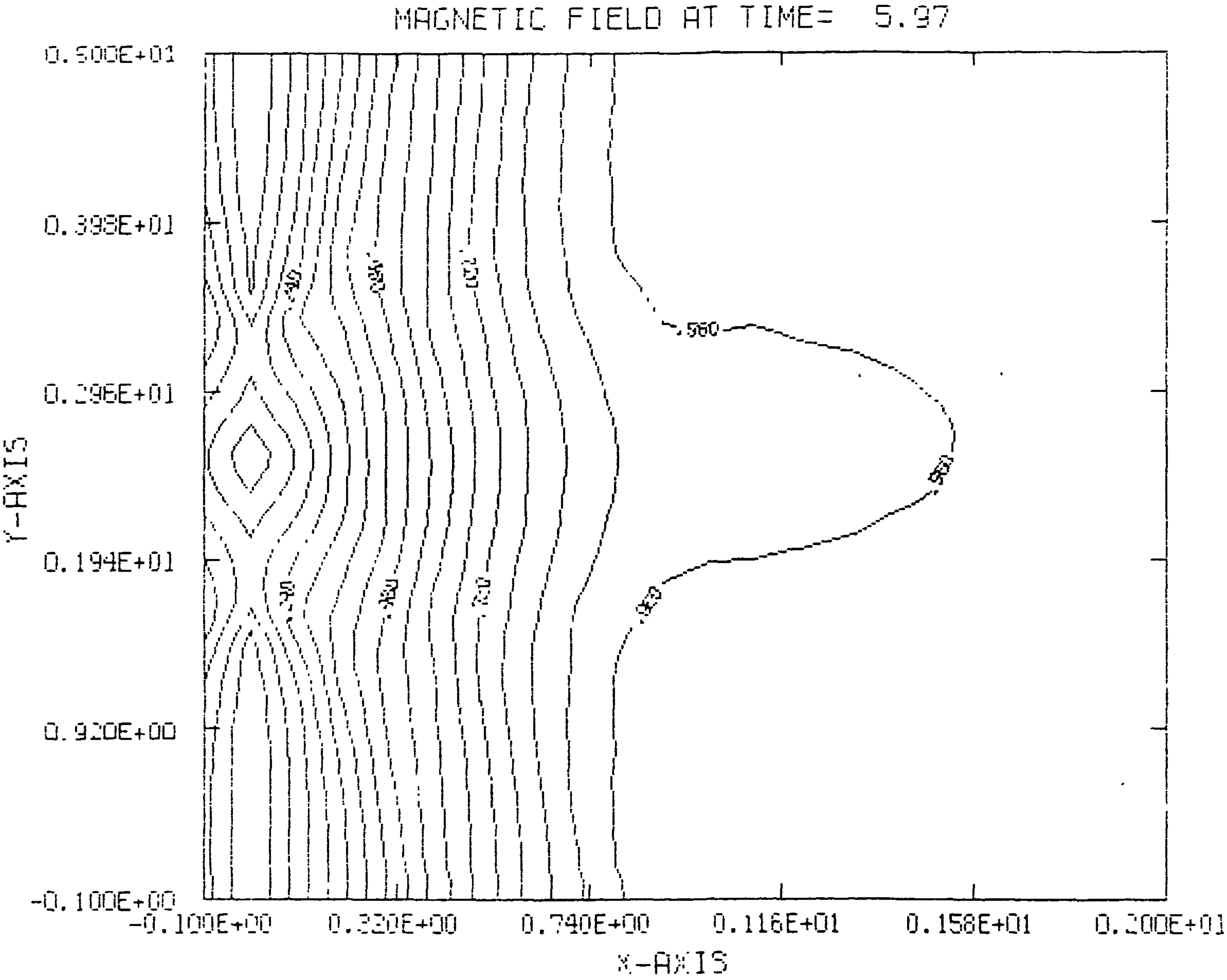

CONTOUR FROM 0.00000E+00 TO 0.96000 CONTOUR INTERVAL OF 0.80000E-01 PT(9,3)= 0.14038

FIG. 43

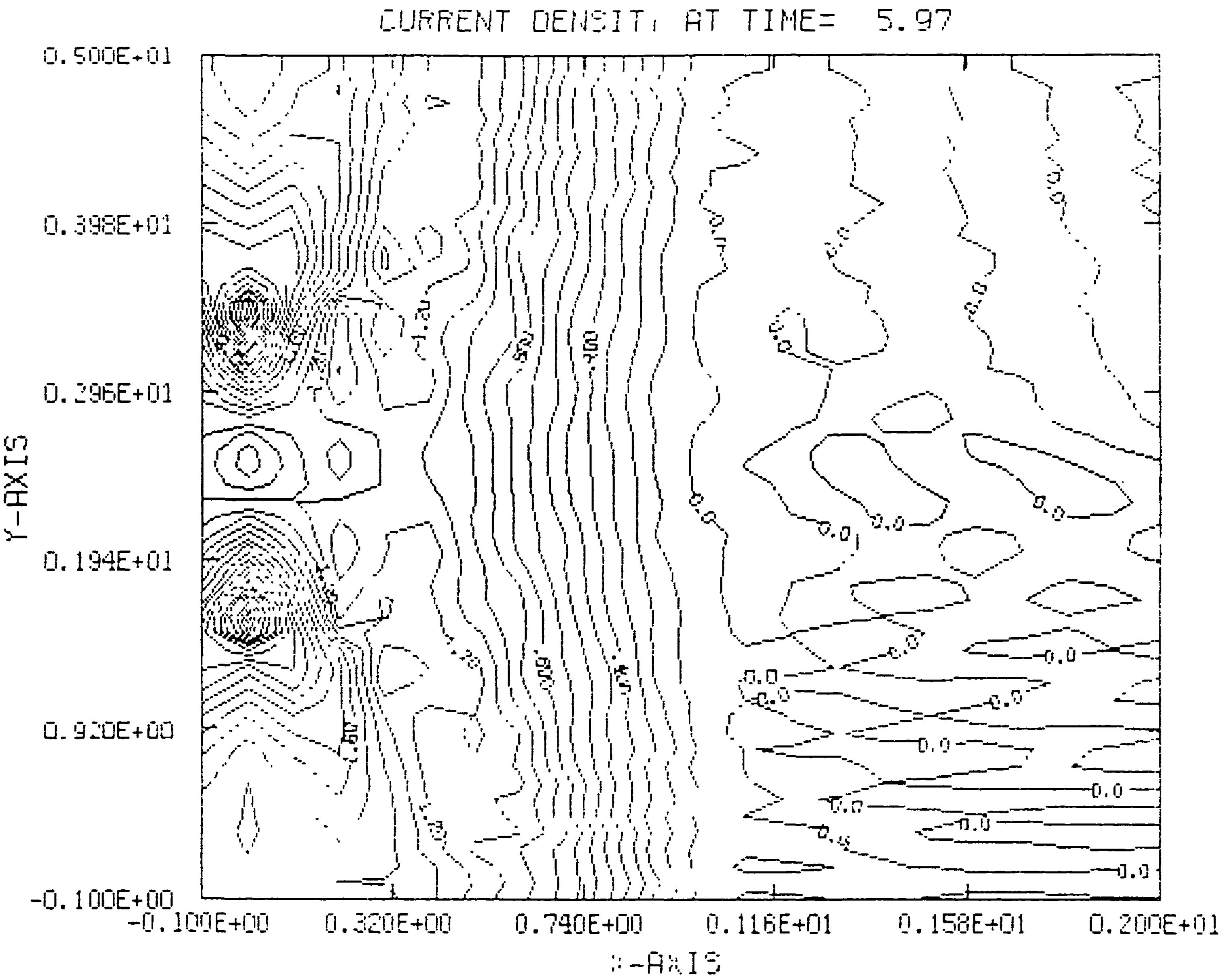

CONTOUR FROM 0.0000E+00 TO 3.0000 CONTOUR INTERVAL OF 0.10000 PT(3,3)= 1.9057

FIG. 44

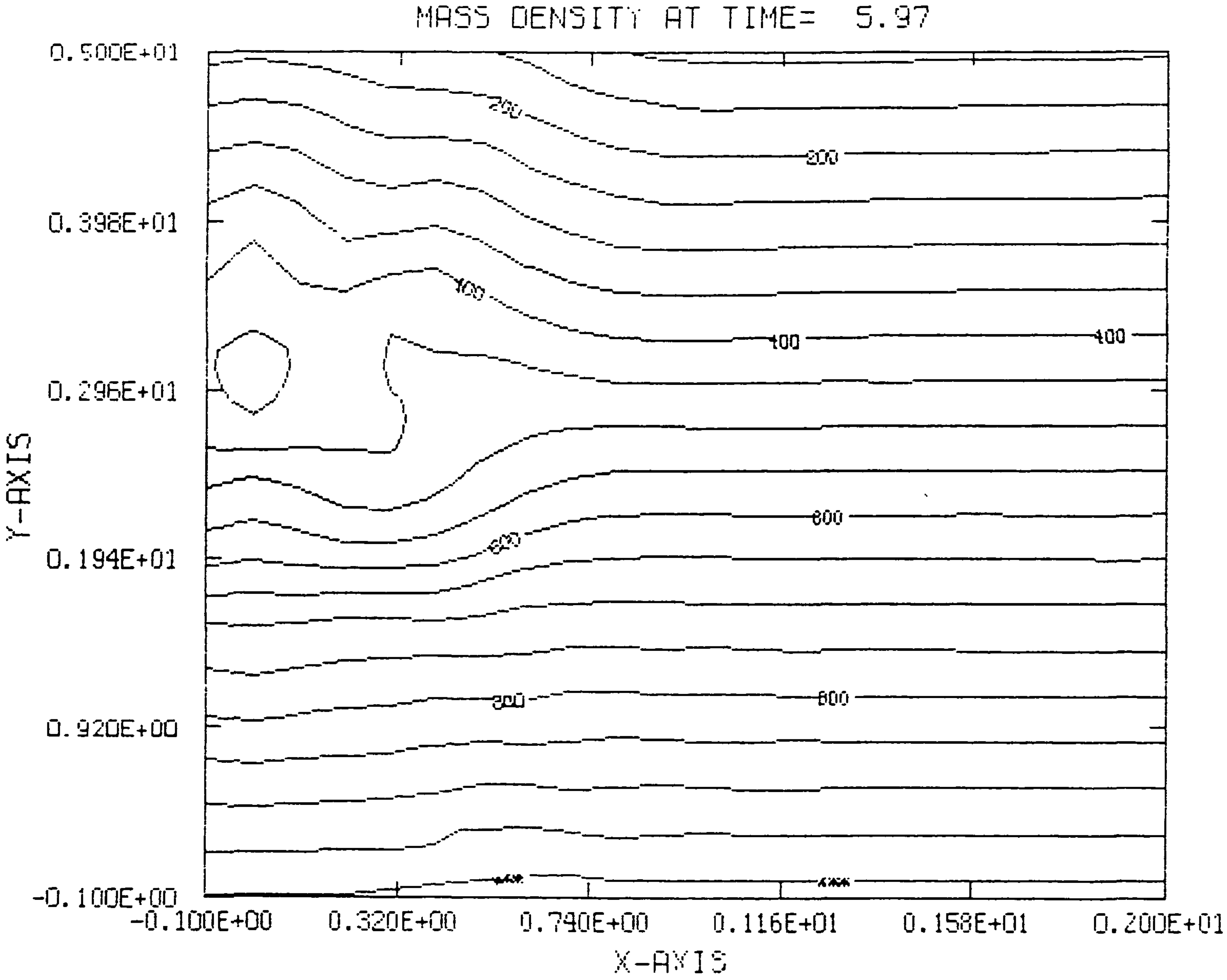

CONTOUR FROM 0.50000E-01 TO 1.0000 CONTOUR INTERVAL OF 0.50000E-01 PT(3,3)= 0.97976 LABELS SCALED BY 1000.0

FIG. 45

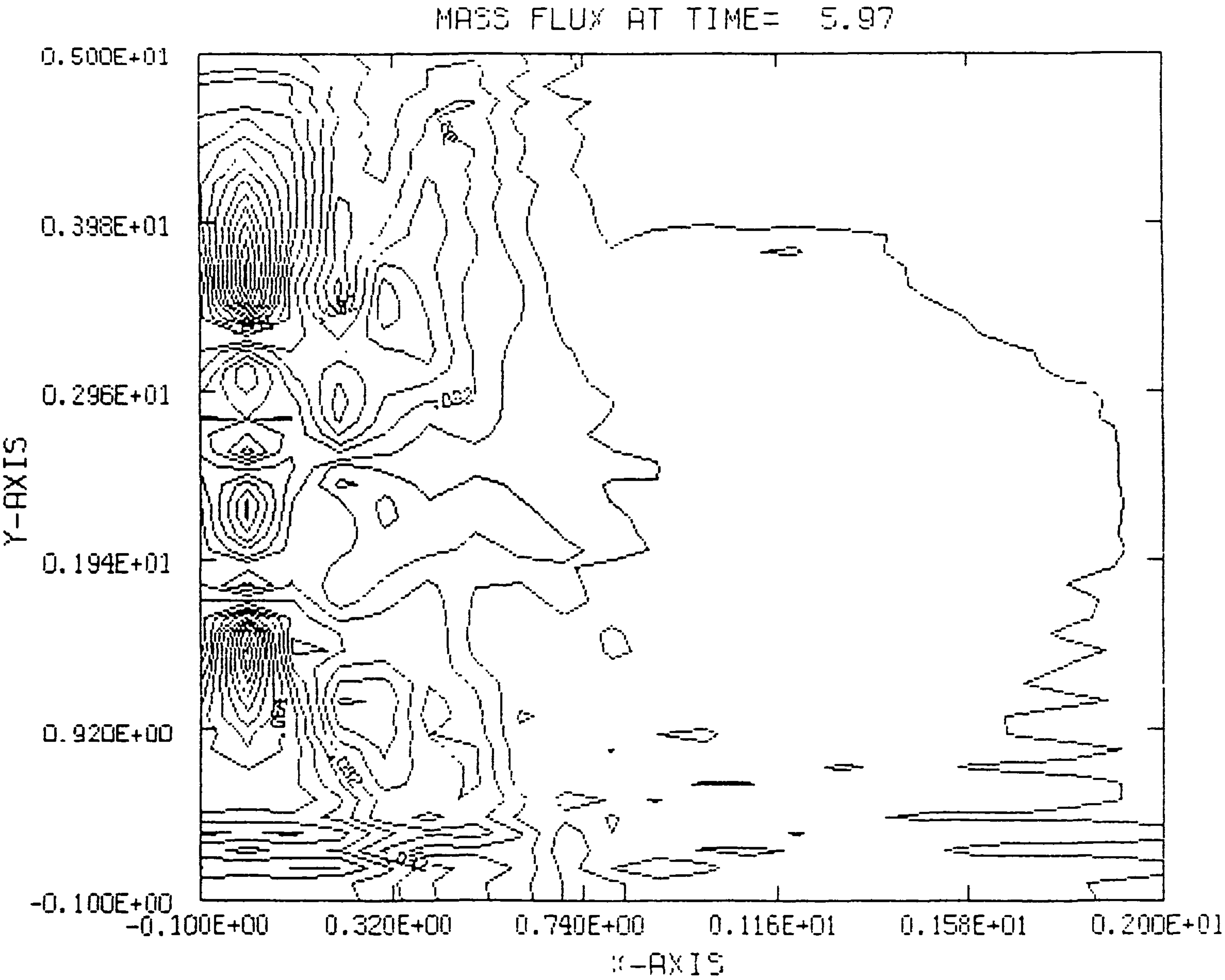

CONTOUR FROM 0.00000E+00 TO 0.13600 CONTOUR INTERVAL OF 0.80000E-02 PT(3,3)= 0.84159E-01

FIG. 46

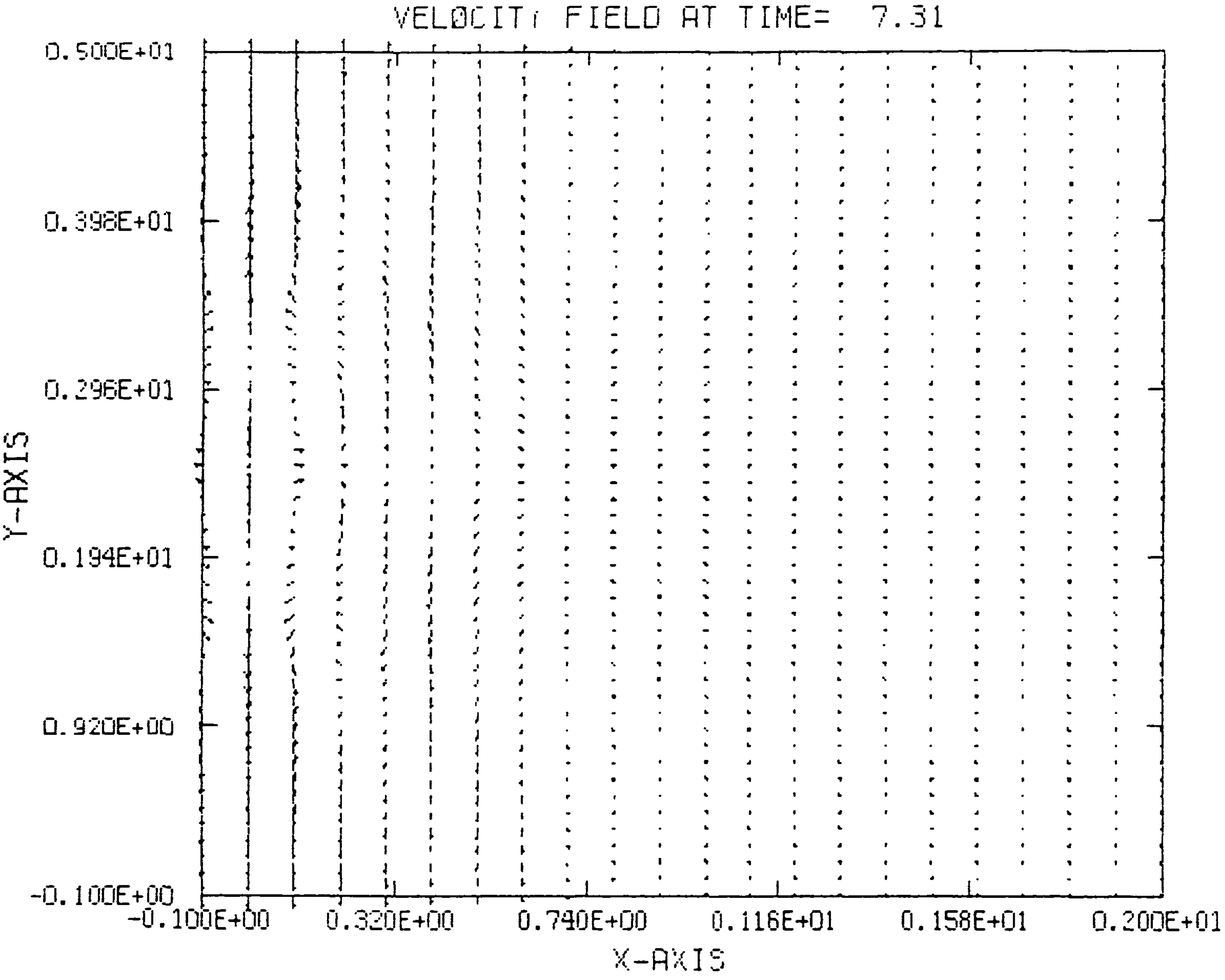
VELØCITY FIELD AT TIME= 7.31
0.500E+01
0.398E+01
0.296E+01
0.194E+01
0.920E+00
-0.100E+00
Y-AXIS
-0.100E+00
0.320E+00
0.740E+00
0.116E+01
0.158E+01
0.200E+01
X-AXIS

FIG. 47

0.183E+00
MAXIMUM VECTOR

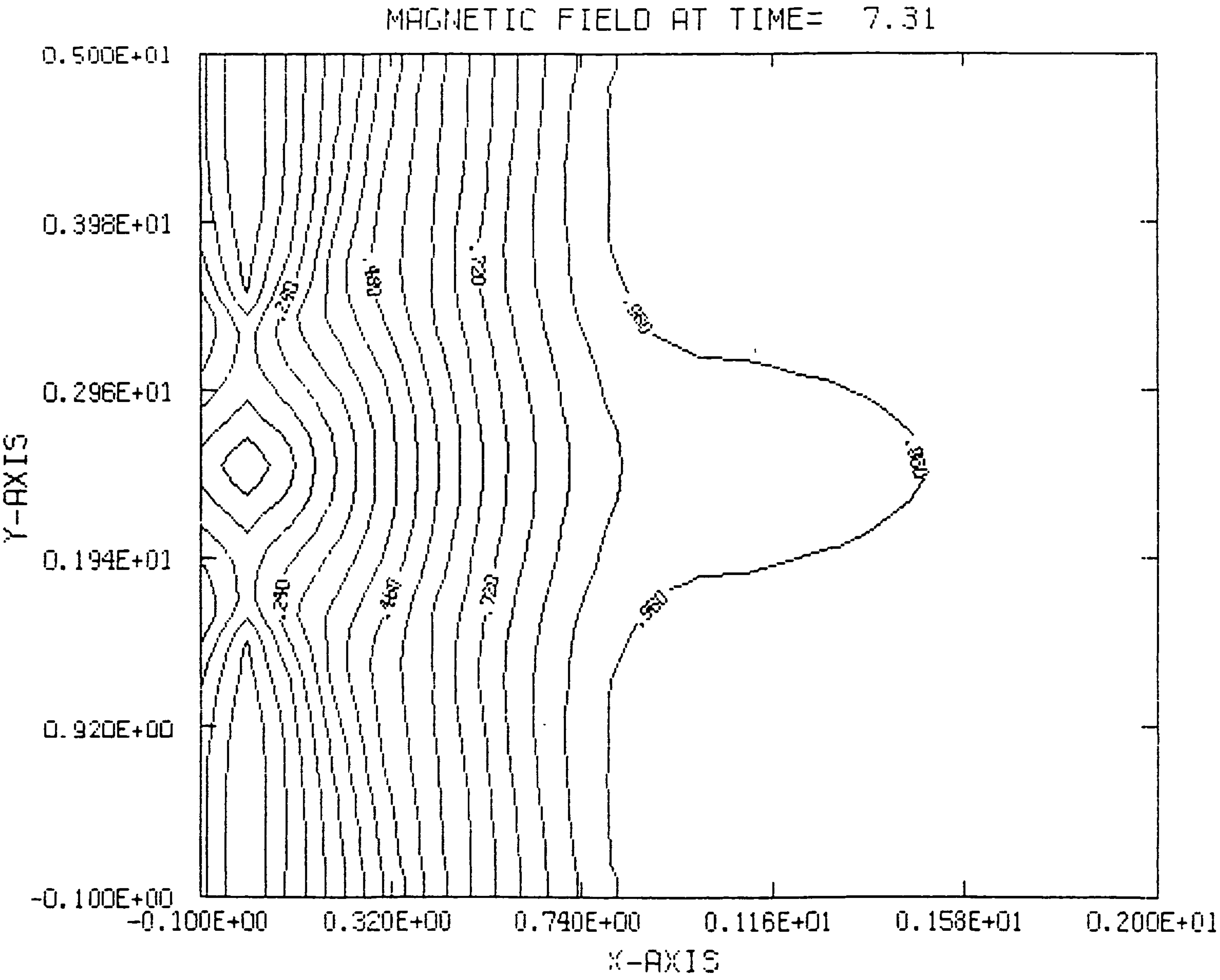

```
CONTOUR FROM  0.00000E+00 TO  0.98000     CONTOUR INTERVAL OF  0.80000E-01 PT(3,3)=  0.13545
```

FIG. 48

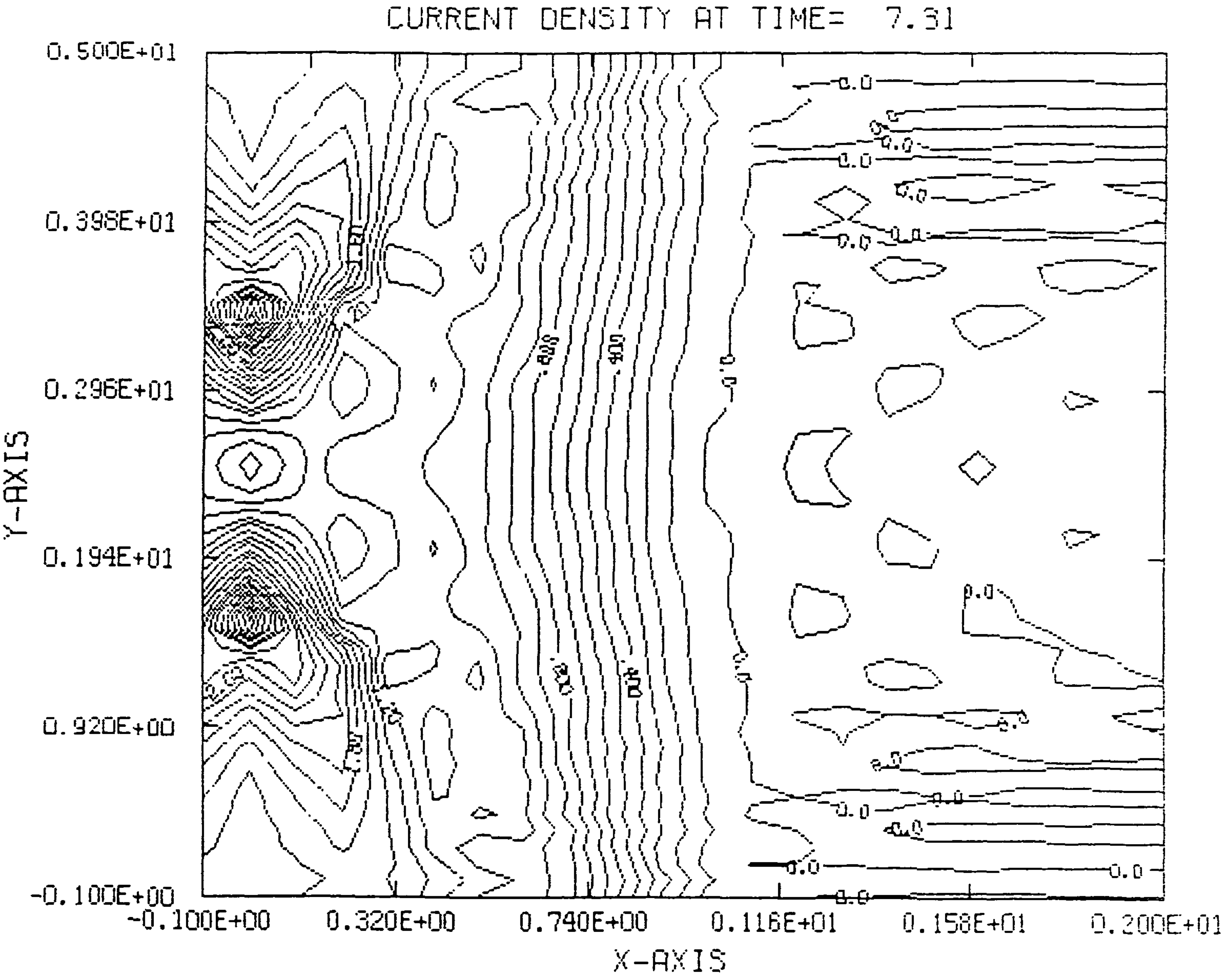

CONTOUR FROM 0.00000E+00 TO 2.9000 CONTOUR INTERVAL OF 0.10000 PT(9,3)= 1.3979

FIG. 49

ORIGINAL PAGE IS
OF POOR QUALITY

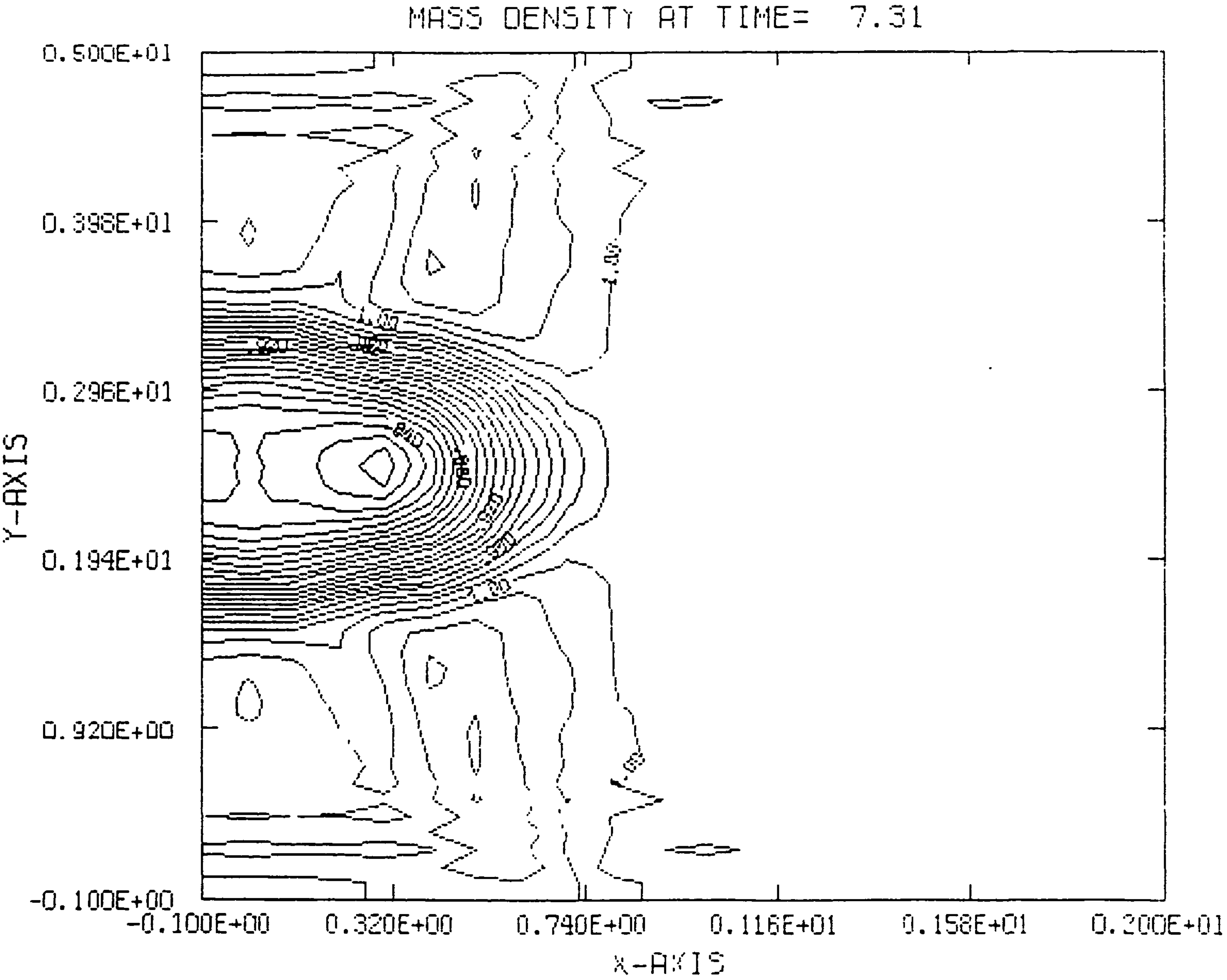

CONTOUR FROM 0.80000 TO 1.0300 CONTOUR INTERVAL OF 0.10000E-01 PT(3,3)= 1.0170

FIG. 50

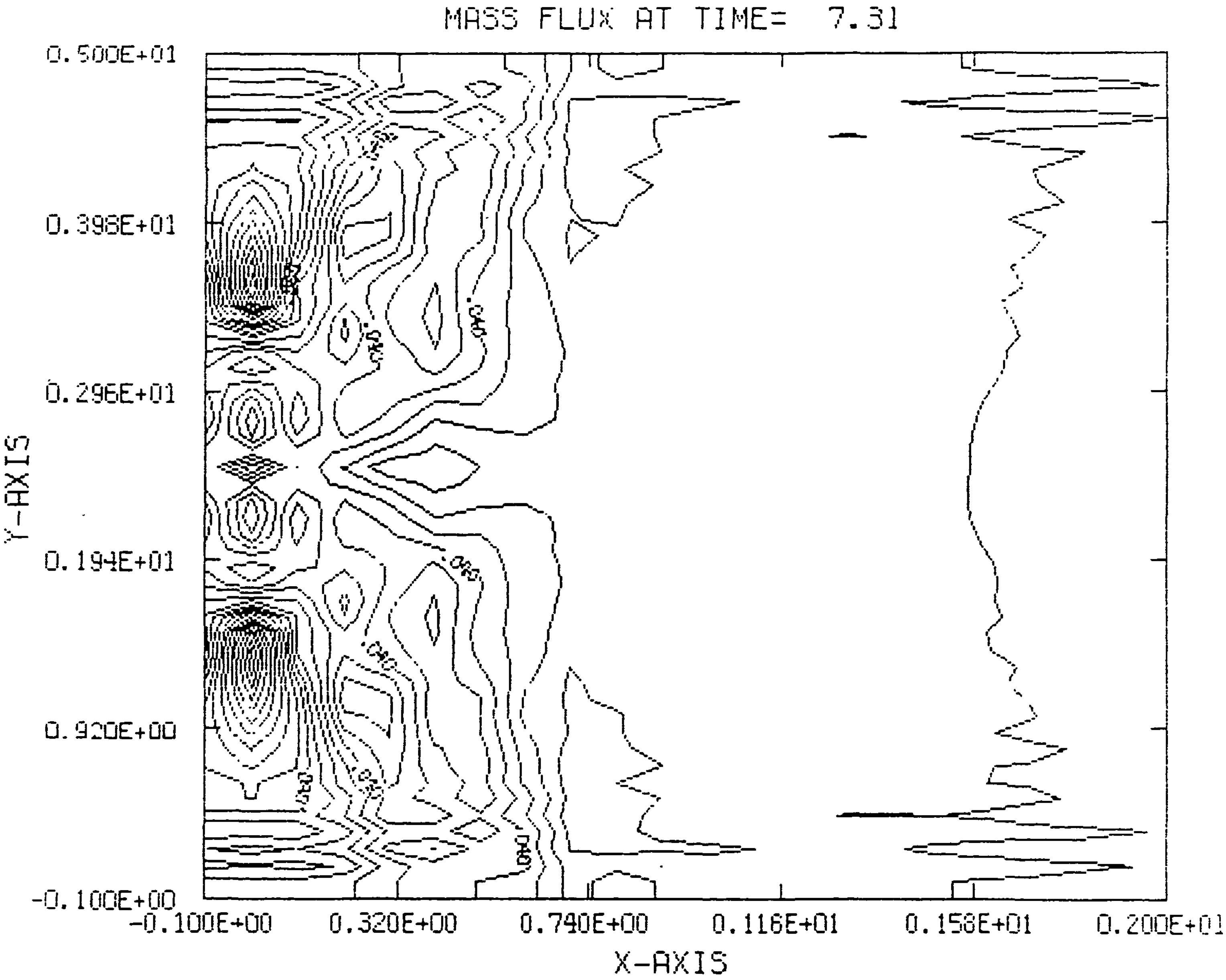

CONTOUR FROM 0.00000E+00 TO 0.18000 CONTOUR INTERVAL OF 0.10000E-01 PT(3,3)= 0.84034E-01

FIG. 51

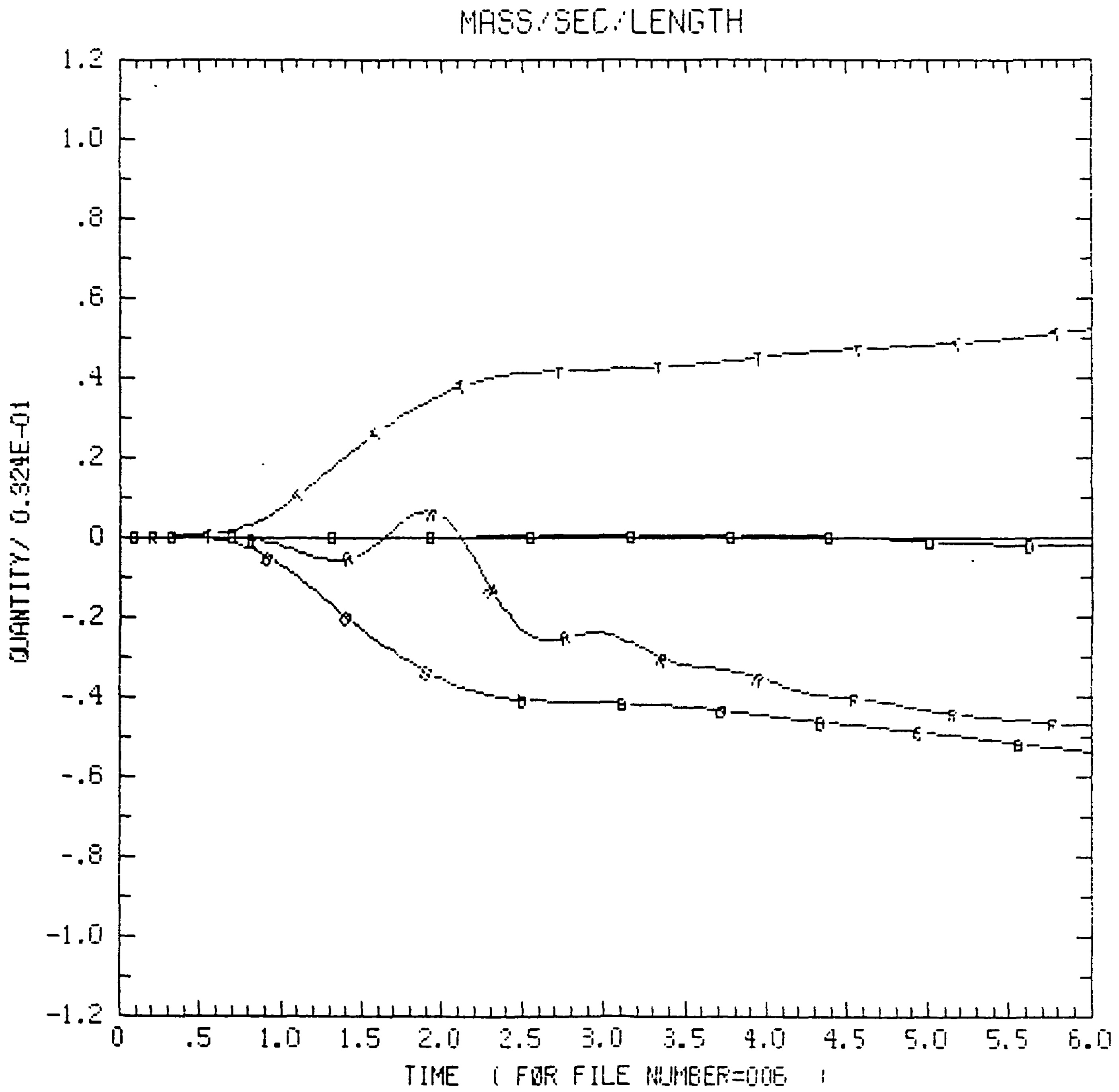

FIG. 52

52 \32

T = [illegible] -ve

comes in from right -ve

R = flow from right   B = flow out bottom   out = -ve

D = diff [illegible] Top-Bottom

DOt: no [illegible]

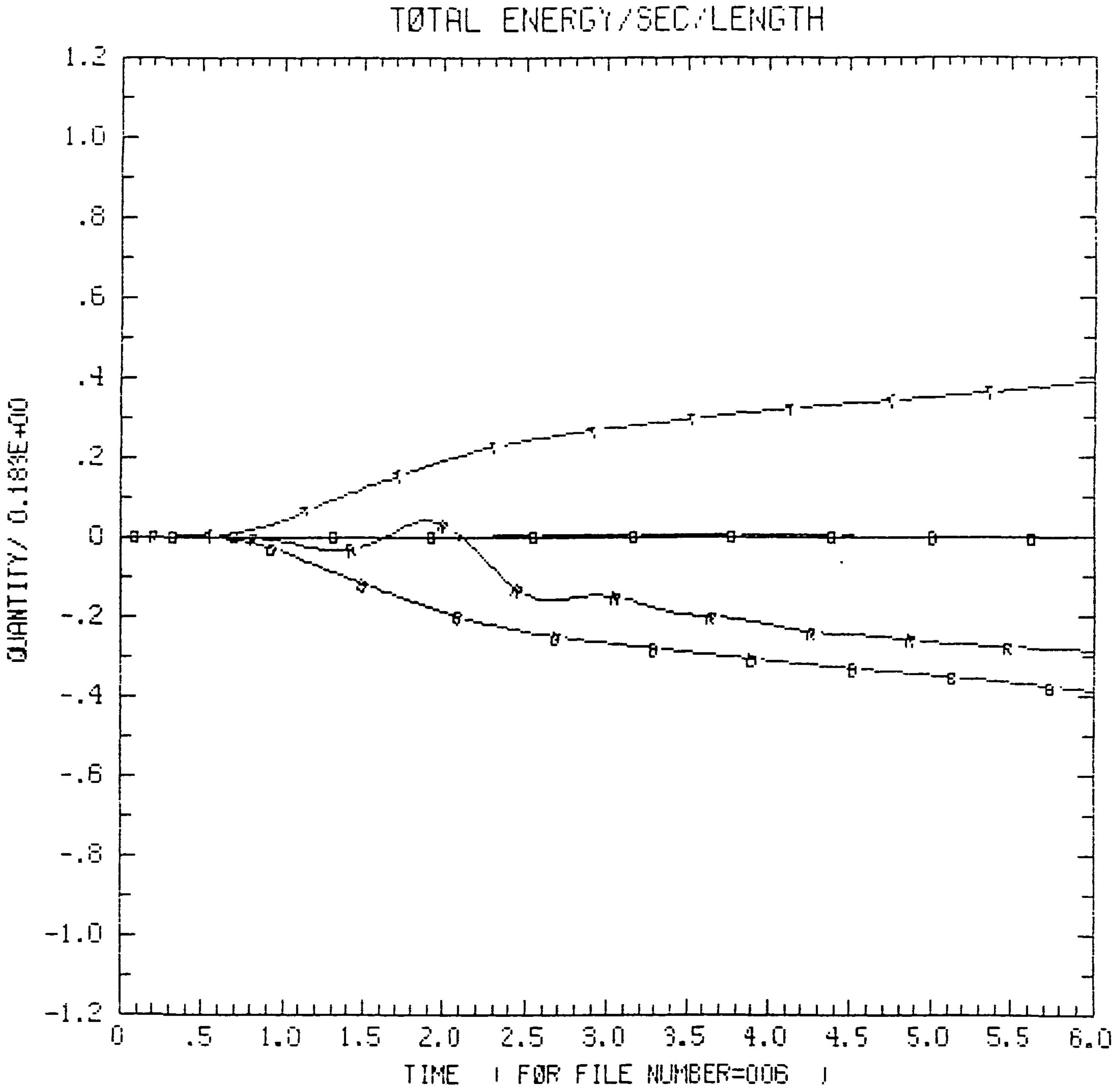
TØTAL ENERGY/SEC/LENGTH
1.2
1.0
.8
.6
.4
.2
0
-.2
-.4
-.6
-.8
-1.0
-1.2
QUANTITY/ 0.183E+00
0
.5
1.0
1.5
2.0
2.5
3.0
3.5
4.0
4.5
5.0
5.5
6.0
TIME (FØR FILE NUMBER=006)
T
R
B
D

FIG. 53

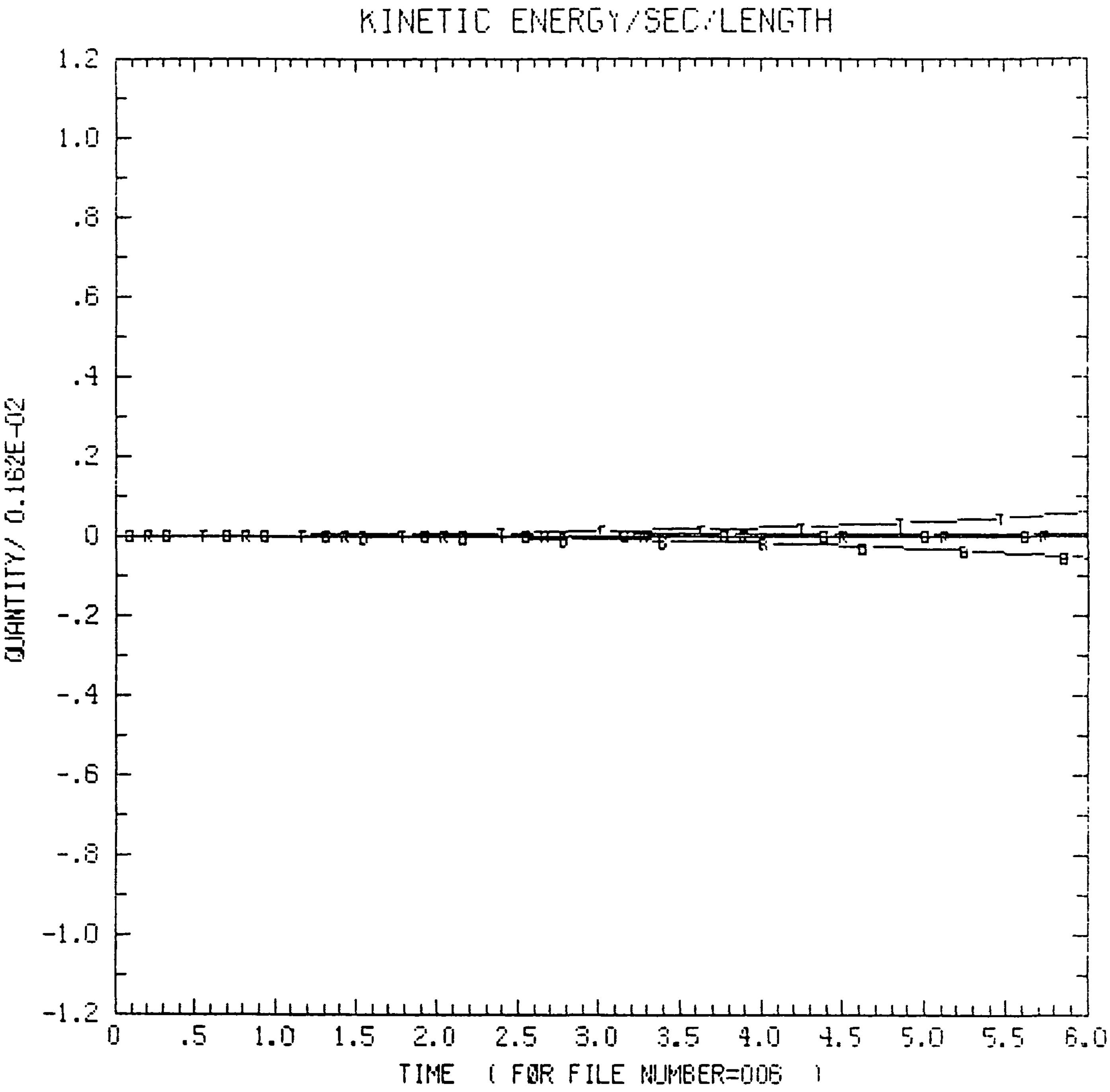
KINETIC ENERGY/SEC/LENGTH
1.2
1.0
.8
.6
.4
.2
0
-.2
-.4
-.6
-.8
-1.0
-1.2
QUANTITY/ 0.162E-02
0
.5
1.0
1.5
2.0
2.5
3.0
3.5
4.0
4.5
5.0
5.5
6.0
TIME (FØR FILE NUMBER=006)
T
B
R

FIG. 54

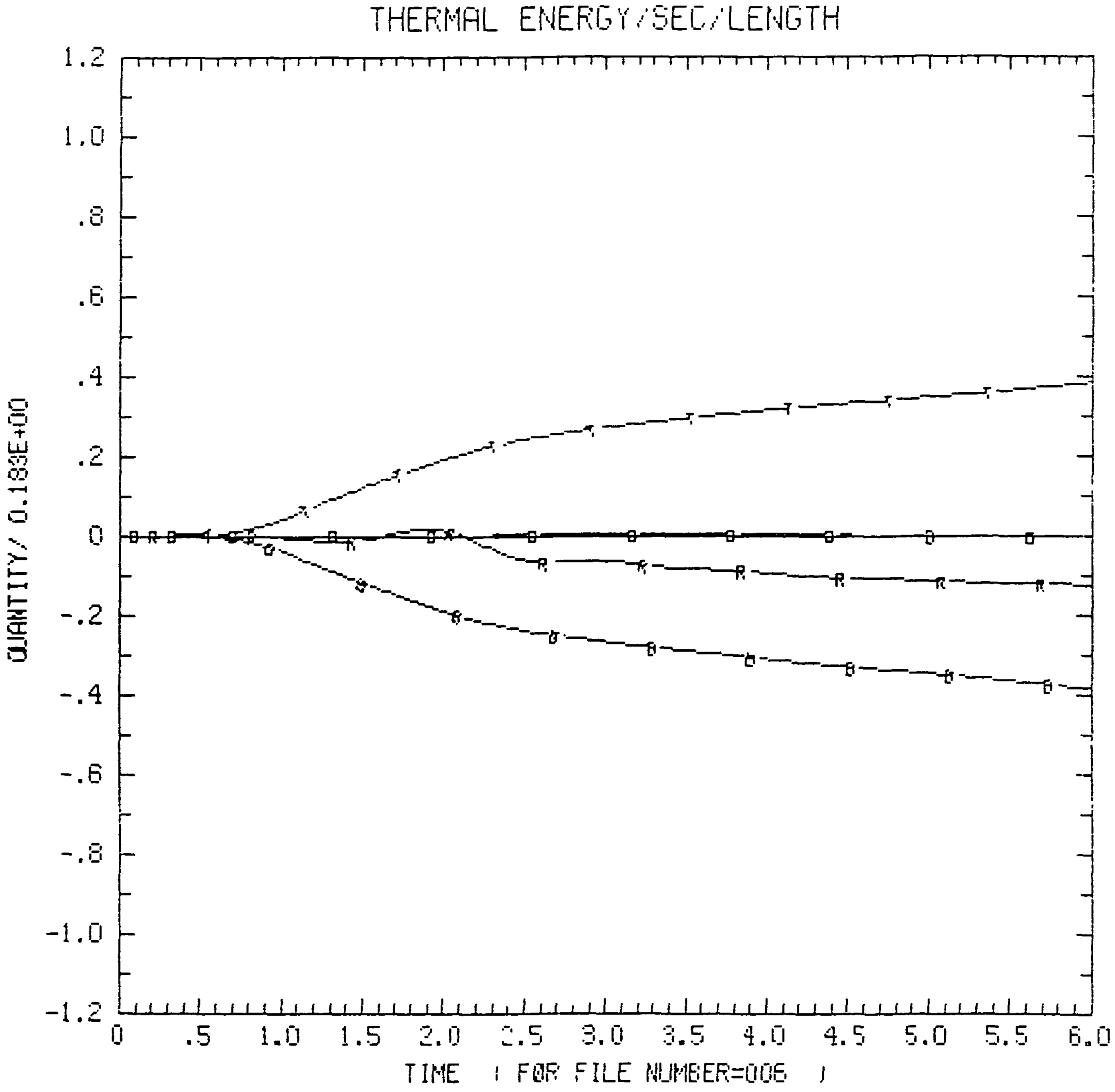
THERMAL ENERGY/SEC/LENGTH
QUANTITY/ 0.183E+00
1.2
1.0
.8
.6
.4
.2
0
-.2
-.4
-.6
-.8
-1.0
-1.2
0
.5
1.0
1.5
2.0
2.5
3.0
3.5
4.0
4.5
5.0
5.5
6.0
TIME (FOR FILE NUMBER=006)
T
B
R
D

FIG. 55

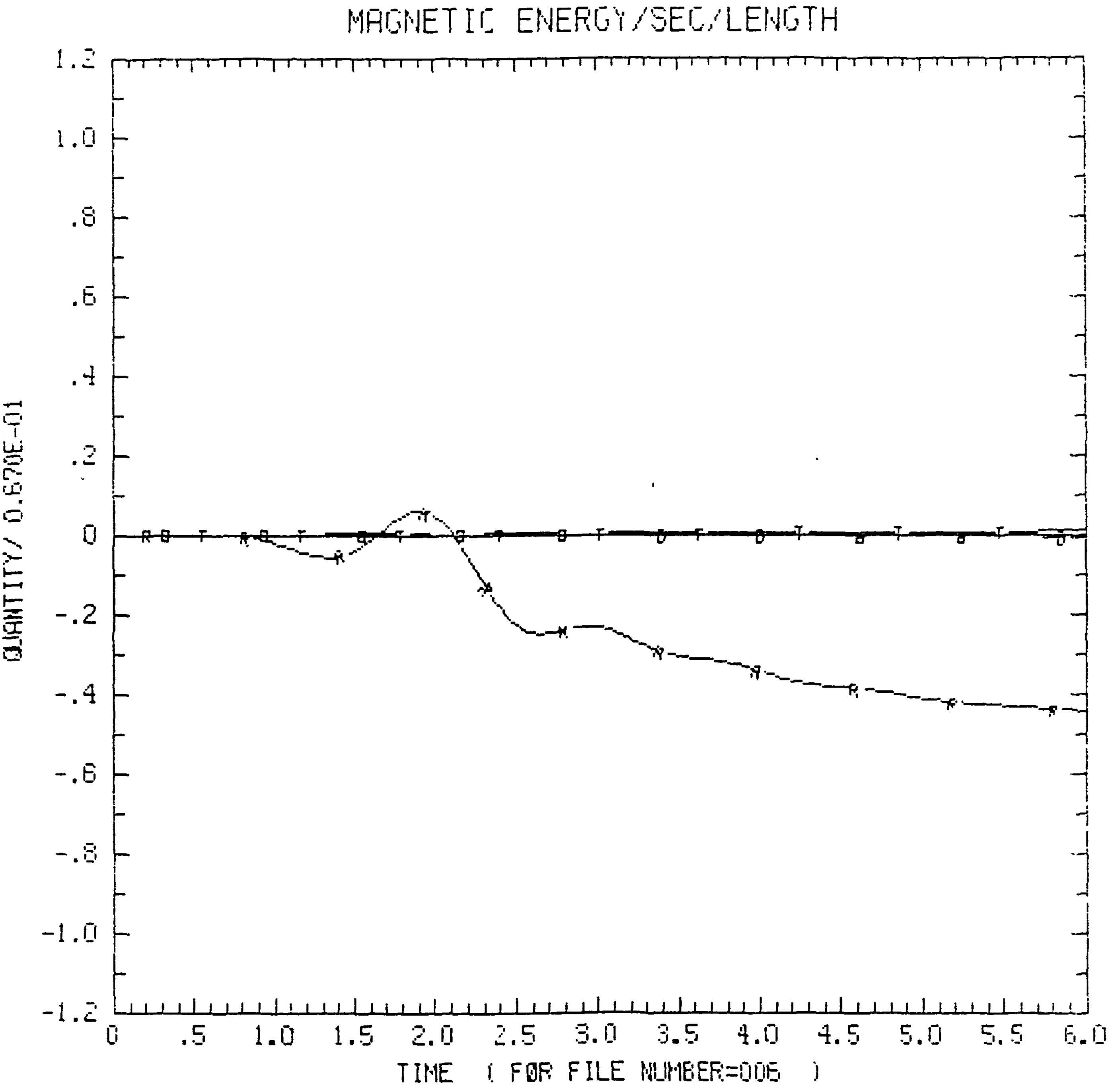
MAGNETIC ENERGY/SEC/LENGTH
QUANTITY/ 0.670E-01
1.2
1.0
.8
.6
.4
.2
0
-.2
-.4
-.6
-.8
-1.0
-1.2
0
.5
1.0
1.5
2.0
2.5
3.0
3.5
4.0
4.5
5.0
5.5
6.0
TIME (FØR FILE NUMBER=006)
R
B
T

FIG. 56

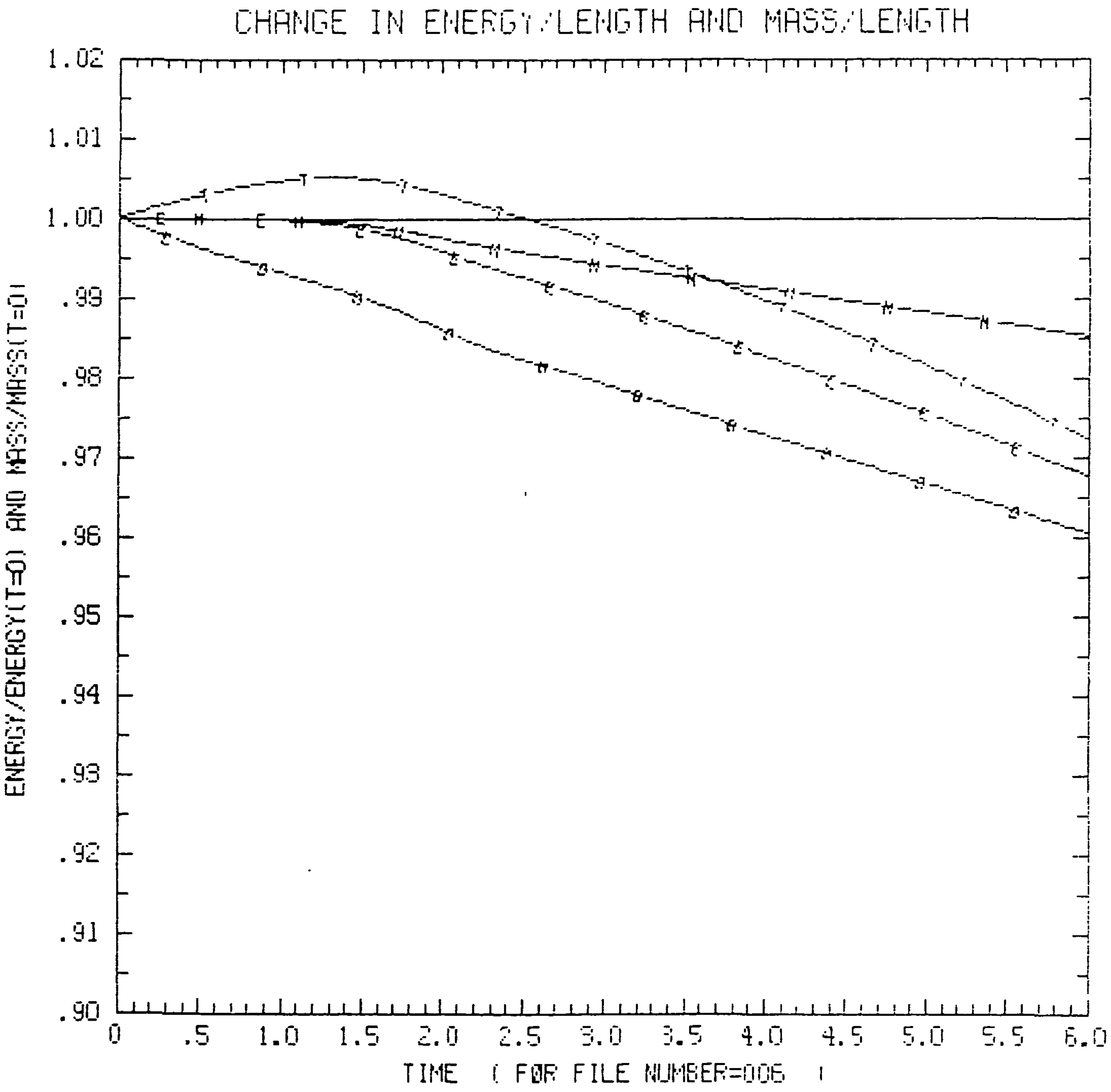
CHANGE IN ENERGY/LENGTH AND MASS/LENGTH
ENERGY/ENERGY(T=0) AND MASS/MASS(T=0)
1.02
1.01
1.00
.99
.98
.97
.96
.95
.94
.93
.92
.91
.90
0
.5
1.0
1.5
2.0
2.5
3.0
3.5
4.0
4.5
5.0
5.5
6.0
TIME (FØR FILE NUMBER=006)
T
E
M
Ø

FIG. 57

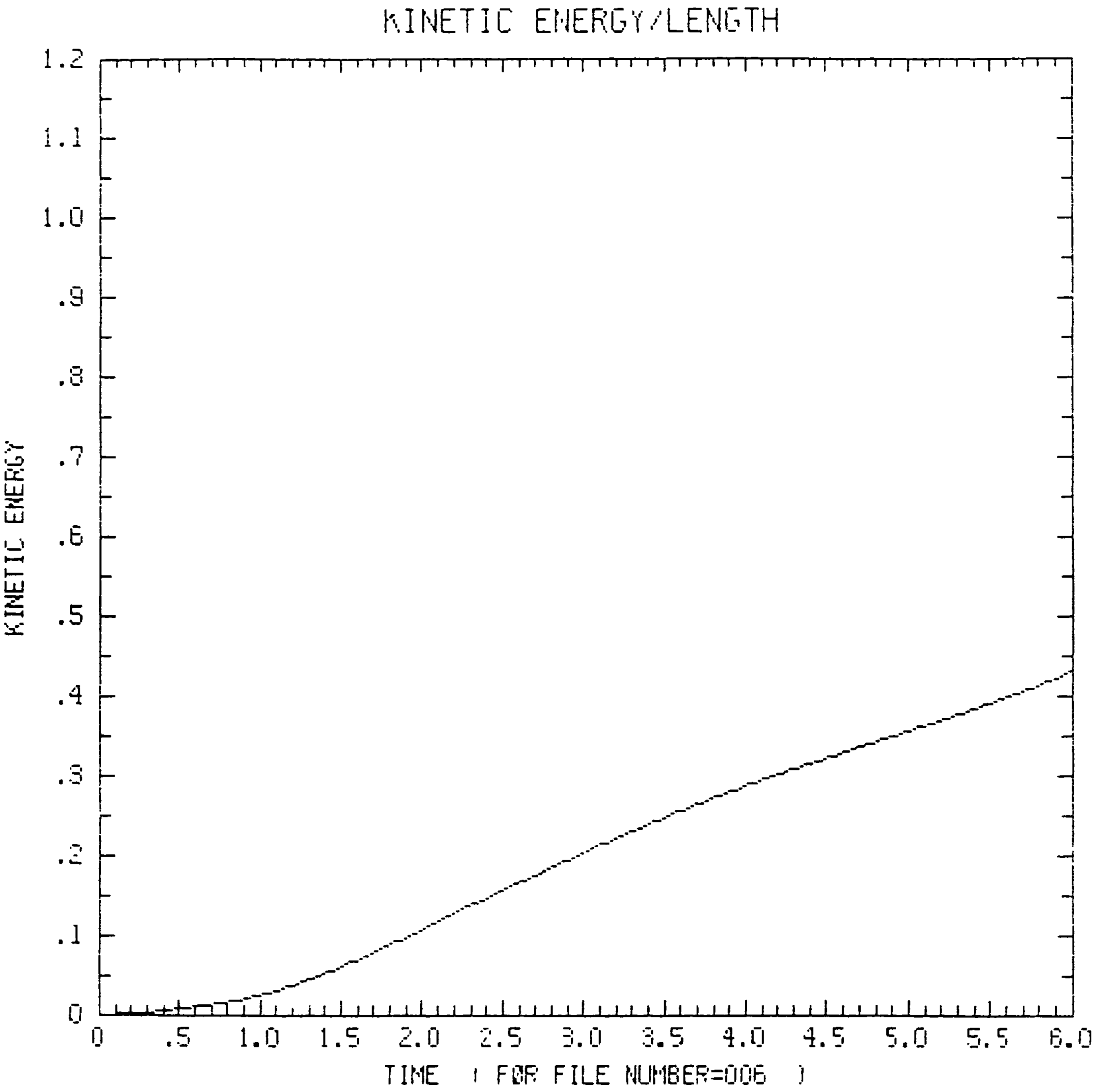
KINETIC ENERGY/LENGTH
1.2
1.1
1.0
.9
.8
.7
.6
.5
.4
.3
.2
.1
0
KINETIC ENERGY
0
.5
1.0
1.5
2.0
2.5
3.0
3.5
4.0
4.5
5.0
5.5
6.0
TIME (FØR FILE NUMBER=006)

FIG. 58

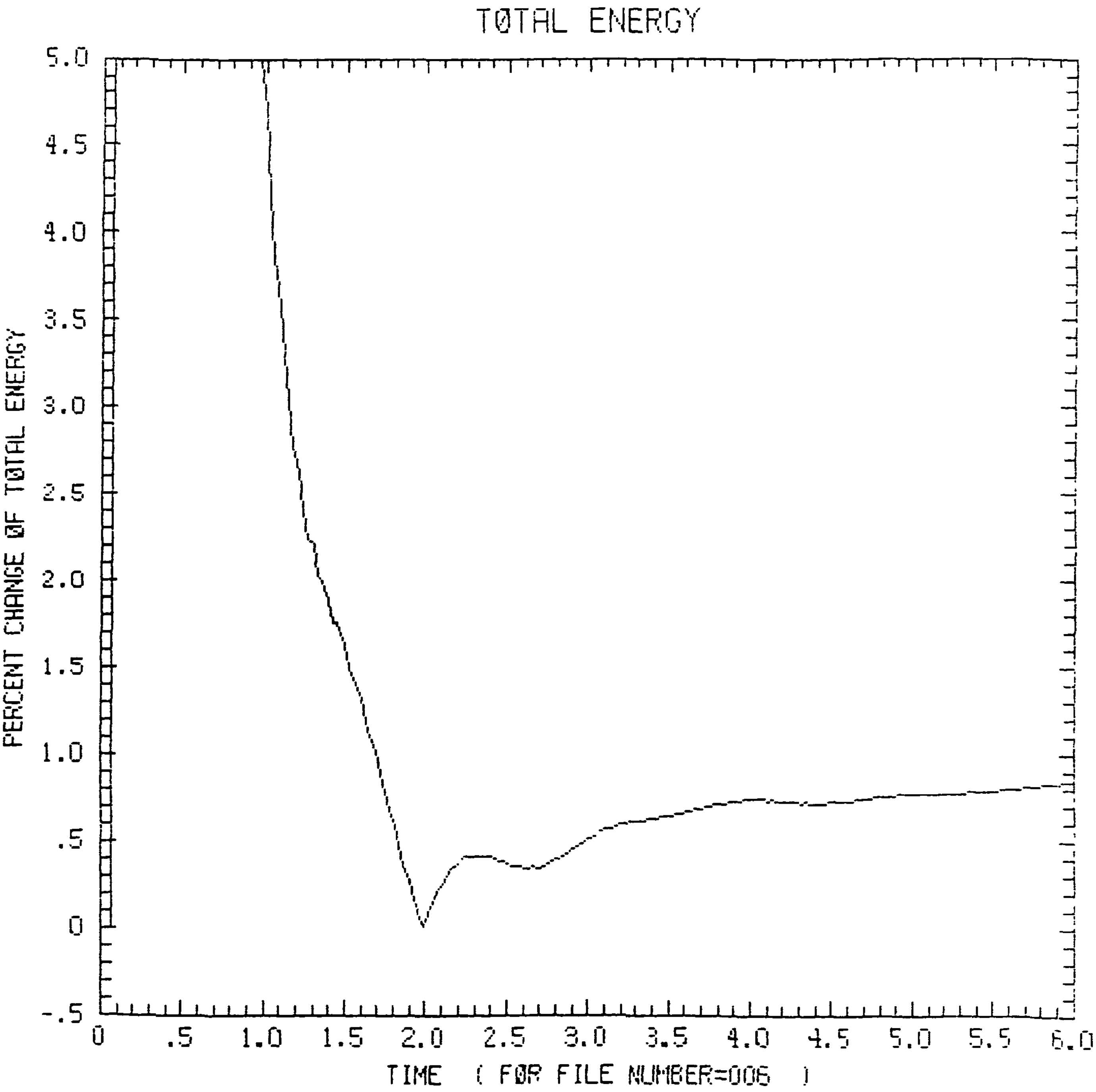
TØTAL ENERGY
PERCENT CHANGE ØF TØTAL ENERGY
5.0
4.5
4.0
3.5
3.0
2.5
2.0
1.5
1.0
.5
0
-.5
0
.5
1.0
1.5
2.0
2.5
3.0
3.5
4.0
4.5
5.0
5.5
6.0
TIME (FØR FILE NUMBER=006)

FIG. 59

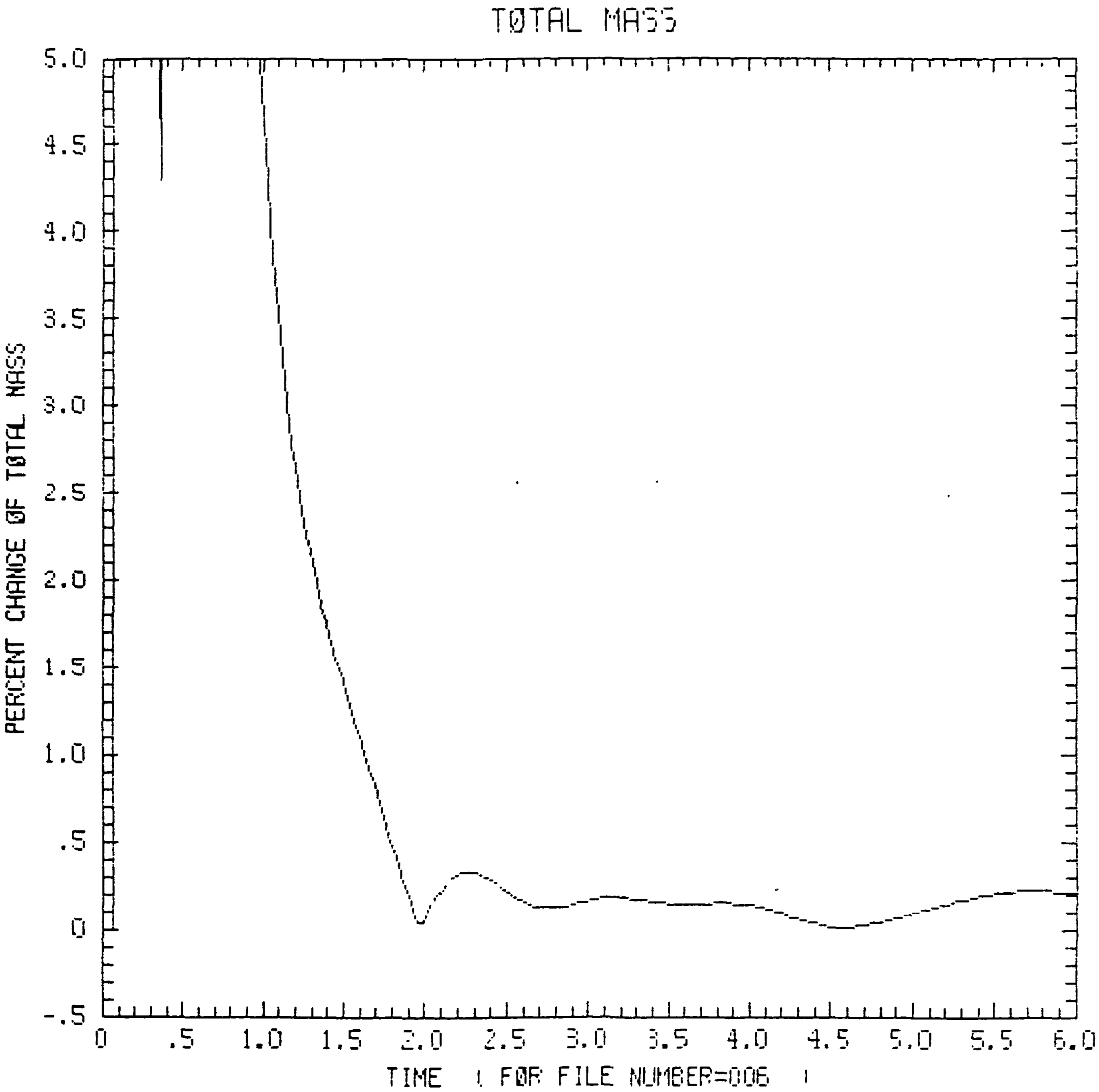

TØTAL MASS
PERCENT CHANGE ØF TØTAL MASS
5.0
4.5
4.0
3.5
3.0
2.5
2.0
1.5
1.0
.5
0
-.5
0
.5
1.0
1.5
2.0
2.5
3.0
3.5
4.0
4.5
5.0
5.5
6.0
TIME (FØR FILE NUMBER=006)

FIG. 60

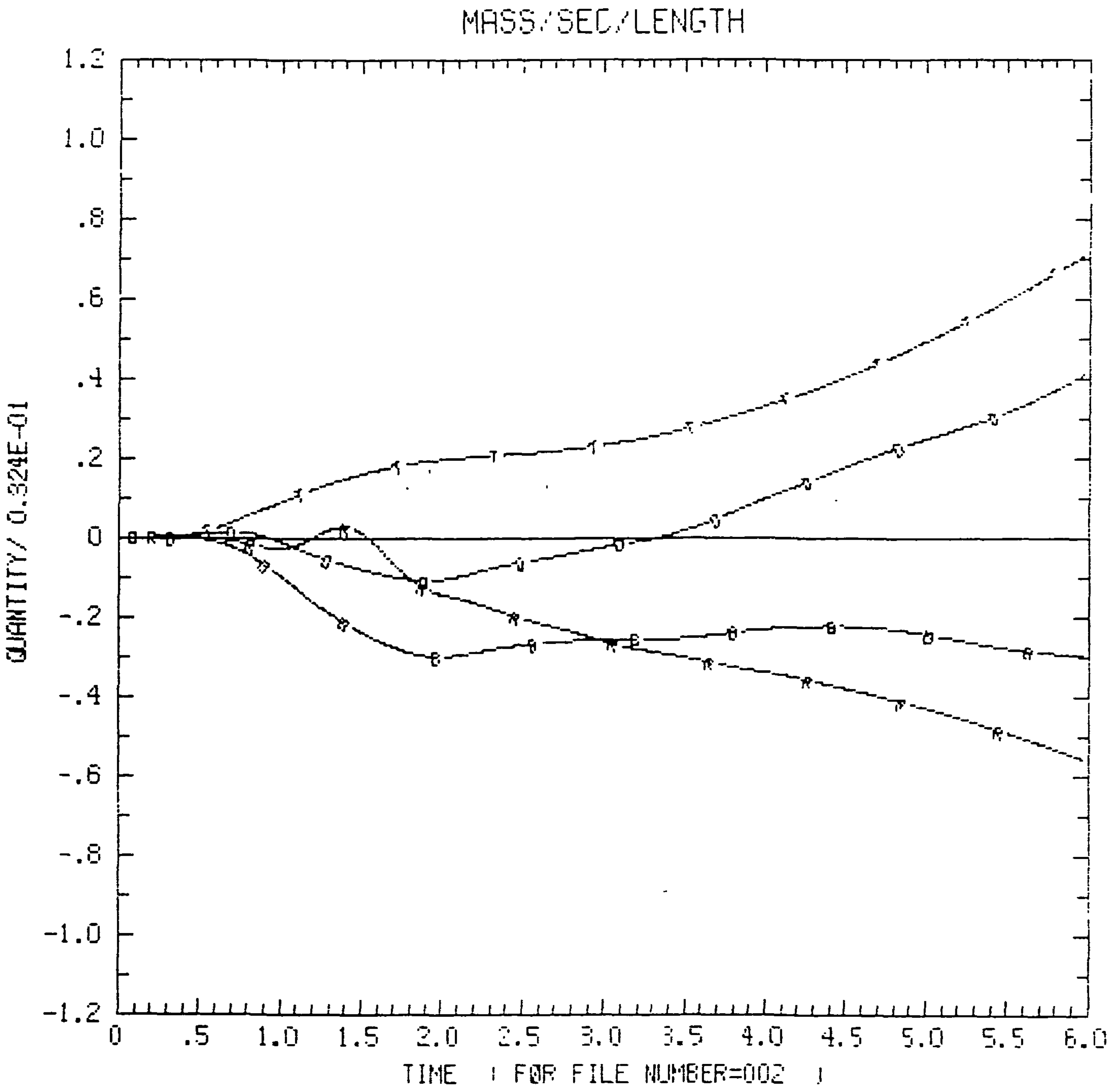
MASS/SEC/LENGTH
1.2
1.0
.8
.6
.4
.2
0
-.2
-.4
-.6
-.8
-1.0
-1.2
QUANTITY/ 0.324E-01
0
.5
1.0
1.5
2.0
2.5
3.0
3.5
4.0
4.5
5.0
5.5
6.0
TIME (FOR FILE NUMBER=002)

FIG. 61

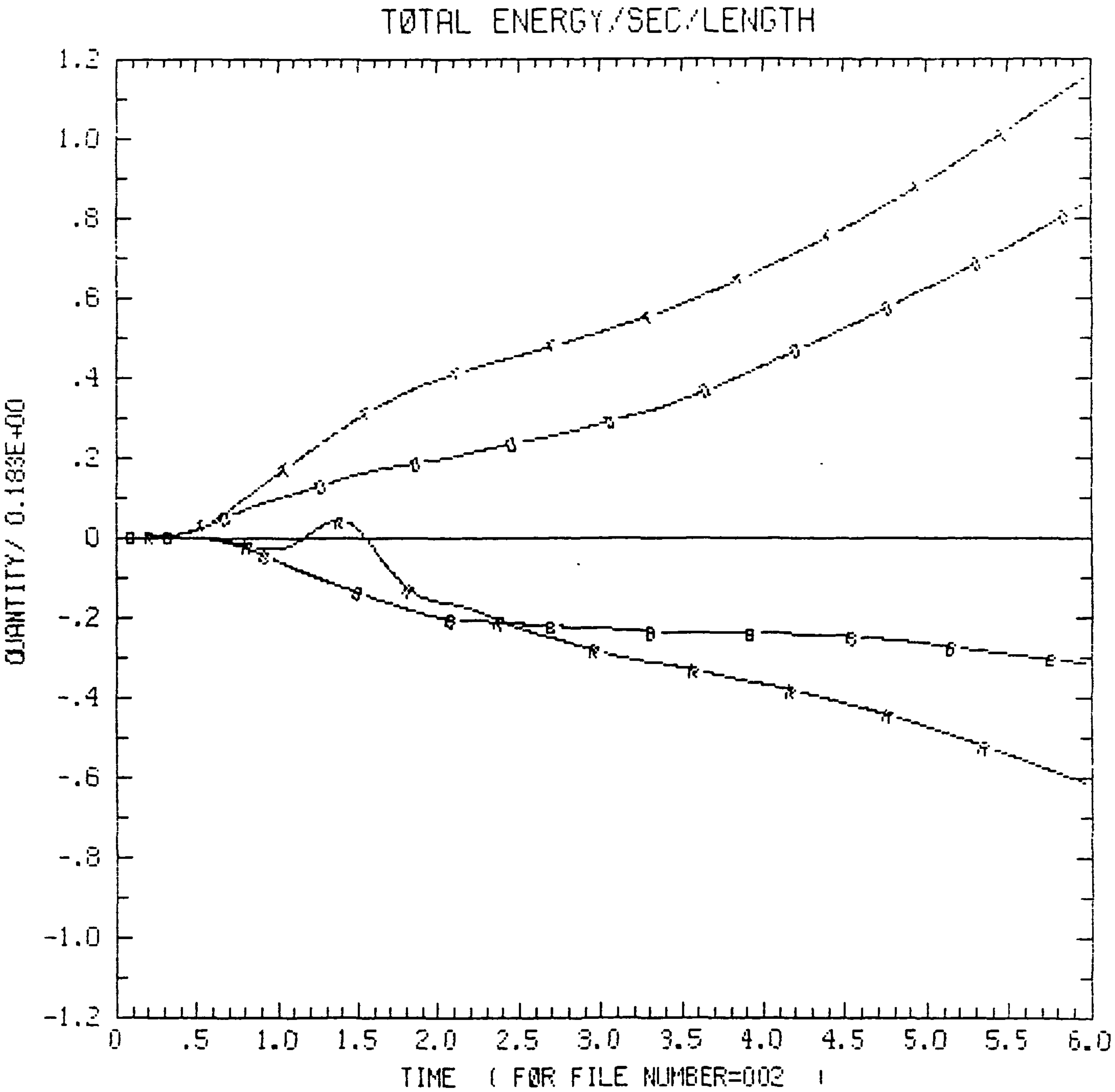
TOTAL ENERGY/SEC/LENGTH
QUANTITY/ 0.183E+00
1.2
1.0
.8
.6
.4
.2
0
-.2
-.4
-.6
-.8
-1.0
-1.2
0
.5
1.0
1.5
2.0
2.5
3.0
3.5
4.0
4.5
5.0
5.5
6.0
TIME (FOR FILE NUMBER=002)

FIG. 62

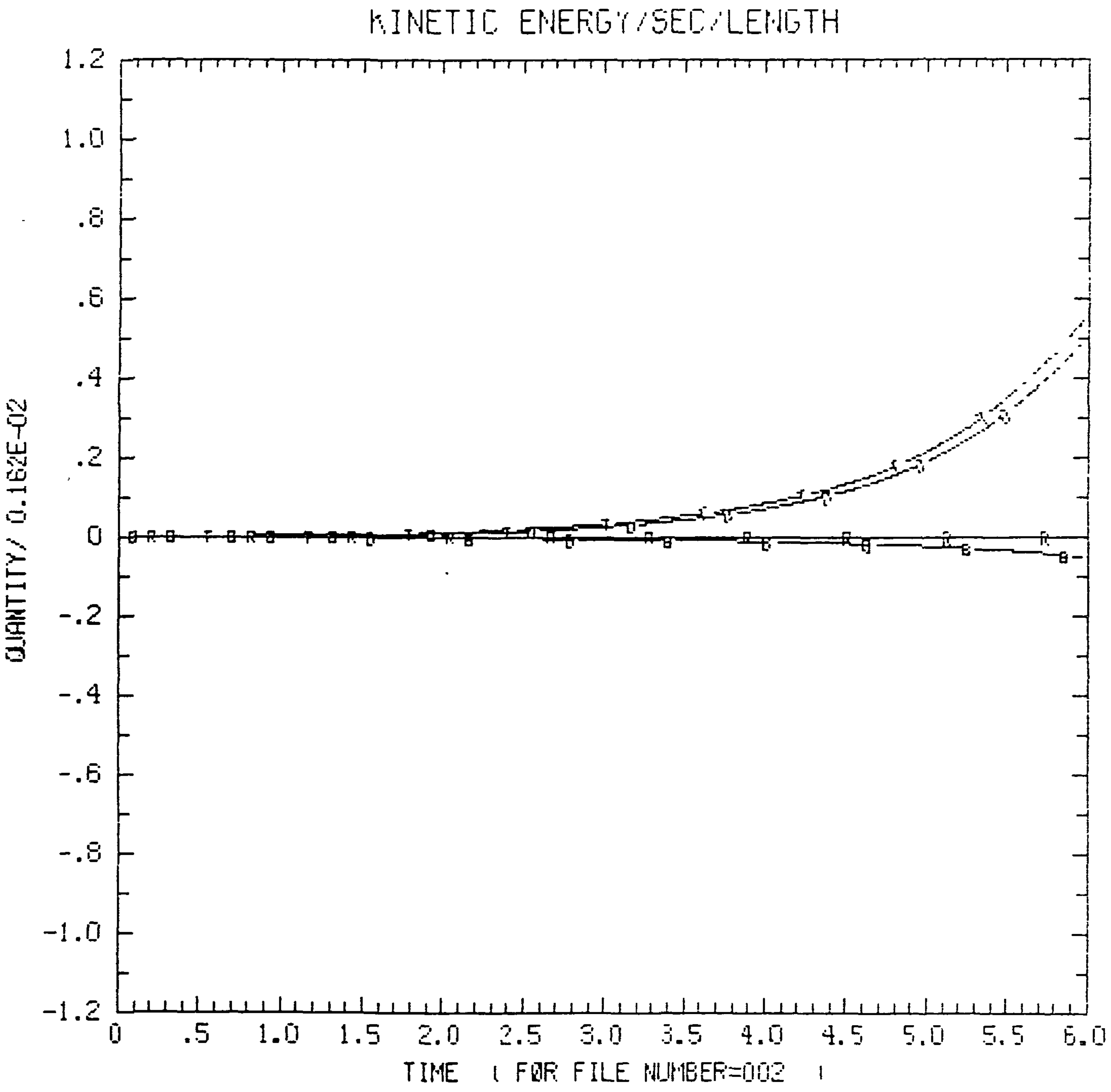
KINETIC ENERGY/SEC/LENGTH
QUANTITY/ 0.162E-02
1.2
1.0
.8
.6
.4
.2
0
-.2
-.4
-.6
-.8
-1.0
-1.2
0
.5
1.0
1.5
2.0
2.5
3.0
3.5
4.0
4.5
5.0
5.5
6.0
TIME (FØR FILE NUMBER=002)
T
B
R

FIG. 63

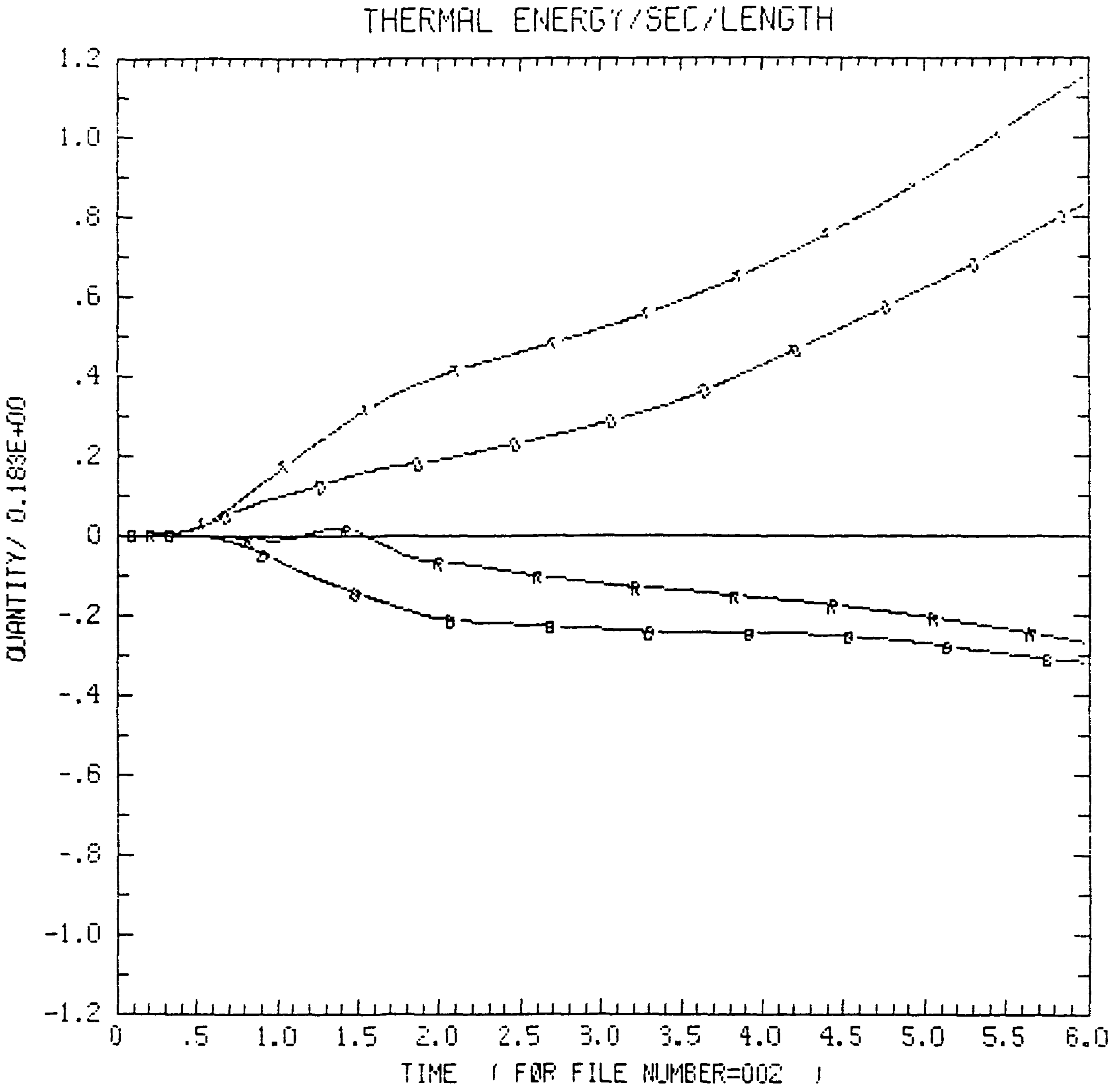
THERMAL ENERGY/SEC/LENGTH
QUANTITY/ 0.183E+00
1.2
1.0
.8
.6
.4
.2
0
-.2
-.4
-.6
-.8
-1.0
-1.2
0
.5
1.0
1.5
2.0
2.5
3.0
3.5
4.0
4.5
5.0
5.5
6.0
TIME (FØR FILE NUMBER=002)
R
B

FIG. 64

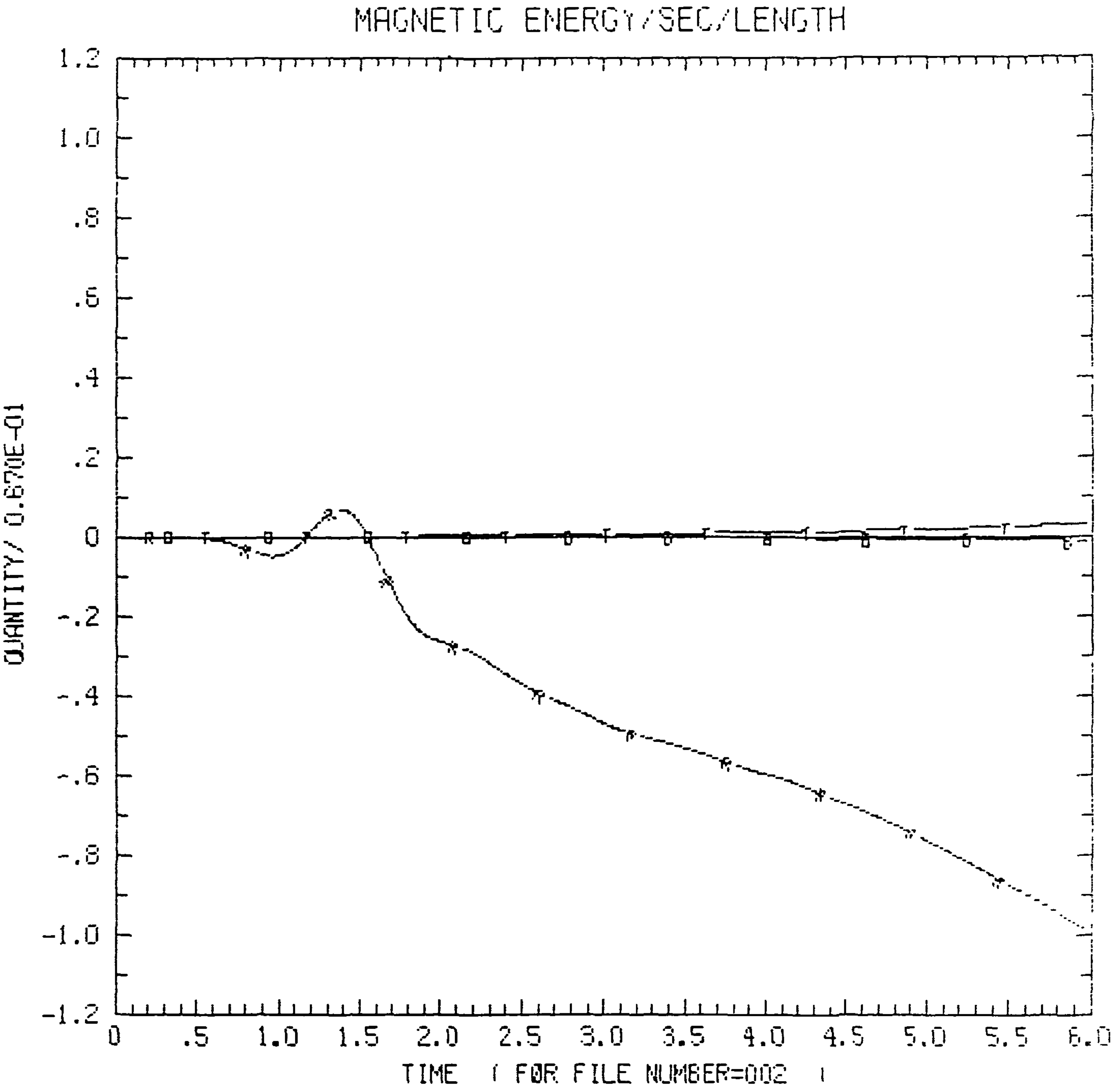
MAGNETIC ENERGY/SEC/LENGTH
1.2
1.0
.8
.6
.4
.2
0
-.2
-.4
-.6
-.8
-1.0
-1.2
QUANTITY/ 0.670E-01
0
.5
1.0
1.5
2.0
2.5
3.0
3.5
4.0
4.5
5.0
5.5
6.0
TIME (FØR FILE NUMBER=002)

FIG. 65

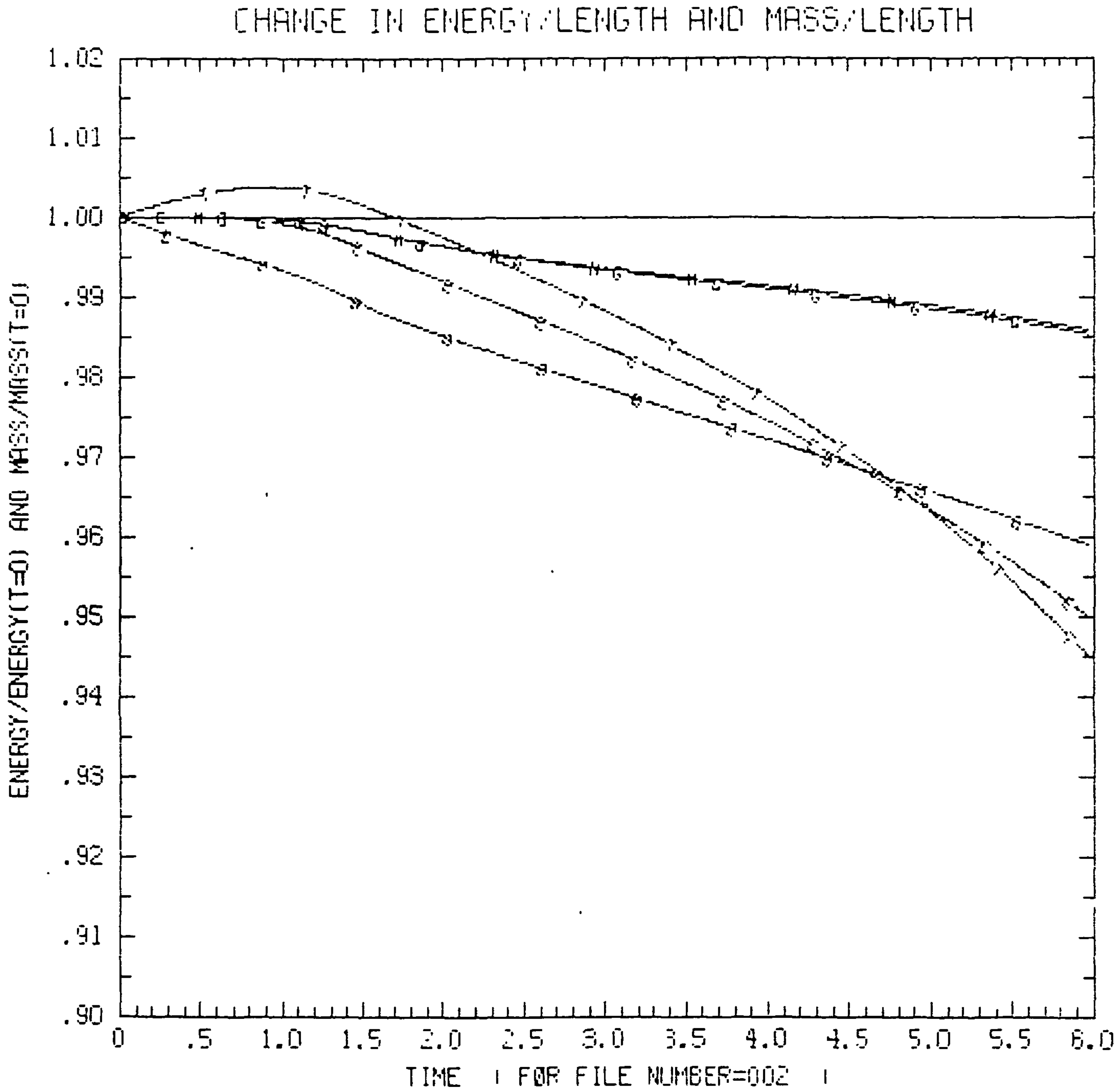

FIG. 66

7 = Thermal energy (heating [illegible])
6 = [illegible] energy
8 = Mag energy

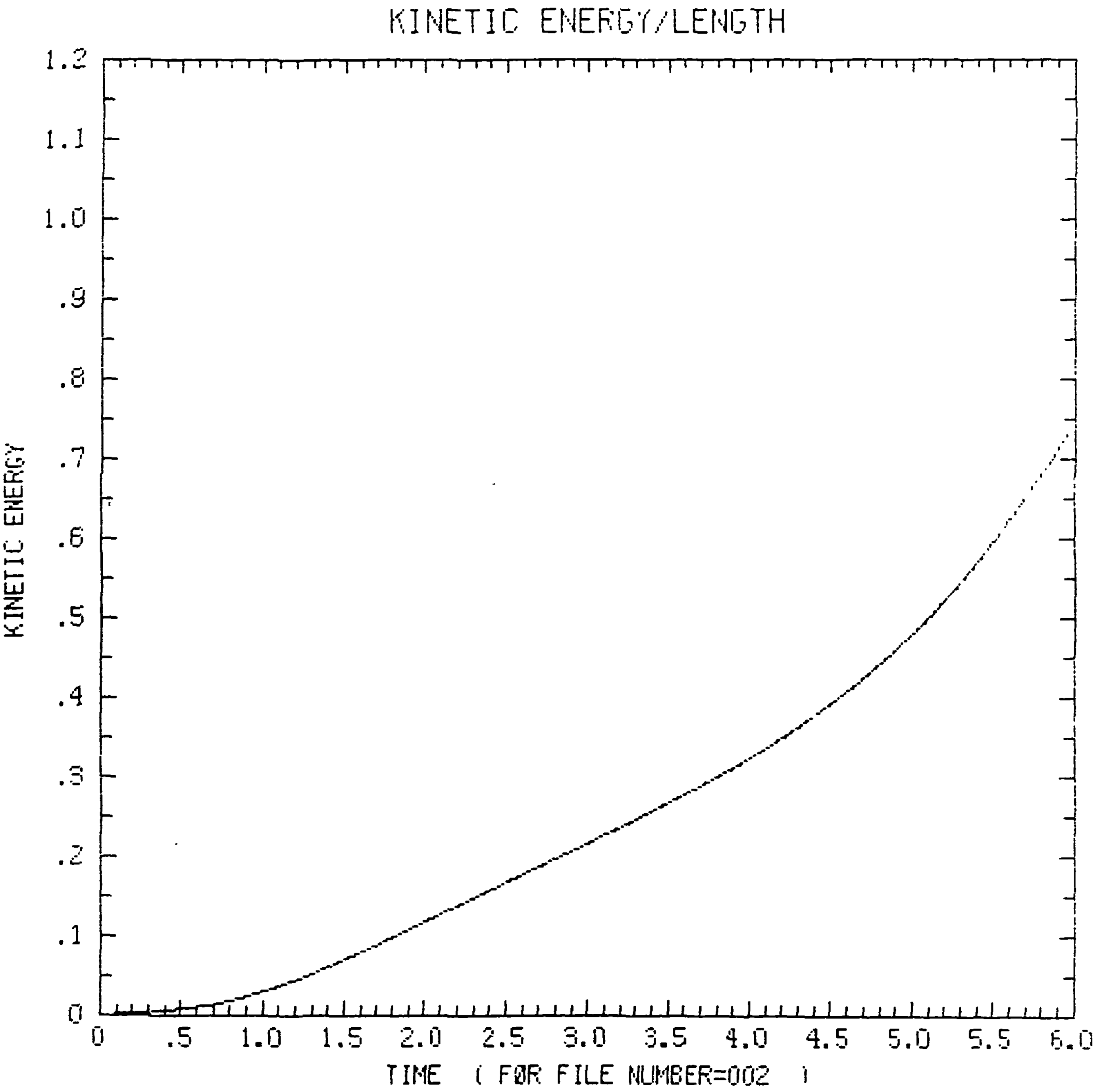
KINETIC ENERGY/LENGTH
KINETIC ENERGY
1.2
1.1
1.0
.9
.8
.7
.6
.5
.4
.3
.2
.1
0
0
.5
1.0
1.5
2.0
2.5
3.0
3.5
4.0
4.5
5.0
5.5
6.0
TIME (FØR FILE NUMBER=002)

FIG. 67

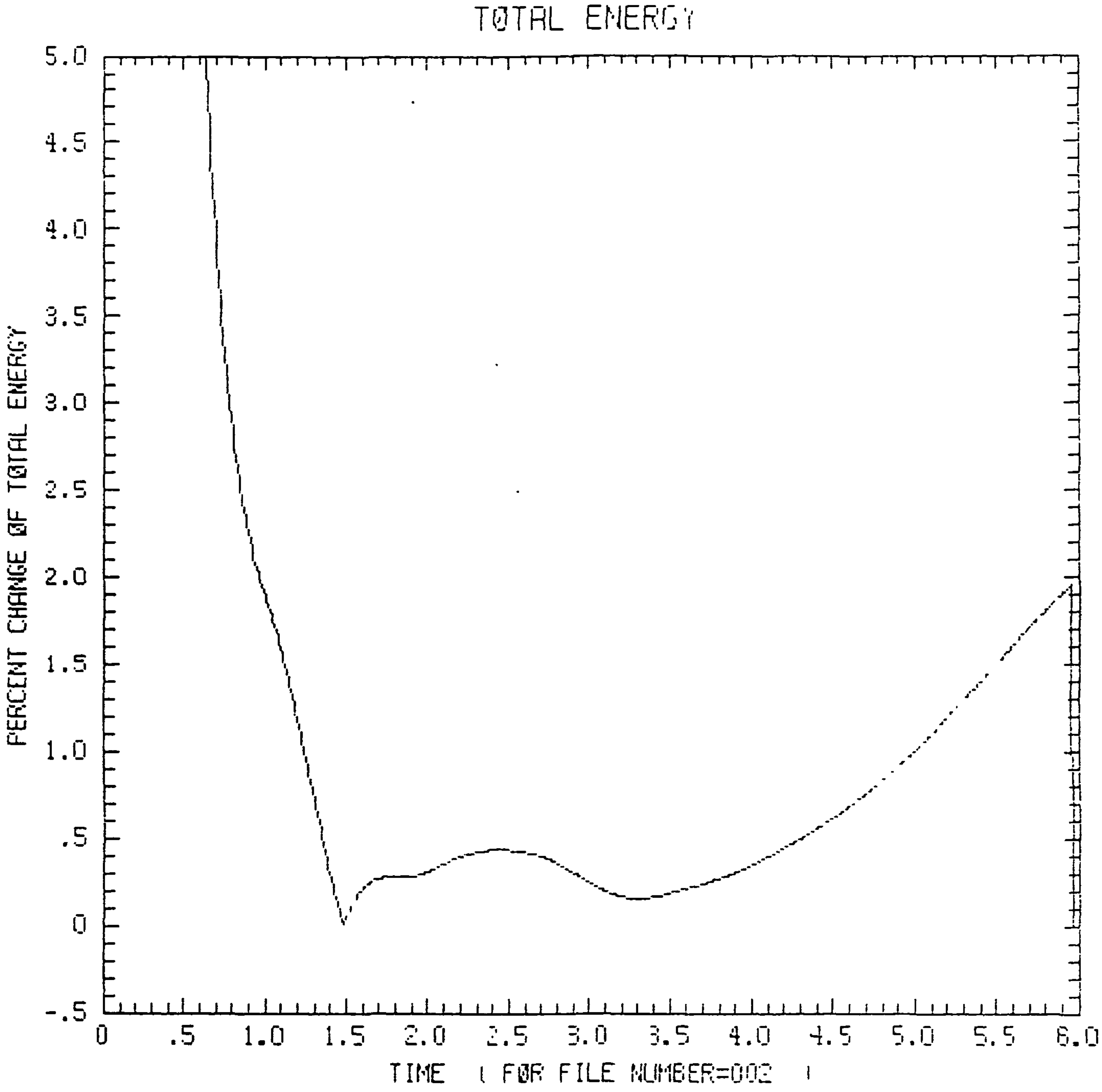
TOTAL ENERGY
5.0
4.5
4.0
3.5
3.0
2.5
2.0
1.5
1.0
.5
0
-.5
PERCENT CHANGE OF TOTAL ENERGY
0
.5
1.0
1.5
2.0
2.5
3.0
3.5
4.0
4.5
5.0
5.5
6.0
TIME (FOR FILE NUMBER=002)

FIG. 68

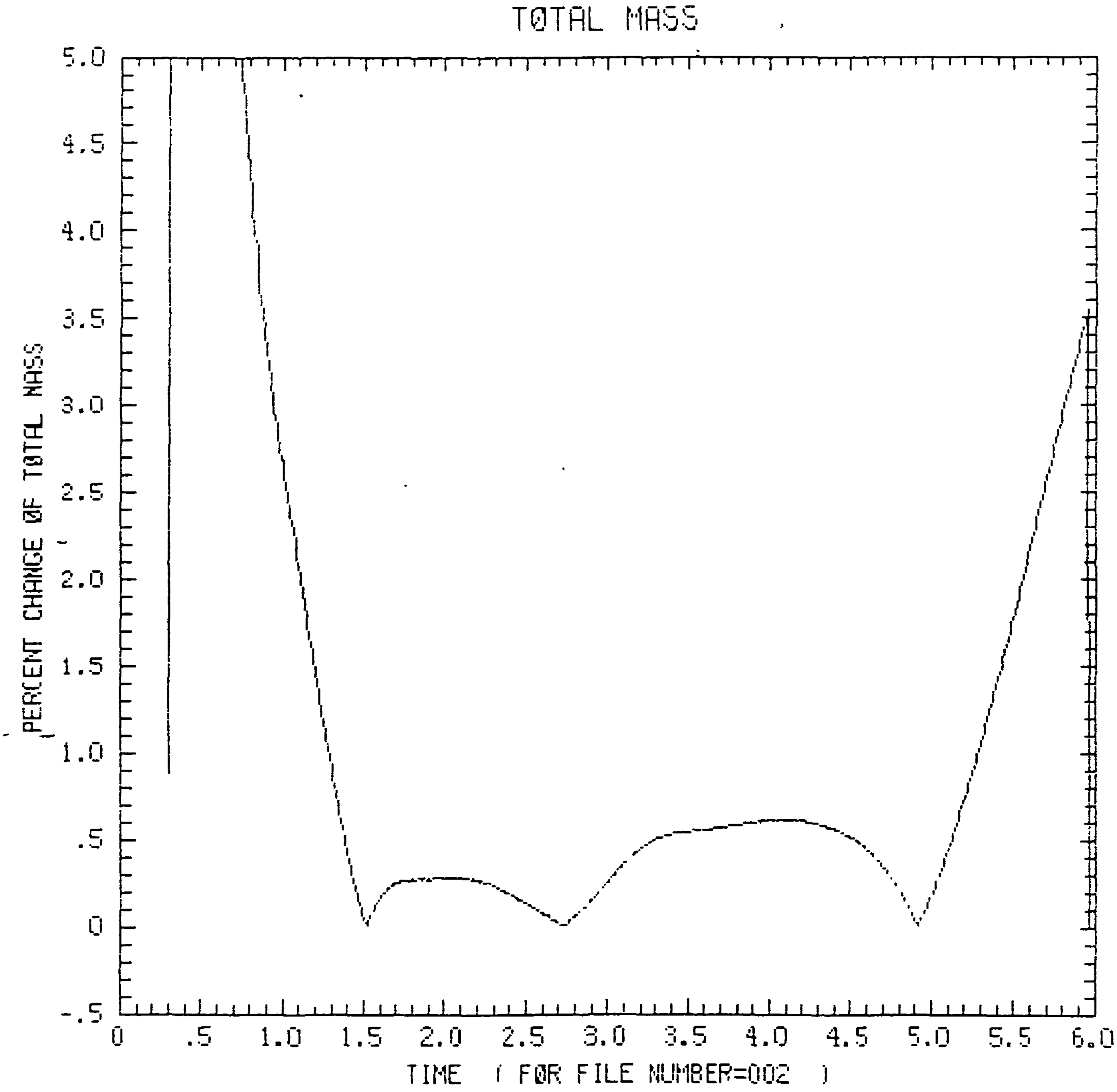
TØTAL MASS
PERCENT CHANGE ØF TØTAL MASS
5.0
4.5
4.0
3.5
3.0
2.5
2.0
1.5
1.0
.5
0
-.5
0
.5
1.0
1.5
2.0
2.5
3.0
3.5
4.0
4.5
5.0
5.5
6.0
TIME (FØR FILE NUMBER=002)

FIG. 69